GEOMETRIC CONTROL OF 3D CHROMOSOME ORGANIZATIONS

YEJUN WANG

(Bsc. (Chemistry) Zhejiang University, China)

A THESIS SUBMITTED

FOR THE DEGREE OF DOCTOR OF PHILOSOPHY

MECHANOBIOLOGY INSTITUTE

NATIONAL UNIVERSITY OF SINGAPORE

2016

DECLARATION

I hereby declare that this thesis is my original work and it has been written by me in its entirety. I have duly acknowledged all the sources of information which have been used in the thesis. This thesis has also not been submitted for any degree in any university previously.

Yejun Wang

18 July 2016

ACKNOLEDGEMENTS

First and foremost, I would like to express my deep and genuine gratitude to my academic supervisor Prof. Shivashankar, who kindly opened the door to the field of mechanobiology for me five years ago, and have constantly supported me in my pursuit of the doctorate degree. He guided me to the beautiful yet not fully-understood world of cell nucleus, financially and intellectually supported me to understand principles underlying mechanotransduciton in genome regulation. While giving enough freedom to my project development and time management, he has always been there whenever I was lost, and placed me back onto the track. I greatly appreciate his patience to my trials and errors and more importantly his faith in me being a good scientist.

I would also like to thank my thesis committee members: Prof. Linda Kenney and Prof. Pakorn,Tony Kanchanawong for their critical and valuable comments on my projects throughout my PhD. I would like to thank MBI for providing state-of-art facilities and collaborative environment. I thank my collaborators Prof. Michelle Wang, Prof. Fabrizio d'Adda di, and Assistant Prof. Caroline Uhler for their useful suggestions and scientific inputs to my work. I thank MBI admin staffs especially Carol and Ai Leng for their great help in all the student matters. I thank Microscopy core especially Kah Jun, Liu Jun, and Waihan for their assistance in Zeiss Elyra, SIM, and confocal microscopes. I thank Science communication core especially Steven and Chun Xi for improving English and illustration when publicizing my work.

I thank Shova, who mentored me during my rotation and early years in this lab. She is one of the reasons why I chose to stay in this lab. She is friendly, intelligent, and diligent, who inspired me to make friends inside and outside the lab, and to work as hard as her.

I thank all my labmates, colleagues, and friends including but not limited to: Venky, Ekta, Nisha, Abhishek, Shefali, Soumya, Nikhil, Qingsen, Mallika, KeeChua, Kathirvel, Aninda, Saradha, RK, Prasuna, Xiaowei, Shifali, Bibhas, Karthik, Mrinal, Aneesh, Rishita, Kamal, Eric, Tingting, Jiawei, Pan Meng, Darren, Tina, Catherine, Jichao, Shiyin for their accompany during the past five years. Last but not the least I would like to thank my family for understanding and supporting me to pursue my academic dreams unconditionally.

-Yejun

TABLE OF CONTENTS

SUMMARY ..... **vii**

LIST OF PUBLICATIONS ..... **viii**

LIST OF TABLES ..... **ix**

LIST OF FIGURES ..... **ix**

LIST OF SYMBOLS ..... **xiv**

CHAPTER1: INTRODUCTION **1**

1.1 Role of extracellular matrix on tissue homeostasis, differentiation, and transcription regulation. 2

1.2 Link between extracellular matrix and nuclear architecture. 3

1.3 Role of chromatin remodelling and 3D chromosome position on genome regulation 4

1.4 Superresolution imaging of chromatin structures. 6

1.5 Hypothesis 7

1.6 Overview of the thesis 7

CHAPTER2: METHODS AND MATERIALS **12**

CHAPTER3: CELL GEOMETRY REORIENTS AND REPOSITIONS CHROMOSOMES TO REGULATE GENOMIC PROGRAMS. **26**

3.1 Cell geometry influences the normalized volume and the normalized radial distance of chromosomes. 27

3.2 Changes in radial position were accompanied by differential levels of 5S RNA pol2. 32

3.3 Cell geometry regulates the intermingling degrees between specific chromosomes. 34

3.4 Chromosome orientation correlates with the specificity in intermingling changes. 37

3.5 Coupling between chromosome reorganization and transcriptome change. 39

3.6 The presence of 5S RNA pol2, SRF and its target gene *zyxin* in the intermingling regions is regulated by cell geometry. 44

3.7 Ellipsoid packing models predict cell geometry specific CT orientations and new neighbourhoods. 50

CHAPTER4 SUPERRESOLUTION MICROSCOPY REVEALS DECONDENSED CHROMATIN STRUCTURE AND CHROMOSOMAL CONTACTS AT ACTIVE TRANSCRIPTION SITES 56

4.1 Characterization of chromatin fibers 57

4.2 Enhancing the resolution of chromatin using BALM 60

4.3 Serum starvation induced chromatin condensation 67

4.4 BALM detects transcriptional regions on chromatin fibers 69

4.5 BALM imaging of digested chromatin fragments 76

4.6 Chromosomal contacts are lost upon transcriptional quiescence 82

4.7 Visualization of YAP target chromosomal contacts 84

4.8 Visualization of SRF target chromosomal contacts 87

4.9 Visualization of NF-κB target chromosomal contacts 90

4.10 EpiTect ChIP analysis reveals promoter occupancy of NF-κB on its target chromosomal contacts 93

CHAPTER5: CONCLUSION, DISCUSSION, AND FUTURE DIRECTIONS 97

BIBILIOGRAPHY 108

APPENDICES 113

SUMMARY

Extracellular matrix (ECM) signals regulate gene expression program, which is central to tissue and cell homeostasis such as cell proliferation, apoptosis, differentiation, as well as tumor initiation and progression. Regulation of eukaryotic genes occurs through various layers including 3D chromosome positioning, chromatin remodeling, and chromosome physical interactions. While such ECM- regulated modular gene expression is remarkable, how these mechanical signals are integrated into the 3D chromosome architecture is not clear. In the first project, we quantitatively investigated the role of cell geometry on 3D chromosome position and revealed its implications in genome regulation. In the second project, we developed open chromatin spreads to visualize decondensed chromatin structures and nanoscale chromosomal contacts at active transcription sites using superresolution microscopy. With this system we discovered that cell geometry regulates the cellular level of chromosomal contacts associated with specific transcription factors, while differentially regulating their target genes. Taken together, this work provides a quantitative framework together with a robust open chromatin platform to systematically understand the role of cell geometry in 3D chromosome reorganization for genome regulation.

LIST OF PUBLICATIONS

1. **Super-resolution microscopy reveals decondensed chromatin structure at transcription sites**. **Yejun Wang**, Shovamayee Maharana, Michelle Wang & G.V.Shivashankar *Sci Rep*. (2014) Mar 26;4:4477

2. **Evolution of chromosome intermingling regions during differentiation reveals principles of chromosome organization.** Shovamayee Maharana*, K. Venkatesan Iyer*, Nikhil Jain*, Mallika Nagarajan*, **Yejun Wang**, G. V. Shivashankar. *Nucleic Acid Research* (2016) * Equal Contributors

3. **Role of cell geometry on nuclear mechanics, chromosome reorganization, and gene expression. Yejun Wang***, Ekta Makhija*, Karthik Damodaran and G. V. Shivashankar (2016, *Molecular and Cellular Mechanobiology*, Edited by Shu Chien, Adam Engler, and Peter Wang)* Equal Contributors

4. **Cell geometry orients chromosomes to regulate genomic programs. Yejun Wang**, Mallika Nagarajan, Caroline Uhler, G. V. Shivashankar. (2016, under review in NAR)

5. **Superresolution microscopy reveals physical chromosomal contacts at single cell level. Yejun Wang**, Ratna Prasuna Vogirala, G. V. Shivashankar. (2016, submitted)

LIST OF TABLES

Table4.1 Chromatin staining methods. 59

Table 4.2 λ DNA combing methods. 63

LIST OF FIGURES

Figure 1.1 Link between ECM and nuclear architecture. 4

Figure 3.1 Effects of cell geometry on cytoskeleton organization and nuclear morphology 27

Figure 3.2 Representative images of painted 12 chromosomes and nucleus. 28

Figure 3.3 Monitoring of the 3D image thresholding 29

Figure 3.4 Bar graph quantifying the absolute and normalized chromosomes volume. 30

Figure 3.5 Cell geometry influences the normalized radial distance of chromosomes. 31

Figure 3.6 Correlation between chromosome radial distance and deccompaction. 32

Figure 3.7 Changes in radial position are accompanied by differential levels of 5S RNA pol2. 33

Figure 3.8 Activated form of RNA pol2 was revealed as pocket like structures at the surface of CTs. 34

Figure 3.9 Intermingling between chromosomes is negatively correlated with radial distance. 35

Figure 3.10 Cell geometry regulates the intermingling degrees between specific chromosomes. 36

Figure 3.11 Cell geometry reorients chromosomes. 37

Figure 3.12 Chromosomes orienting along mechanical axis are sensitive to geometry changes. 39

Figure 3.13 Coupling between the radial position change and chromosome activity change. 40

Figure 3.14 Coupling between the intermingling change and interchromosome activity distance change. 41

Figure 3.15 NF-κB target genes and SRF/ MRTF-A target genes. 43

Figure 3.16 5S RNA pol2 enriched in the intermingling regions, the level of which decreases when chromosomes intermingle less. 44

Figure 3.17 Treatment with 40 μg/ml α-amanitin for 30 min decreases the level of 5S RNA pol2. 45

Figure 3.18 Transcription is required for the increase in intermingling degrees. 46

Figure 3.19 Localization frequency of SRF&5S RNA pol2 clusters and *zyxin* in intermingling regions is regulated by cell geometry. 47

Figure 3.20 Chromosome reorientation and reposition is not due to global changes in transcription. 49

Figure 3.21 Ellipsoid packing models. 51

Figure 3.22 Ellipsoid packing models predict cell geometry specific chromosome orientations. 52

Figure 3.23 Ellipsoid packing models predict cell geometry specific chromosome radial positions. 52

Figure 3.24 Ellipsoid packing models predict cell geometry specific new neighborhoods. 53

Figure 3.25 Model for the 3D chromosome reorganization in facilitating the geometry-dependent genome regulation. 55

Figure 4.1 Functionality of chromatin fibers. 57

Figure 4.2 Measurement of fiber thickness. 58

Figure 4.3 Effect of expansion time on the structure of chromatin fibers and the loss of histone proteins as well as transcription machinery. 60

Figure 4.4 Chromatin fibers detected in PALM and BALM. 62

Figure 4.5 TIRFM images of λ DNA stretched using different methods. 62

Figure 4.6 Characterization of λDNA in BALM. 64

Figure 4.7 Number of localization events at each of the ten thousand frames. 65

Figure 4.8 BALM images of chromatin fibers. 66

Figure 4.9 Condensed chromatin after serum starvation. 67

Figure 4.10 Spatial correlation analysis of chromatin fibers in serum -/ + conditions. 68

Figure 4.11 TIRFM and BALM imaging of 5S RNA pol2. 70

Figure 4.12 Colocalization of decondensed regions with 5S RNA pol2. 71

Figure 4.13 Quantification of gap structures detected by BALM imaging..... 72

Figure 4.14 Transcriptionally active gap structures are independent of frame numbers or photons collected while imaging. 73

Figure 4.15 Colocalization analysis for gap structures and 5S RNA pol2..... 74

Figure 4.17 Quantification of gap structures. 75

Figure 4.18 Quantification of gap structures after serum starvation. 76

Figure 4.19 Brief overview of the chromosomal contacts preparation..... 78

Figure 4.20 TIRFM imaging of digested chromatin fragments. 79

Figure 4.21 Digested chromatin spreads prepared with/ without fixation. 80

Figure 4.22 BALM imaging of digested chromatin fragments reveals chromosomal contacts. 81

Figure 4.23 Three-color BALM imaging of chromosomal contacts with 5S RNA pol2 and the transcription factor SRF in serum +/- system. 83

Figure 4.24 Nuclear shape was maintained after cytoplasm removal. 85

Figure 4.25 TIRFM images of digested chromatin fragments with 5S RNA pol2 and the transcription factor YAP under geometric confinement..... 86

Figure 4.26 BALM imaging of digested chromatin fragments reveals YAP targeted chromosomal contacts. 87

Figure 4.27 TIRFM images of digested chromatin fragments with 5S RNA pol2 and the transcription factor SRF under geometric confinement..... 88

Figure 4.28 BALM imaging of digested chromatin fragments reveals SRF targeted chromosomal contacts. 89

Figure 4.29 Nuclear localization of p65 regulated by cell geometry and cytokine treatment. 90

Figure 4.30 TIRFM images of digested chromatin fragments with 5S RNA pol2 and the transcription factor p65 under geometric confinement and cytokine induction. 91

Figure 4.31 BALM imaging of digested chromatin fragments reveals a differential amount of p65 target chromosomal contacts in response to geometric confinement or cytokine induction. 92

Figure 4.32 Color map of the whole set of genes with differential p65 enrichment..... 94

Figure 4.33 EpiTect ChIP qRCR analysis reveals particular genes with differential enrichment of p65 at the promoters in response to geometric confinement or cytokine induction. 95

LIST OF SYMBOLS

5S RNA pol2	Ser5 phosphorylated RNA polymerase II
AP	Anisotropic (rectangle, 1800 μm^2)
APTES	(3-Aminopropyl) triethoxysilane
BALM	Binding Activatable Localization Microscopy
CTs	Chromosome Territories
CW	Chromatin fiber Width
ECM	Extracellular Matrix
FISH	Fluorescence *In Situ* Hybridization
FWHM	Full Width at Half Maximum
GCl	Gap Chromatin length
GCw	Gap Chromatin width
H3K4Me3	Histone H3 Trimethylated at Lysine3
H3K9Ac	Histone H3 Acetylated at Lysine9
HDAC3	Histone Deacetylase 3
HP1α	Heterochromatin protein 1 α
IP	Isotropic (circle, 500 μm^2)
LADs	Lamin-Associated Domains
LINC	Linker of Nucleoskeleton and Cytoskeleton
Lw	Lambda DNA width
MET	Mesenchymal to Epithelial Transition
PALM	Photoactivatable Localization Microscopy
ROXS	Reducing-Oxidizing System
SIM	Structure Illumination Microscopy
STORM	Stochastic Optical Reconstruction Microscopy
TIRFM	Total Internal Reflection Fluorescence Microscopy

CHAPTER1: INTRODUCTION

1.1 Role of extracellular matrix on tissue homeostasis, differentiation, and transcription regulation.

Extracellular Matrix (ECM) signals, in the form of substrate stiffness or geometric constraints, are critical for maintaining tissue homeostasis [1-3]. During vertebrate epithelial branching morphogenesis, deposition of newly synthesized ECM components such as fibronectin, which increases ECM stiffness, promotes the splitting of the epithelial bud. Conversely, degradation of ECM is required for epithelial cells to grow from the side of the duct, resulting in side branching [4]. Abnormal ECM leads to tumor progression. Increase in ECM stiffness in vivo, resulting from deregulated expression of ECM crosslinkers, accelerates cancer cell invasion. In contrast, decrease in ECM stiffness by inhibiting ECM crosslinkers reduces tissue fibrosis [5]. Cells on stiffer substrates have larger spreading area, regulated by focal adhesion formation and actomyosin-dependent cytoskeletal reorganization. Reduction in cell spreading by culturing cells on smaller fibronectin-coated islands induces cell apoptosis. Contrarily, increased cell spreading on larger fibronectin-coated islands accelerates cell proliferation [6]. Moreover, substrate stiffness or geometric constraints regulate stem cell lineage specification. Naïve mesenchymal stem cells (MSC) on soft substrates differentiate into neuronal cells, whereas on stiff substrates MSCs differentiate into bone cells [7]. Another study shows that MSCs cultured on polarized substrates, with high cellular contractility, differentiate into bone cells. On the other hand, less polarized substrates that disrupt contractility guide MSCs into fat cells [8].

Cell geometries induce modular changes in gene expression patterns by spatially confining mouse fibroblasts for 3 hrs. On large polarized substrates the serum response pathway is more active, whereas the inflammatory pathway becomes more active on isotropic substrates with less matrix attachment [9]. During this process, activity of transcription factors is differentially regulated. Transcription factor reporter assays show that serum response element (SRE) is more active in cells cultured on large polarized substrates. In

addition, reduction in matrix induces the nuclear enrichment of histone deacetylase3 (HDAC3), leading to a lower level of histone H3 acetylated at lysine 9 (H3K9Ac), a marker of less compacted chromatin [9]. The differential expression of genes is essential for example in matrix assisted lineage specification [7, 8] as well as embryonic development [10].

1.2 Link between extracellular matrix and nuclear architecture.

ECM dependent mechanotransduction occurs through sensing of the major matrix signals at the level of focal adhesions for example via integrin signaling [11]. Fig. 1.1 shows that ECM signals are transmitted through actin cytoskeleton and then relayed into nucleus across the LINC (Linker of Nucleoskeleton and Cytoskeleton) complex that connects nuclear lamina and actin filaments. Nuclear lamina is associated with heterochromatin directed by GAGA motif, which requires GAGA-binding factor cKrox and HDAC3 [12]. High-resolution map of the tethering sites of the genome with the nuclear lamina shows that the lamin-associated domains (LADs) are generally associated with low gene expression levels [13]. External mechanical signals regulate actin polymerization and depolymerization, resulting in the cytoplasm-to-nuclear shuttling of transcription cofactors such as Myocardin Related Transcription Factor-A (MRTF-A), and Yes-associated protein (YAP) [14, 15]. A very recent paper shows that applying a cyclic stretching force on skin stem cells induced accumulation of emerin at outer nuclear membrane, whereas decreased its localization at inner nuclear membrane. The force-induced redistribution of emerin resulted in the detachment of heterochromatin from the nuclear lamina and promoted local actin polymerization that reduced nuclear actin, leading to transcription attenuation [16]. However, how the ECM signals are integrated into the 3D chromosome architecture to regulate modular gene expressions is still not clear. This is an important question, since transcription factor/cofactor or nuclear actin is not sufficient to systematically explain the differentially regulated transcription programs.

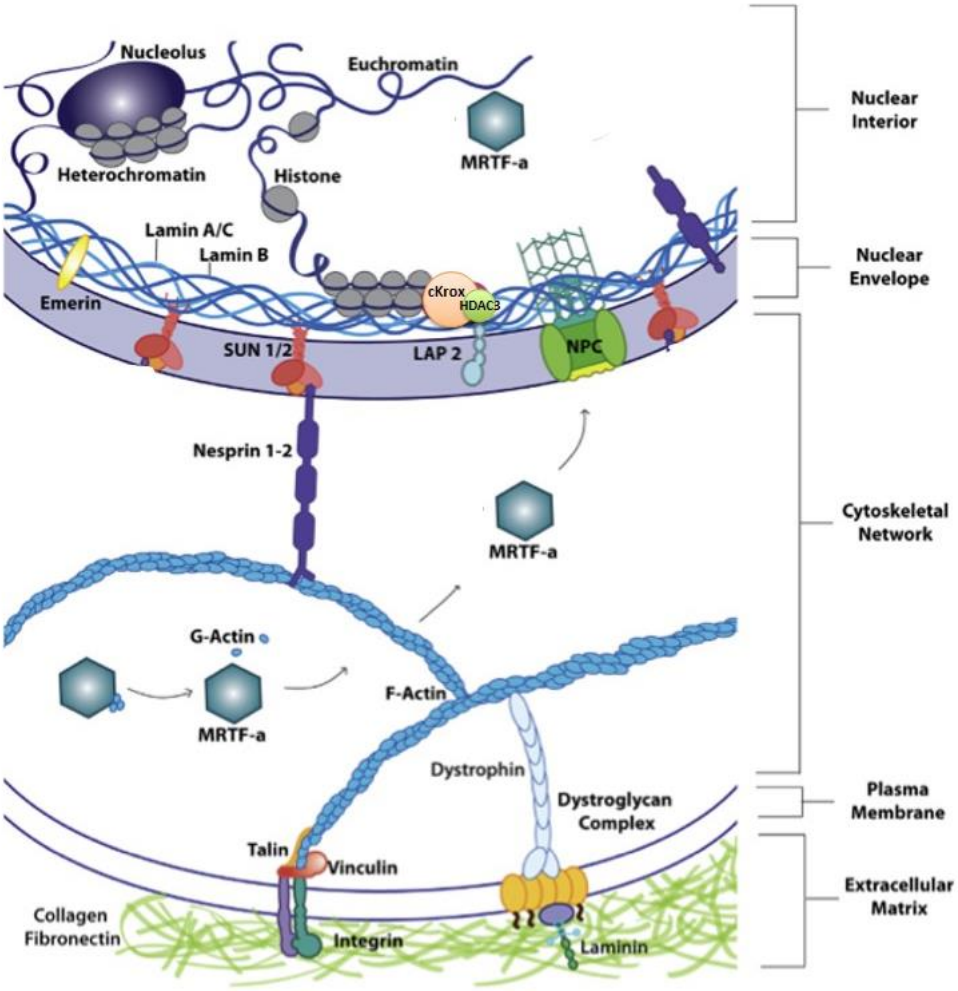

Figure 1.1 Link between ECM and nuclear architecture.

Adapted with permission from Progress in Biophysics and Molecular Biology

1.3 Role of chromatin remodelling and 3D chromosome position on genome regulation

Eukaryotic DNA is packaged, together with histones and non-histone proteins, into chromatin fibers [17, 18]. The fundamental unit of this fiber is the nucleosome [19], which consists of ~150 base pairs of DNA wrapped 1.6 times around an octamer of core histones (H2A, H2B, H3, H4) and sealed with a single linker histone (H1) molecule that is bound closely to the core particle dyad[20, 21]. In interphase cells, chromatin fibers are further packed into higher order structures composed of euchromatin and heterochromatin [22]. Euchromatin is mostly comprised of active genes and gene-rich regions, while repressive

DNA is usually heterochromatinized [23]. The various levels of DNA packaging are mediated by a number of post-translational modifications on both core and linker histones [24, 25]. Modulation of the chromatin structure at promoter sites is required for eukaryotic transcription, and this occurs in a highly regulated manner [26, 27].

In recent years the packing of DNA into three-dimensional chromosome territories (CTs) have been shown to be a critical intermediate to bring about spatial dimensions for genome regulation [28]. Techniques such as fluorescence *in situ* hybridization (FISH) enable the painting of individual chromosome territory. With the help of chromosome FISH it has been revealed that the radial position of chromosomes is correlated with chromosome length and gene density. Gene-poor chromosomes tend to localize at the nuclear periphery, whereas gene-rich chromosomes prefer the interior localization [29]. On the other hand, larger chromosomes are more peripherally localized, whereas smaller chromosomes are more interiorly localized [30, 31]. Defects in Lamin B1 expression or processing alters the radial position of chromosome 18 but not chromosome 19 [32]. The relative position of chromosomes correlates with similar epigenetic states including histone modifications and methylation states, DNase sensitivity, and gene co-expression [33]. Chromosomes with similar transcription activity, defined by the summed expression level of genes on each chromosome, are physically proximal with each other [34]. Intermingling between two chromosomes is transcription-correlated, with the enrichment of 5S RNA pol2, a specific transcription factor and its target gene, as well as histone markers for decompacted chromatin such as H3K9Ac and Histone H3 Trimethylated at Lysine3 (H3K4Me3) [35]. Techniques such as chromosome FISH, chromosome conformation capture assays and theoretical models have revealed that active genes either in *cis*- or *trans*- cluster in specific spatial regions inside the nucleus [36, 37]. Some of these include erythroid-specific immunoglobin genes [38], the Hox cluster [39], and the NF-κB regulated cluster [40, 41]. Moreover, the co-expression of a multi-gene complex requires the physical chromosomal contacts, disruption of which abrogates their co-transcription [41].

1.4 Superresolution imaging of chromatin structures.

Though gene co-clustering has been shown to be important for gene co-regulation with the technique of DNA FISH or RNA FISH [41], the direct visualization of such clusters at the nanoscale resolution is still lacking. The packaging of DNA beyond 10 nm at both euchromatin and heterochromatin regions is also largely unclear.A number of studies have explored the structure of chromatin using electron microscopy [42, 43]. X-ray crystallography studies have described the structure of the nucleosome and the DNA-protein complexes at a resolution of Ångströms [44-48]. Other optical microscopy methods such as confocal microscopy have also revealed chromosome territories at a resolution above hundreds of nanometers [49, 50]. However, these imaging techniques are not able to resolve the structures of transcriptionally active chromatin in interphase nucleus, due to restrictions with electron microscopy labelling methods and the limited resolution associated with conventional light microscopy. Recently, a number of 'super-resolution' strategies were developed that circumvent the usual optical resolution limits [27, 51-54]. One simple yet powerful method that is becoming more widely adapted is 'single-molecule localization microscopy'. This method, which can obtain a lateral spatial resolution of ~20 nm [55-58], involves the repeated imaging of sparse stochastic subsets of fluorophores in a single sample. The position of each fluorophore is determined by finding the center of their point spread function, and this information is used to construct a super-resolution image.

For superresolution imaging of chromatin fibers, stochastic stimulation of a subset of fluorophores is achieved through either tagging histone proteins with photoactivatable fluorescent proteins [57], or incorporating EdU labelled with photoactivatable fluorephores using the 'click chemistry' approach [58], or labelling DNA with a DNA intercalating dye YOYO-1, which shows binding/unbinding kinetics in a specific reducing-oxidizing buffer [59]. With these labelling strategies, it has been found that Drosophila metaphase chromosomes contains fine filaments of ~70 nm [57]. More recently, 3D STORM

combined with oligonucleotide probes has distinguished the structures among active, inactive, and repressed chromatin [60]. However, the direct visualization of gene clusters has still not been achieved, primarily due to the crowded nuclear environment.

1.5 Hypothesis

Based on the aforementioned information, we hypothesized that cell geometry remodels cytoskeletal organization, leading to altered nuclear morphology, which creates different 3D spatial confinements for chromosome position. We further hypothesized that this non-randomly regulated chromosome position would facilitate the formation of specific chromosomal contacts for modular gene regulation.

1.6 Overview of the thesis

Cell Geometry Reorients and Repositions Chromosomes to Regulate Genomic Programs.

This project probes the role of cell geometry on 3D chromosome repositioning and its implications in genome regulation. Mouse fibroblast cells were cultured on fibronectin-coated micropatterns with the shape of either large anisotropic (AP) or small isotropic (IP) for 3 hrs. We observed that cells on large anisotropic substrates were well spread and polarized with enhanced actin stress fibers on top of the nucleus, whereas cells on small isotropic substrates were rounded up with short actin filaments surrounding the nucleus. This resulted in flattened and elongated nuclei on large anisotropic substrates, whereas spherical nuclei on small isotropic substrates. Chromosomes with a wide range of size and gene density were painted using the chromosome FISH technique. Confocal imaging combined with semi-automated MATLAB programming was carried out to measure the 3D morphology and position of these chromosomes. We observed that among 12 painted chromosomes, chromosome 1, 2, and 11 were more interiorly localized in small isotropic substrates compared to large anisotropic substrates, which mimics the physiological

spreading condition of mouse fibroblasts. In contrast, chromosome 3 was more peripherally positioned. Interestingly, we further observed that in small isotropic substrates chromosome 1, 2 and 11 were less compacted and decorated with higher level of Ser5 phosphorylated RNA polymerase2 (5S RNA pol2), an activated form of RNA polymerase II, whereas chromosome 3 was more compacted with less 5S RNA pol2 at the surface of the chromosome.

To further investigate the role of cell geometry on chromosome relative positions, we painted 10 representative chromosome pairs and measured their intermingling degrees on the two substrates. We observed that in small isotropic substrates chromosome 2&6, chromosome 2&10, and chromosome 11&15 intermingled more, whereas chromosome 5&9 intermingled less, compared to those in large anisotropic substrates. The level of 5S RNA pol2 in intermingling regions also changed accordingly. Moreover, inhibition of transcription prevented the increase in intermingling, suggesting that chromosome intermingling was transcription-dependent. Chromosome orientation analysis further revealed that chromosome 2&6, 2&10, and 11&15 were more aligned along the z axis of the nucleus on small isotropic substrates, while chromosome 5&9 chromosomes were preferably aligned along the x axis of the nucleus on large anisotropic substrate. These results suggested that chromosomes that oriented more along the mechanical axis of a nucleus were more sensitive to the cell geometry change. Interestingly, changes in chromosome radial position and orientation between two geometries was not affected by transcription inhibition, emphasizing the role of cell geometry. We next investigated the implications of the chromosome rearrangement in transcription regulation. Chromosome FISH combined with immunostaining or DNA FISH revealed the enrichment of specific transcription factor SRF and its target gene *zyxin* in the intermingling regions. Furthermore, whole-genome transcriptome analysis showed that interiorly moved chromosomes have higher transcription activity and chromosomes that intermingle more have smaller activity distance. Finally, our geometric model of chromosome packing and transcription revealed

that with the optimized transcription-similarity based chromosome arrangement, alteration of nuclear shape could predict the rearrangement or reorientation of chromosomes. Taken together, our experimental observations and modeling efforts reveal a previously unrecognized role of cell geometry on chromosome repositioning for regulating modular genomic programs.

Superresolution Microscopy Reveals Decondensed Chromatin Structure and Chromosomal Contacts At Active Transcription Sites.

To overcome the imaging difficulties rising from the crowded environment of cellular nucleus, in this project we developed an open chromatin spread system combined with superresolution microscopy to visualize interphase chromatin structures at the resolution of ~30 nanometers. Briefly, nuclei were isolated and immunostained with antibodies against active transcription machinery as well as specific transcription factors. The labeled nuclei were then swollen and ruptured by mechanical forces. Chromatin fibers from the nuclei were spread onto glass slides and labeled with YOYO-1, a DNA intercalating dye, for superresolution imaging. The condition of superresolution imaging was optimized using the well-characterized λ-DNA, whose thickness was visualized as ~30 nm using superresolution microscopy, whereas under conventional microscopy the thickness of λ DNA was limited to ~200 nm.

The optimized imaging condition was then applied to visualize the open chromatin spreads. Co-localization of DNA with histone proteins (e.g. H1, H2B), was observed using the TIRFM technique, indicating chromatin fibers in the open spreads were structurally intact after an appropriate nuclear expansion time. Through the use of the BALM technique, a substantial enhancement in resolution of chromatin fibers was attained compared to the TIRFM technique. The most common type of fiber observed via BALM had a width of 150 ±45 nm (mean ± SD), whilst those observed with TIRFM had a width of 450 ±30nm. Structural changes of chromatin in actively transcribing (serum (+)) versus quiescent

(serum (-)) states were also detected using BALM. In the actively transcribing state, chromatin fibers were less compact and featured more gap structures, which were defined as decondensed regions having a length of 388±170nm (mean ± SD) and a width of 60±25nm (mean ± SD). To further check the transcriptional activity of these gap structures, we immunostained phosphorylated 5S RNA pol2 (S5 RNA pol2). Active RNA pol2 is phosphorylated at the 5th serine in the heptad YSPTSPS of the C-terminal domain. This active RNA pol2 is recruited to gene promoters during transcription initiation. Colocalization of RNA pol2 with gap structures implies that these gap structures may be transcriptionally active. Consistent with this, when cell quiescence was induced via serum starvation, the number of gap structures, as well as RNA pol2 signals in those regions, decreased. This method allows us to visualize decondensed chromatin structures at active transcription sites at single cell level. It also provides a robust platform to image the localization of proteins on chromatin fibers.

We further modified this method to directly visualize the functional genomic contacts at the nanometer scale resolution by digesting chromatin fibres into short fragments. Superresolution imaging resolved the short chromatin fragments as structures with more than one DNA fiber associated with 5S RNA pol2 and specific transcription factors. In serum-starved cells, few contacts were observed, whereas the amount of contacts increased significantly upon serum stimulation, indicating the functionality of the observed chromosomal contacts. We directly visualized specific chromosomal contacts, in particular those targeted by transcription factors/cofactors such as YAP (Yes-associated protein), SRF (Serum Response Factor), and NF-κB. Moreover, for cells with various geometric confinements or cytokine treatments, we observed differential levels of specific contacts. It is worth noting that, by seeding cells sparsely onto a glass slide, we were able to image chromosomal contacts from one cell without mixing contacts from other cells. Hence, this method also allows us to reveal heterogeneity in the level of the specific contacts from cell to cell. In summary, we developed a novel open chromatin spread system combining with

existing superresolution microscopy methods to visualize decondensed chromatin and functional chromosomal contacts at a nanometer resolution. This method opens up a new venue to image the physical chromosomal contacts at a nanometer resolution. It also provides evidence for the existence of transcription-dependent chromosomal contacts, which are sensitive to cell geometry changes.

CHAPTER2: METHODS AND MATERIALS

Cell culture and micropatterning. NIH 3T3 fibroblast cells were cultured in low glucose Dulbecco's modified Eagle's medium (DMEM, GIBCO, New York, USA) supplemented with 10 % fetal bovine serum (FBS, Gibco) and 1 % (vol / vol) penicillin streptavidin (GIBCO, New York, USA) at 37 °C in 5 % CO_2. 65,000 cells were seeded for 10-15 min on fibronectin coated microfabricated patterns, the preparation of which was described in previous work from our lab [9]. Non-adhered cells were removed and the remaining cells were washed once with DMEM, and incubated for 3hrs at 37 °C in 5 % CO_2.

Chromosome FISH combined with Immunostaining on fibronectin-coated patterns. NIH3T3 cells were cultured for 3 hours on fibronectin-coated microfabricated patterns that were printed on cleaned glass slides spin coated with PDMS prior to this. For the transcription inhibition experiment, 40 μg/ml α-amanitin (Sigma Aldrich, USA) was added to patterned cells and treated them at 37 °C in 5 % CO_2 for 3 hrs. For the cytokine treatment experiment, patterned cells were treated with 25 ng/ ml TNF-α (Sigma Aldrich, USA) for 30 min. For the Jasplaknolide treatment experiment, 500 nM Jasplakinolide (Sigma Aldrich) was added to patterned cells for 30 min. Cells were then washed with 1× PBS to remove cell culture medium followed by incubation on ice for 5-8 minutes, with 0.25 % Triton in CSK buffer (100 mM NaCl, 300 mM Sucrose, 3 mM MgCl2, 10 mM PIPES with pH 6.8). Cells were then fixed with 4 % PFA (Paraformaldehyde) for 10 minutes, briefly rinsed with 0.1 M Tris-HCl followed by 1× PBS wash. This was followed by permeabilization with 0.5 % Triton for 10-15 minutes. Overnight incubation in 20% glycerol at 4 °C, and then 5 - 6 freeze-thaw cycles in liquid nitrogen followed. After this, cells were washed with 1× PBS a few times, before and after treatment with 0.01 % HCl for 5-10 minutes, followed by digestion with 0.002 % porcine pepsin (Sigma Aldrich, USA) in 0.01N HCl at 37 °C for 4 minutes. Cells were then fixed with 1 % PFA for 4 minutes, briefly rinsed in 1× PBS before being treated with RNase (from Promega, USA, 200 μg/ml made in 2× SSC-0.3M sodium chloride and 30mM trisodium citrate) at 37°C for 15-20 minutes. The cells were then washed with 2× SSC and equilibrated in 50 % Formamide / 2× SSC [(pH 7.4)

overnight at 4 °C. Hybridization was set up the following day. Chromosome paints (Chrombios, Germany) tagged with different fluorophores were thawed to room temperature, and mixed with hybridization buffer provided by the supplier. Cells were denatured in 50 % Formamide / 2× SSC at 85 °C for 2-3 minutes and then incubated with the fluorescently labeled mouse chromosome FISH probe mix; the slides were then sealed with a Sigmacote (Sigma) coated hydrophobic coverslip and rubber cement to incubate overnight in a moist chamber at 37 °C with shaking. At the end of the incubation period, slides were washed thrice each in 50 % Formamide / 2× SSC at 45 °C and 0.1× SSC at 60 °C. After the last stringent wash with the 50% Formamide made in 0.1× SSC at 45°C, the nuclei were blocked in 5% BSA solution made in 2× SSC and then subjected to primary and the secondary antibody diluted in 5% BSA solution made in 2× SSC. If indirect labels like chromosome probes conjugated with biotin, digoxigenin [DIG] are used during hybridization, detection step also involved use of fluorophore labeled streptavidin/avidin, anti-DIG. The primary antibody used here is: RNA Polymerase II CTD repeat YSPTSPS (phospho S5) (Abcam - ab5131, 1:500), Serum Response Factor, SRF (sc-335, Santa Cruz biotechnology, USA, 1:100), Mouse monoclonal [21H8] to Digoxigenin, DIG (Abcam-ab420; 1:500). Finally, cells were counterstained with Hoechst 33342 (Sigma, USA) for 10 minutes and then mounted with Prolong Gold antifade mounting medium (Life Techonlogies, USA), sealed with a coverslip, and imaged.

Confocal laser scanning microscope imaging for chromosome FISH samples. Slides for chromosome FISH were scanned using Nikon A1 Confocal microscope (Nikon, USA) with a 100×, 1.4 NA oil objective. The axial distance between light optical sections was set as 200 nm. For each optical section, images were collected sequentially to minimize crosstalk between different fluorochromes. The pinhole size was set as 1 airy unit. Stacks of 16-bit gray scale two-dimensional images were obtained with a pixel size of 80 nm in XY direction, and used for the quantitative evaluation.

Image analysis.

1. Normalized radial distance

To estimate the radial distance of each chromosome, the coordinates for nuclear centroids (O) and chromosome centroids (C1), as well as nuclear surface were obtained from 3D thresholded images. The absolute radial distance of the chromosome was first computed (d_{OC1}). To find out the radial position of the chromosome relative to the nuclear envelope, we also measured the nuclear radius where the chromosome sits, by drawing a line passing through the chromosome and nuclear centroids, and then intersect with the nuclear surface (B1). The nuclear radius was defined by the distance between the nuclear centroids and the intersection point (d_{OB1}). Normalized radial distance was defined as

$$Normalized\ radial\ distance = \frac{d_{OC_1}}{d_{OB_1}}$$ (See Figure 2.1A)

2. Chromosome decompaction factor

In order to estimate the chromosome decompaction factor, the sequence length for all the painted chromosomes was obtained from National Center for Biotechnology Information, USA (NCBI, http://www.ncbi.nlm.nih.gov/genome/guide/mouse/; August 2013). The chromosome decompaction factor was defined as,

$$Chromosome\ decompaction\ factor = \frac{Norm\_V_{CT}}{L_{CT}\ (Mbp)} \times 10^4$$ (See Figure 2.1B)

Where, $Norm_V_{CT}$is normalized chromosome volume and L_{CT} is chromosome length in Mega base pair (Mbp).

3. Intermingling degree

To compute the intermingling degree, the intermingling volume ($V_{1\&2}$) between two chromosomes was first estimated. To estimate the intermingling volume, the thresholded images of the two chromosomes were multiplied, and only the overlapping region resulted in pixels with value of 1. The number of pixels with value 1 represents intermingling volume. The intermingling degree was then defined as the intermingling volume

normalized to the volume of the two chromosomes and their homologues (V_1, $V_{1'}$, $V_{1''}$, V_2, $V_{2'}$, $V_{2''}$),

$$Intermingling\ degree = \frac{V_{1\&2}}{V_1+V_{1'}+V_{1''}+V_2+V_{2'}+V_{2''}}$$ (See Figure 2.1C)

4. 3D Chromosome orientation mapping

To map all the chromosome 3D orientations in large anisotropic (AP) and small isotropic (IP) substrates, coordinates for 3D CT surface were obtained, followed by searching on the surface for the point that had the largest distance to the CT centroid. The centroid and the far most point on the CT surface determined the vector $\overrightarrow{V1}$. Another vector ($\overrightarrow{V2}$) was defined by the nuclear centroid and any point on the line passing through the nuclear centroid and a line parallel to the X-axis or Z-axis. γ_x or γ_z was defined as,

$$\cos(\gamma_x\ or\ \gamma_z) = \frac{\overrightarrow{V1}\cdot\overrightarrow{V2}}{|\overrightarrow{V1}|\cdot|\overrightarrow{V2}|}$$ (See Figure 2.1D)

5. 5S RNA pol2 distribution on a chromosome

To analyze the spatial distribution of 5S RNA pol2 on a chromosome, images of 5S RNA pol2 were preprocessed by applying a Fourier high pass filter to remove background noise and to highlight the bright features. Subsequently, 3D erosion was applied on each chromosome, which divided one chromosome into 3 shells with the same thickness. Fraction of the bright features for 5S RNA pol2 in each shell was then quantified.

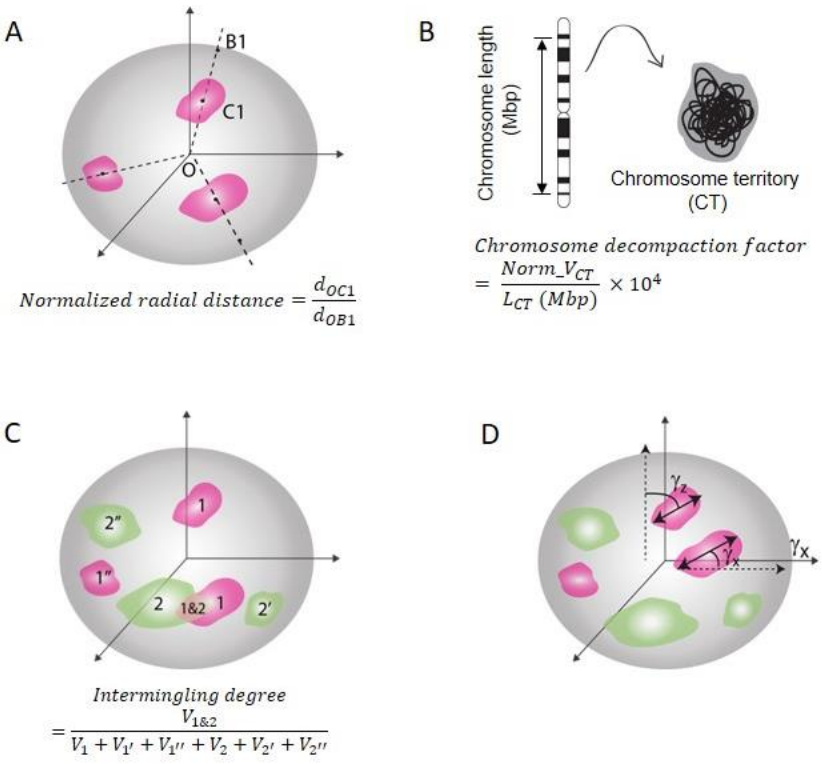

Figure 2.1 Schematic description of the quantities.

(A) Schematic description of radial distance measurement, where *d* refers to the distance between two points. (B) Schematic description of Chromosome Decompaction Factor measurement, where *Norm_V*$_{CT}$ refers to the normalized chromosome volume, and *L*$_{CT}$ refers to chromosome length. (C) Schematic description of intermingling degree measurement, where *V* refers to the volume of one homologous or heterologous chromosome, or the intermingling regions between two heterologous chromosomes. (D) Schematic description of γ_x and γ_z measurement.

Serum starvation and stimulation assay

Wild type HeLa cells and HeLa cells stably transfected with fusion plasmid for core histone H2B tagged with EGFP [61] were cultured in Dulbecco's modified Eagle's medium (DMEM, Gibco, New York, USA) supplemented with 10% fetal bovine serum (FBS, Gibco) at 37 ℃ in 5% CO_2. To subject cells to serum starvation, cells were cultured in DMEM without FBS at 37 ℃ in 5% CO_2 for 36 hours. For NIH3T3 cells, they were starved by culturing them in low glucose Dulbecco's modified Eagle's medium (DMEM, GIBCO, New York, USA) supplemented with 1 % fetal bovine serum (FBS, Gibco) and 1 % (vol/vol)

penicillin streptavidin (GIBCO, New York, USA) at 37 ℃ in 5 % CO_2 for 36 hrs. Serum stimulation was achieved by replacing the serum-poor DMEM with normal DMEM supplemented with 10% FBS for 12 hrs.

Nuclei isolation and chromatin spreads

HeLa cells were suspended in Phosphate Buffered Saline (PBS) after a brief treatment with Trypsin (Gibco). Cells were collected by centrifugation at 200×g and re-suspended in cell rupturing buffer TM2 containing 2 mM $MgCl_2$, 10 mM Tris-HCl (pH 7.4), 5 mM PMSF (Sigma, USA) with 1% Triton X-100 for 4-5 minutes at 4 ℃. The nuclei were separated as pellet from the ruptured cytoplasm by centrifugation for 2 minutes at 400×g. The pelleted nuclei were separated from each other by rigorous tapping and stored in 1× PBS containing 1× protease inhibitor cocktail (Roche, Germany) [62]. Nuclei were allowed to settle on polysine-coated slides (MENZEL-GLASER Polysine® J2800AMNZ, Thermo Scientific, Germany) for 30 minutes by confining them in PDMS (DOW CORNING CORPORATION, USA) wells. Attached nuclei were swollen with deionized (DI) water and burst under a moderate pressure exerted through an 18×18 mm coverslip that was cleaned in detergent with ultrasonication for 30 min. The coverslip was sealed with appropriate imaging buffer (described later) on the slide and then subjected to imaging.

To prepare digested chromatin spreads, after NIH3T3 cells were treated with serum starvation/ stimulation, geometry confinement, or cytokine induction, the cytoplasm was removed by incubating cells with lysis buffer containing 2 mM $MgCl_2$, 10 mM Tris-HCl (pH 7.4), 1X protease inhibitor cocktail, and 1 % Triton for 2 min on ice. Isolated nuclei were gently washed with digestion buffer twice, followed by incubating nuclei with FastDigest HindIII (Thermo Fisher Scientific, USA) containing 1X protease inhibitor cocktail for 20 min at 37 ^{o}C.

Labeling of transcriptionally related proteins and chromatin fibers

DNA-associated proteins were labeled with antibodies in isolated nuclei before the swelling process. For immunolabeling, isolated nuclei were incubated in blocking reagent (1% BSA in PBS), followed by primary antibody and secondary antibodies diluted in blocking reagent, each for ~30 min at room temperature. Linker histone H1 (Upstate 05-457, Merck Millipore), transcriptionally active CTD phosphorylated RNA pol II (ab5131, Abcam, UK, or Millipore- 04-1572), NF-κB p65 (Cell Signaling Technology, 8284), YAP1 (Abcam ab56701), and Serum Response Factor SRF (sc-25290, Santa Cruz biotechnology, USA) were immunolabeled on chromatin fibers or digested chromatin fragments.

Labeled nuclei were then swollen with deionized (DI) water for 10-30 min. DNA, which existed as chromatin fibers or digested chromatin fragments prepared as described above, was labeled with either 1 μg/ml Hoechst 33258 (Sigma-Aldrich, USA) diluted in 1X PBS or 100 ng/ml of YOYO-1 (Invitrogen, USA) diluted in freshly made ROXS buffer (50 mM Tris-HCl, 50 mM NaCl, 1 mM EDTA, 1 mM Methyl viologen (Aldrich, USA), 10 mM L-Ascorbic acid (Sigma, USA), pH7.5) and mounted in ROXS buffer [63] for imaging. For H2B-EGFP transfected HeLa cells, chromatin fibers were visualized in reducing buffer: 10mM PBS (pH 7.4), 0.5 mg/ml glucose oxidase (Sigma), 40 μg/ml catalase (Sigma), 10% w/v glucose (Fischer Scientific), and 50 mM β-mercaptoethylamine (MEA, Fluka).

λDNA stretching

Pre cleaned 22×22 mm coverslips were rendered positively charged by coating with (3-Aminopropyl) triethoxysilane (APTES, Sigma-Aldrich, USA). Then, 1μg/ml of λ DNA (BioLab, New England) stained with YOYO-1 (at a dye/bp ratio of 1/150) was added onto the coverslips and incubated for ~30 min, allowing attachment of λDNA via one or more sites on the coverslip. The stretching of λDNA was achieved through capillary effect created by the rapid absorption of the buffer by tissue paper followed by the force caused by the surface tension of the receding liquid surface [64].

Super-resolution imaging

Super-resolution imaging was performed on a Zeiss Elyra P.1 microscope, equipped with an oil-immersion objective (alpha "Plan-Apochromat" 100X/1, 46 Oil DIC) and Total internal fluorescence (TIRFM) illumination. TIRFM illumination was achieved by using lasers with motorized TIRFM angle adjustment. The resulting illuminated area was 51.1×51.1 μm (with alpha "Plan-Apochromat" 100×/1.46 Oil DIC, full chip recording). Excitation was provided by a 488 nm laser line (100 mW) with AOTF-based intensity control. Emitted fluorescence was collected by the same objective and captured by an Andor iXon 897 back-thinned EMCCD camera. Integration time per frame was 50 ms at full laser power. Typically 10,000 frames were collected, which corresponded to measurement duration of ~10 min. XY drift and alignment differences between different channels were corrected by localizing 0.2-μm TetraSpeck™ beads (Invitrogen, USA) immobilized on the sample coverslip.

Super-resolution data analysis

Raw data was processed using Zeiss Zen software to detect single-molecule events above background noise. A Gaussian filter and a Laplace filter were applied to every event of single molecule fluorescence in each frame of the raw image to reduce noise and enhance the detection of events. The image mean (M) and standard deviation (S) were then computed. Single-molecule events were defined when the peak intensity (I) satisfies:

$$I - M > S \times SNR \quad (1)$$

Where, SNR is a user-definable signal-to-noise ratio. The area to be analyzed around each event was typically set to 9 pixels. Events with overlapping PSFs were kept in order to localize the TetraSpeck™ beads for alignment. Gaussian fit was chosen as the method to calculate the center of detected PSFs. After reconstruction, a super-resolution image and a table containing the x-y coordinates of all the single-molecule events (and other details, notably the precision of each localization) were obtained. A typical super-resolution acquisition of YOYO-1-labeled chromatin contained from one hundred million to several

billion total detected events. In the post-processing step, events which were above the 20 nm localization limit were discarded. A super-resolution (SR) image was generated by fitting each event with the Gaussian function, and binning the number of localizations with a bin size of 10 nm. The exported SR images were then processed in MATLAB and ImageJ and the morphological features of the spread were established.

Spatial correlation analysis

A high-pass filter was applied in the Fourier domain of the reconstructed super-resolution image of chromatin fibers. This resulted in an image with only periodic node structures along a fiber, which originally existed together with other random structures in chromatin. A pixel-wise autocorrelation analysis was then carried out to determine the compaction of chromatin structures. To obtain characteristic length scales, the starting point of the fiber was set zero, each mean intensity value along the fiber was used as a signal to calculate the autocorrelation function

$$g(r) = \frac{\langle (I(r)) \times (I(r+r_0)) \rangle}{\langle (I(r))^2 \rangle} \quad (2)$$

Where $I(r)$ is the mean intensity value at position r, and r_0 is the step moving along the fiber. The averaged autocorrelation $g(r)$ was obtained from fibers with the length of 2 μm ($n \geq 15$). The data analysis here was carried out using LabVIEW 6.1 (National Instruments) and graphs were plotted in Origin 8.0 (OriginLab).

Chromosome contact pull down and EpiTect ChIP qPCR

a) Fixing and preparation for immunostaining

NIH3T3 cells (approximately one million) that were geometrically confined, and treated with cytokines, were fixed with 2% formaldehyde for 5 min at room temperature (RT) followed by quenching with 127 mM glycine for 10 min at RT. Cells were washed with Phosphate-buffered Saline (PBS). The nuclei were prepared in lysis buffer (10 mM Tris-HCl (pH 8), 10 mM NaCl, 0.2% IGEPAL CA-630(Sigma)) with protease inhibitor cocktail

(Roche) for 30 min on ice with intermittent agitation. Nuclei were washed with 1x Fast Digest (FD) buffer (Thermo Fisher Scientific). 400 µl of 1 x FD buffer and 6 µl of 20% SDS was added to the nuclei and incubated at 37˚C for 60 min with constant agitation. 40 µl of 20% Triton X-100 was added and incubated at 37˚C for 60 min with constant agitation. 30 µl of HindIII (50 U/µl; Thermo Fisher Scientific) was added and incubated at 37˚C for overnight with constant agitation. Nuclei were washed with PBS and blocked with 5% BSA for 1 hr at RT before being immunostained. Nuclei were washed with 5% BSA, scraped and collected in a tube.

b) Coupling with beads

Dynabeads coupled with Anti-Rabbit secondary antibody (M-280; Thermo Fisher Scientific) were resuspended in 1 ml of Washing Buffer (Ca2+ and Mg2+ free (PBS), supplemented with 0.1% bovine serum albumin (BSA) and 2 mM EDTA, pH 7.4). With the help of a DynaMag™-2 Magnet, the Dynabeads were washed. 5% BSA and NF-κB p65 Rabbit mAb (Cell Signalling Technology) were added to the beads and incubated with gentle tilting and rotation at RT for one hour. The unbound NF-κB p65 Rabbit mAb was removed using a DynaMag™-2 Magnet. Dynabeads were washed with 5% BSA to ensure all unbound NF-κB p65 Rabbit mAb was removed.

These Dynabeads were then resuspended in the nuclei in 5% BSA and incubated for over 12 hours at 4℃. The product obtained after the incubation was a tertiary complex comprised of Dynabeads coated with Anti-Rabbit secondary antibody, bound to NF-κB p65 Rabbit mAb, which was further bound to chromatin associated with NF-κB p65. The beads were washed with PBS, to ensure that the chromatin that was not associated with NF-κB p65 was washed off.

c) Reverse crosslinking

Reverse crosslinking was performed by incubating the pulled-down contacts with 5µl of Proteinase K (PK; Thermo Fisher Scientific) in 200µl of PK buffer (30mM Tris (pH8.0), 10mM EDTA, 1% SDS) incubated at 65˚C for at least 90 min. Using DynaMag™-2 Magnet the supernatant was separated from the Dynabeads. 50 µL of PK buffer was added to the bead fraction to elute any remaining DNA. The supernatant collected was purified using Qiagen PCR clean up to concentrate the DNA. This DNA was further amplified using REPLI-g Single Cell Kit (Qiagen). The amplified DNA was analysed using EpiTect ChIP qPCR array (Qiagen).

Immunostaining, and colocalization analysis. Cells were seeded on fibronectin-coated microfabricated patterns that were printed on uncoated dishes (ibidi, Germany) for 3 hrs. Cells were rinsed three times with 1X PBS, followed by fixation using 4% paraformaldehyde (Sigma) in 1X PBS for 10 min. Cells were washed and permeabilized with 0.5 % Triton-X (Sigma, USA) in 1X PBS for 15 min. After washing thrice with 1X PBS, the cells were treated with 1 % BSA (blocking solution) for 1 hrs. This was followed by incubation with required primary antibodies. The primary antibodies [RNA polymerase II CTD repeat YSPTSPS (phospho S5) (1:500, 04-1572, Merck, USA), NF-κB p65 (1:300, 8242S, Cell Signaling Technology), serum response factor (SRF) (1:100, sc-335, Santa Cruz Biotechnology, USA), myocardin-related transcription factor (MRTF-A) (1:100, sc-21558, Santa Cruz Biotechnology, USA)], Lamin A/C (1:1000, abcam 8984), phalloidin 561(ThermoFisherScientific, USA), and Lamin B1 (1:300, abcam16048) were used to stain RNA polymerase II CTD repeat YSPTSPS phosphorylated at serine 5, total p65, total SRF, MRTF-A, Lamin A/C, and Lamin B1 respectively. Cells were washed with 1X PBS and incubated with the corresponding secondary antibody. The nuclei were labeled with Hoescht-33342 (1mg/mL; 1:500) for 10 min.

Images of fully adhered single cells were captured with a Nikon A1R microscope using a 100x, 1.4 NA oil objective. Imaging conditions were kept similar in all of the experiments. To estimate protein levels and localizations, fluorescence images were captured on confocal

microscope using a 100x objective, 3x magnification, and z-step of 500 nm. Nucleus to cytoplasmic ratio (N/C ratio) of MRTF-A and p65 was calculated by dividing the total nuclear level with the cytoplasmic level of MRTF-A and p65. Fluorescent images of 5S RNA pol2, SRF, MRTF-A, and p65 were threshold to a proper extent for colocalization analysis. The colocalization analysis was carried out using a customized MATLAB program, in which the 3D nucleus was divided into multiple 3D boxes with xy width of 340 nm, and z height of 1 μm, within the confocal resolution limit. The fraction of colocalization was calculated by the number of boxes containing signals of the two or three proteins divided by the total number of boxes inside the nucleus.

Structured Illumination Microscopy (SIM) imaging and image analysis. SIM imaging was performed on a Nikon N-SIM, equipped with a Nikon Ti-E motorised inverted microscope with perfect focus system. The samples were imaged with a 100x 1.49 NA objective and an Andor DU-897 X-6219 camera (Andor Technology PLC, Northern Ireland). SIM images were acquired with 488 nm and 561 nm excitation lasers. Images were acquired in 3D SIM mode (for each SIM image 15 images with five different phases of three different angular orientations of illumination were collected) and z-stacks were collected with a step size of 0.24 μm. Collected SIM raw images were processed with the Nikon Elements software. The reconstruction parameters were optimized to be: Structured illumination contrast = 0.5; Apodization Filter = 1.0; Width of 3D-SIM filter = 0.05. SIM images of ~20 cells were acquired for each condition. Images were further processed in ImageJ (NIH, Bethesda, MD).

Western blotting. NIH 3T3 cells were seeded for three hours on 80 mm petri dishes coated with fibronectin patterns. After that, cells were scraped off in 1X PBS and spun down at 650 rcf for 8 min. Supernatant was discarded, and the sediment was mixed thoroughly with RIPA buffer [150 mM NaCl, 50 mM Tris-HCl pH 7.3, 0.25 mM EDTA, 1% (w/v) sodium deoxycholate, 1% (v/v) Triton X-100, 50 mM NaF, 5 mM sodium orthovanadate, protease inhibitors (Roche Applied Science)] on ice. The lysates were clarified by centrifugation at

15, 000 rpm for 10 min at 4 ℃. The extracted proteins were separated by SDS-PAGE and transferred to immobilon transfer membrane (Millipore) for western blotting analysis. The primary antibodies were anti- Lamin A/C (abcam8984, 1:1000), anti- Lamin B1 (abcam16048, 1:1000), anti-GAPDH (sc-32233, 1:1000).

Lamin A/C overexpression (OE) and knock down (KO) experiments. The plasmid Lamin A/C fused with GFP was transfected into NIH 3T3 cells using electroporation. Lamin A/C knockout (KO) and control MEF stable cell lines were kind gifts from Colin L. Stewart. NIH 3T3 cells overexpressing Lamin A/C were trypsinized after 24 hrs of transfection and seeded on circular patterns for 3 hrs, and Lamin A/C KO MEF cells were seeded on rectangular patterns for 3 hrs, followed by FISH procedures.

Statistical analysis. Statistical significance between AP and IP groups was tested using a two-sided Student t-test when the data followed a normal distribution. Otherwise, the Mann-Whitney test was applied. We repeated experiments for a minimum of three times with large enough sample size n for each repeat to be confident that the reported results are representative.

CHAPTER3: CELL GEOMETRY REORIENTS AND REPOSITIONS CHROMOSOMES TO REGULATE GENOMIC PROGRAMS.

3.1 Cell geometry influences the normalized volume and the normalized radial distance of chromosomes.

NIH 3T3 cells were cultured on glass slides with fibronectin micropatterns. Micropatterns were either anisotropic (AP) rectangular (aspect ratio 1:5, area: 1800 μm^2), or isotropic (IP) circular (area: 500 μm^2) substrates (Figure3.1A). The size of AP patterns is similar to the physiological spreading area of NIH 3T3 cells on fibronectin (1,300 ± 30 μm^2) [9], while IP patterns were used to relax the prestress experienced by cells in AP patterns. As a control, cells on AP substrates have long actin stress fibers and more flattened elongated nuclei, whereas cells on IP substrates have short actin filaments and more spherical nuclei with smaller nuclear maximum projected area and larger nuclear height. In addition, the nuclear volume reduced in IP substrates (Figure 3.1).

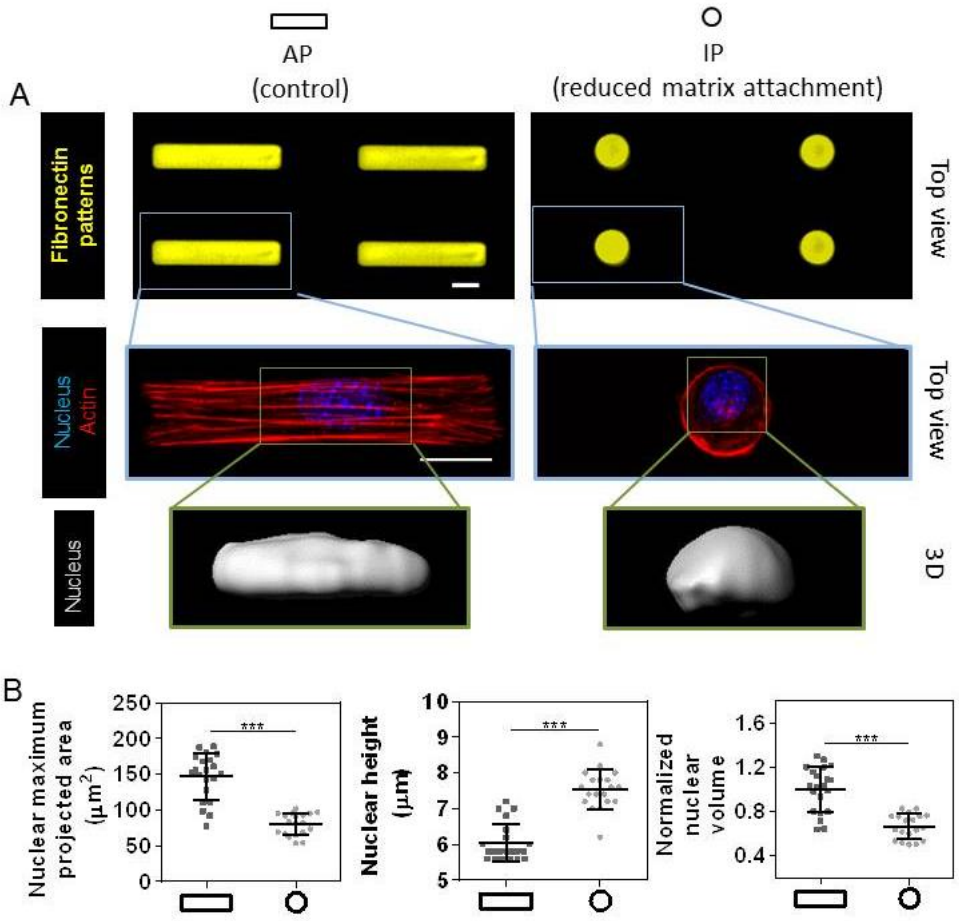

Figure 3.1 Effects of cell geometry on cytoskeleton organization and nuclear morphology.

Low magnification images of fibronectin patterns (yellow). Scale bar: 20 μm. Representative confocal images of NIH 3T3 cells labeled with phalloidin (red) and Hoechst (blue) cultured on these patterns. Scale bar: 20 μm. Images below are Imaris generated surface plot of nucleus in AP and IP substrates. (B) Dot plot quantifying the nuclear maximum projected area, nuclear height, and normalized nuclear volume in AP and IP substrates. Data is presented as mean ± SD with $20 < n < 30$. *** $P < 0.001$. Two sample student's t test.

Next we assessed the consequences of cell geometry changes on the spatial organization of chromosomes using fluorescence *in situ* hybridization (FISH) by painting 12 representative chromosomes (CTs) covering a wide range of chromosome lengths and gene densities (Figure3.2).

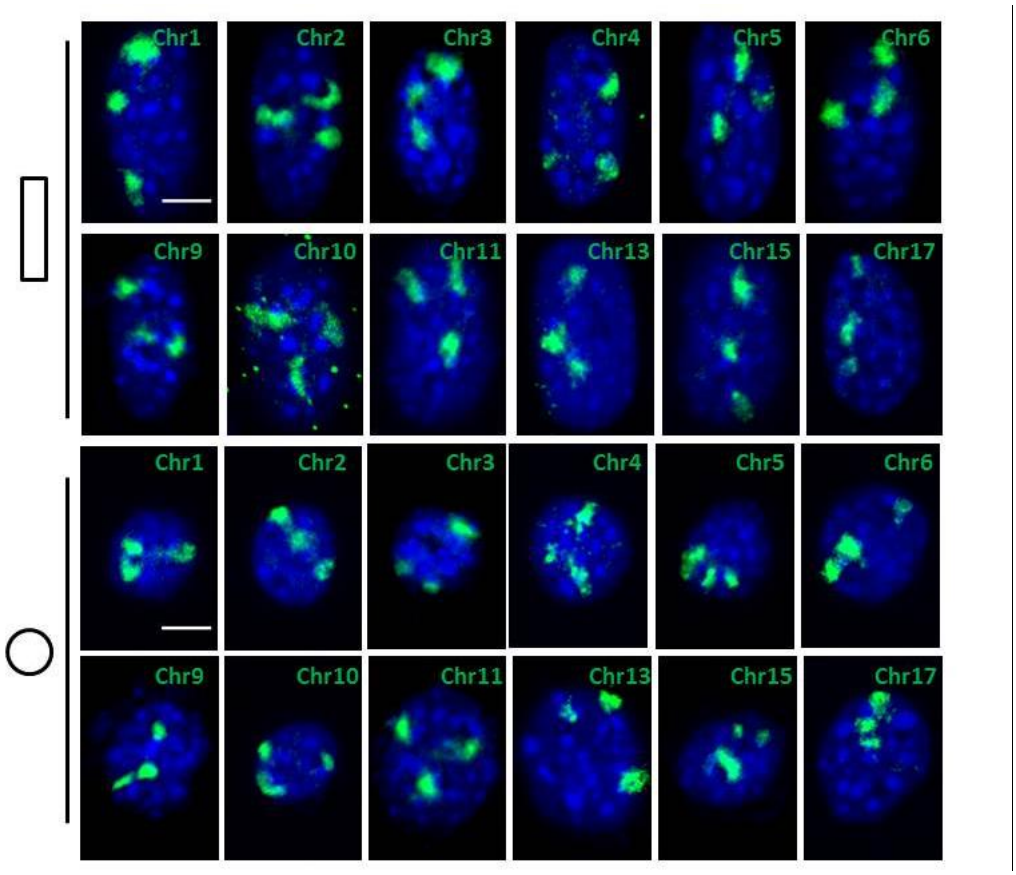

Figure 3.2 Representative images of painted 12 chromosomes and nucleus.

To quantitatively measure the morphology of the nucleus and chromosomes, as well as the chromosome postitioning in the three-dimensional nuclear architecture, z stacks of confocal FISH images were taken, followed by careful thresholding of the stack of confocal slices. A semi-automated algorithm written in MATLAB (Mathworks, USA) was used to analyze

3D chromosome FISH images, where both nuclei and chromosomes were manually selected according to the signal distribution on the Z-maximum projected images. Maximum projected masks for nuclei and chromosomes were then generated. This was used to multiply the entire Z-stack of the nucleus and chromosome to remove the background noise, which would otherwise undermine the thresholding accuracy. For 3D thresholding, the mean and standard deviation of intensity was computed throughout the entire Z-stack. The criteria for setting a pixel as 1 or 0 is based on the mean ± (standard deviation × a), where a is a value to adjust the criteria. Pixels above mean ± (standard deviation × a), were set as 1, and those below were set as 0. The thresholding procedure was monitored by superimposing the outline of the thresholded object with the original object (Figure 3.3). This resulted in best 3D masking for both nucleus and chromosomes, which is critical for quantification of the following parameters.

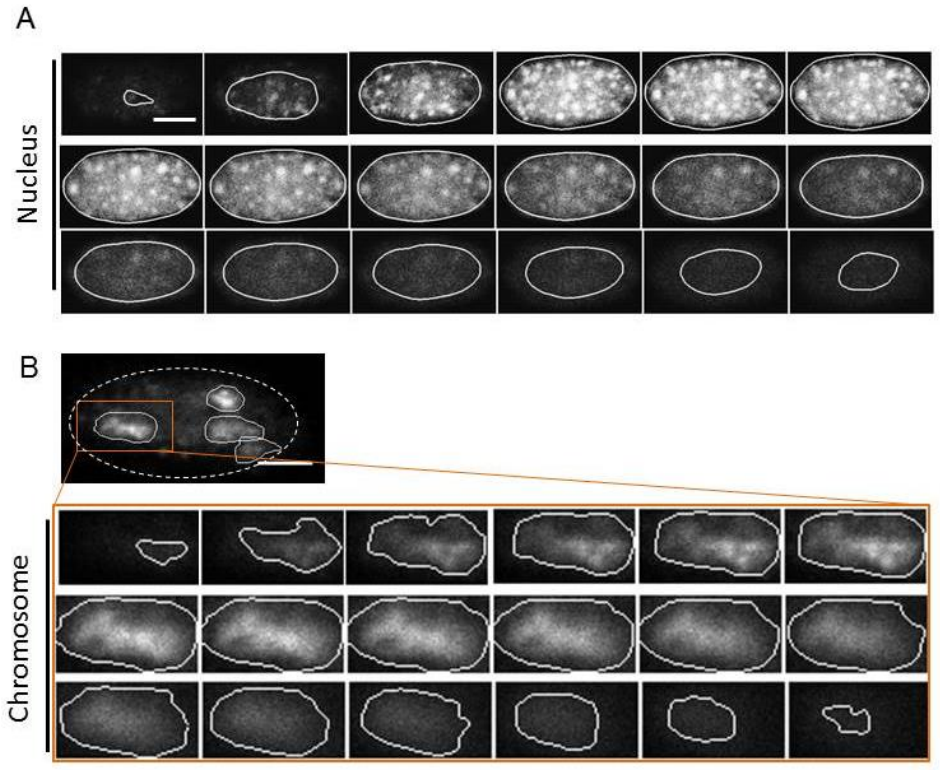

Figure 3.3 Monitoring of the 3D image thresholding.

(A) Merge of the confocal slices of the original nucleus and the boundary of the segmented nucleus. (B) Merge of the confocal slices of the original chromosome and the boundary of the thresholded chromosome.

Since most CTs are smaller in IP substrates simply due to the smaller nuclear volume (Figure 3.1B, Figure. 3.4A), we computed the normalized CT volume with respect to nuclear volume: chromosome (Chr) 2, 4 and 15 showed an increased normalized volume, while Chr 3, 5 and 9 showed a decreased normalized volume in IP substrates, compared to those in AP substrates (Figure. 3.4B).

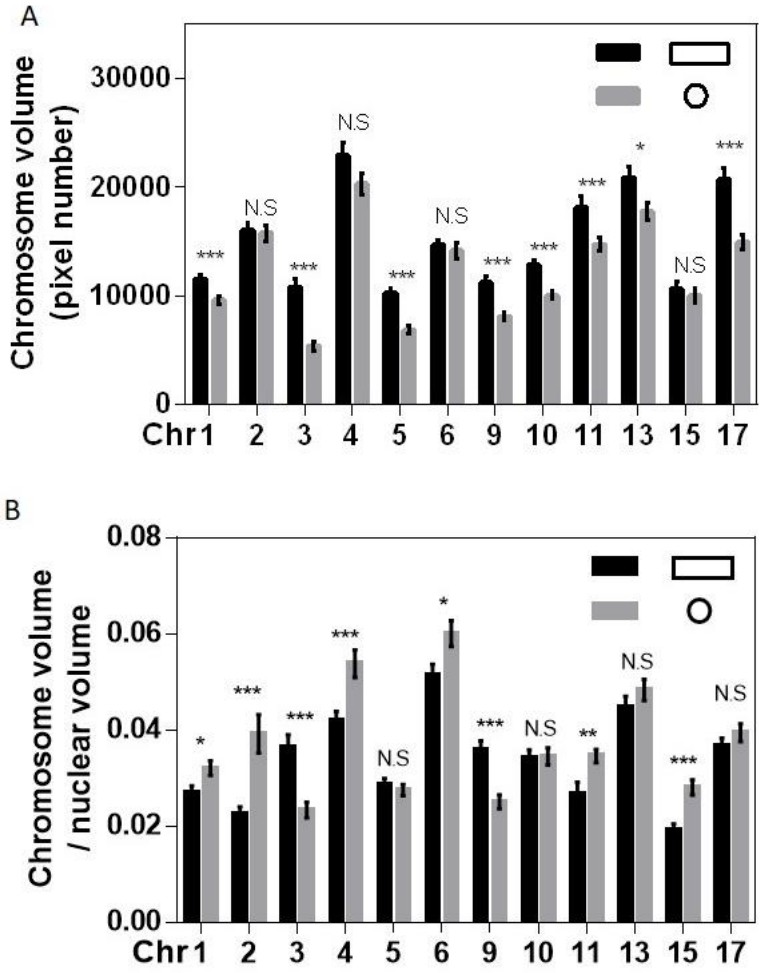

Figure 3.4 Bar graph quantifying the absolute and normalized chromosomes volume.

Data is presented as mean ± SE with 50 < n < 80. *** $P < 0.001$, ** $P < 0.01$, * $P < 0.05$. N.S. refers not significant. Mann-Whitney U test.

Next we computed the normalized radial distance of each CT centroid to the nucleus centroid as depicted in Figure 2.1A and explained in Materials and Methods. We found that

Chr 1, 2, 11 significantly decreased radial distances, and Chr 3 increased radial distance in IP substrates compared to those in AP substrates (Figure 3.5A). Furthermore, a combined analysis of Figure 3.4B and Figure 3.5B shows that Chr1, 2, and 11 that moved towards the nucleus centroid in IP cells were less compacted compared to AP cells. In line with this, Chr3 that moved towards nuclear envelope were more compacted, while Chr5 with similar radial distance in both geometries did not show significant difference in chromosome compaction (Figure 3.5B). These results suggest that cell geometry regulates radial position of specific CTs accompanied with chromatin remodelling, as reflected by the change in normalized chromosome volume. We next analyse the consequences on transcription activity.

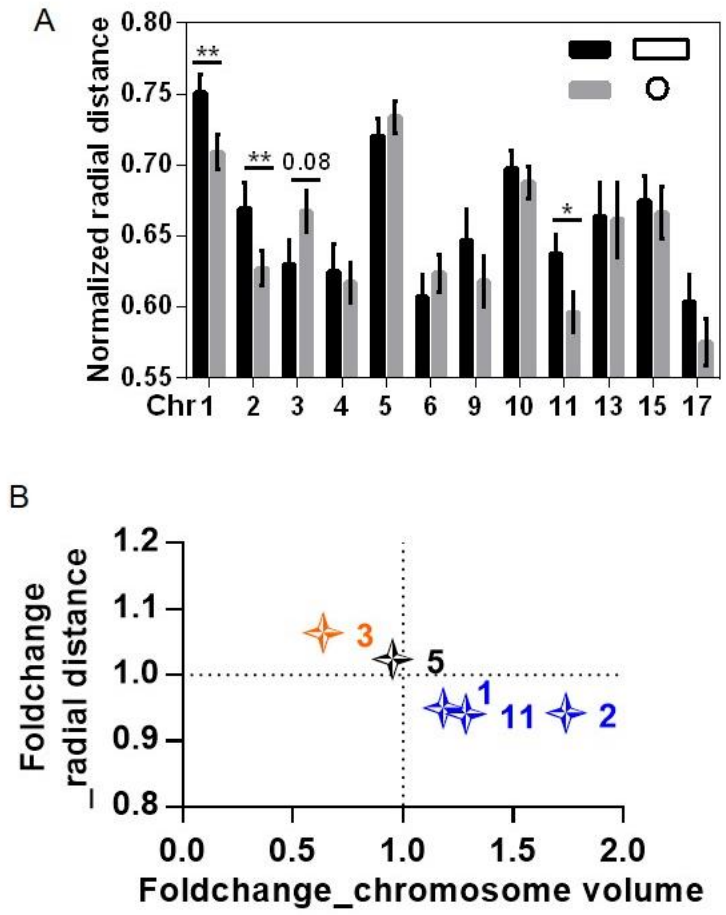

Figure 3.5 Cell geometry influences the normalized radial distance of chromosomes.

(A) Bar graph showing the radial distance of the painted CTs. Data is presented as mean ± SE with 50 < n < 80. ** $P < 0.01$, * $P < 0.05$. Mann-Whitney U test. (B) Scatter plot showing the foldchange

of radial distance and chromosome volume of Chr1, 2, 11 (blue), Chr3 (orange), and Chr5 (black) in IP cells compared to AP cells.

3.2 Changes in radial position were accompanied by differential levels of 5S RNA pol2.

Biochemical analyses and super-resolution imaging have shown that transcriptionally active chromatin is less compacted. To more precisely assess the level of chromatin compaction, we measured the chromosome decompaction factor, defined as the normalized volume of 1 mega base pair (Mbp) of DNA sequence (Figure 2.1B, see Materials and Methods). A larger decompaction factor indicates less compaction. As expected, the chromosome decompaction factor was found to be negatively correlated with radial distance (Figure 3.6).

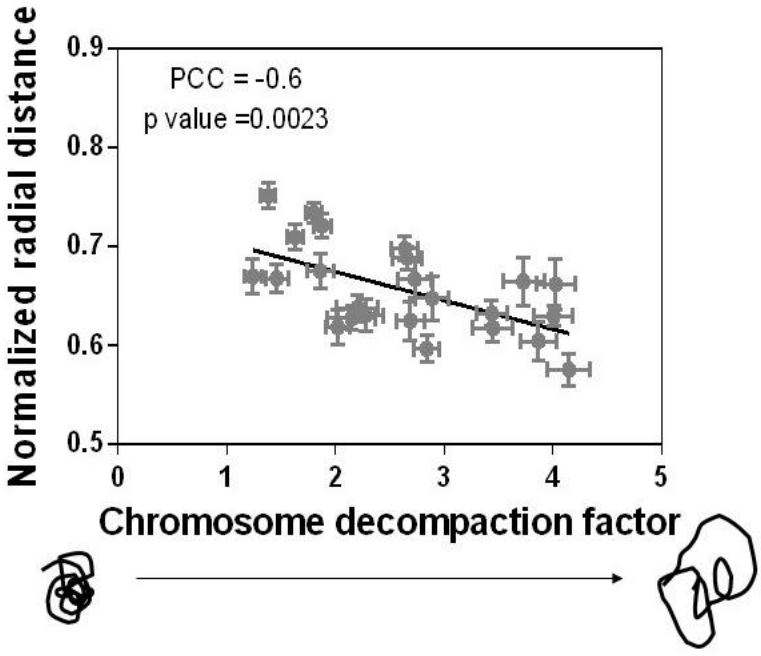

Figure 3.6 Correlation between chromosome radial distance and deccompaction.

Scatter plot between radial distance and decompaction pooled from CTs. Data is presented as mean ± SE with $50 < n < 80$.

To investigate the coupling between decompaction and transcription activity, we carried out immunofluorescence analysis of an active transcription marker, 5S RNA pol2, together

with chromosome FISH for Chr 1, 2, 3, and 11. The level of 5S RNA pol2 on each CT was found to be positively correlated with decompaction factor (Figure 3.7A), suggesting that less compacted chromosomes tend to be more transcriptionally active. These results lead to the correlation that interior chromosomes tend to have higher level of 5S RNA pol2 (Figure 3.7B). Indeed, Chr 1, 2, 3 and 11 that showed an altered radial distance exhibited the corresponding transcription activity changes (Figure 3.7C-E).

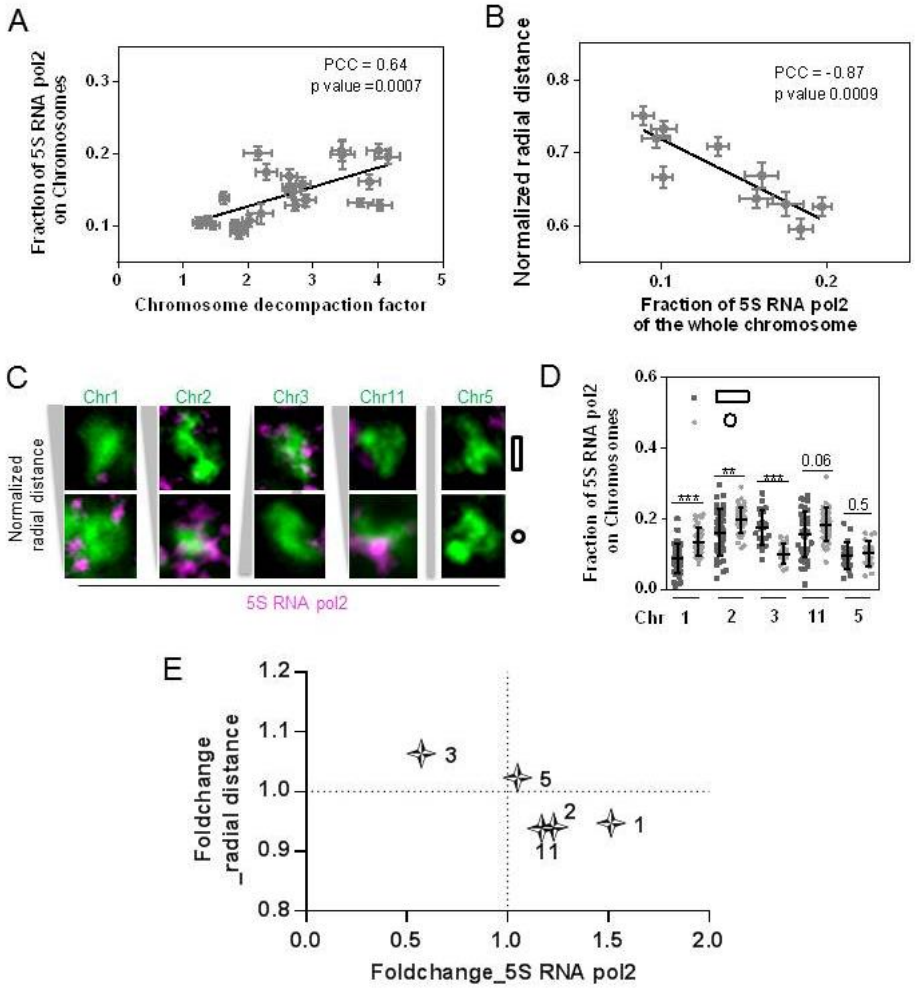

Figure 3.7 Changes in radial position are accompanied by differential levels of 5S RNA pol2.

(A) Scatter plot between the fraction of 5S RNA pol2 and decompaction of CTs. Data is presented as mean ± SE with 50 < n < 80. (B) Scatter plot between radial distance and the level of 5S RNA pol2, pooled from CTs. Data is presented as mean ± SE with 50 < n < 80. (C) Representative images showing the level of 5S RNA pol2 at the surface of Chr1, 2, 3, 11, and 5. (D) Dot plot quantifying the level of 5S RNA pol2 on Chr1, 2, 3, 11, and 5. Data is presented as mean ± SD with 20 < n < 30. $^{**}P < 0.01$. Mann-Whitney U test. (E) Scatter plot between foldchange of radial position and foldchange of 5S RNA pol2 level of chromosomes from AP substrates to IP substrates.

Remarkably, a careful analysis of 5S RNA pol2 levels together with chromosome staining revealed clusters of 5S RNA pol2 located at the surface of CTs (Figure3.8). While recent studies have highlighted the importance of "chromosome kissing" for gene co-regulation [41, 65-67], our results suggest that active 5S RNA pol2 at the surface of chromosomes might facilitate the interaction between heterologous chromosomes.

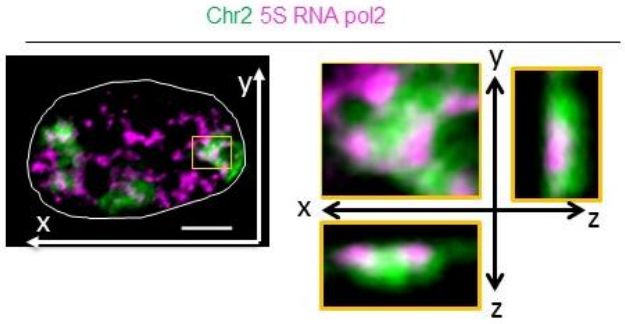

Figure 3.8 Activated form of RNA pol2 was revealed as pocket like structures at the surface of CTs.

Chromosome paint combined with immunofluorescent images of Chr2 (green), and 5S RNA pol2 (pink) with the nuclear outline (white) in xy plane. Scale bar: 5 μm. The right images are the orthogonal views of the region outlined by the orange box.

3.3 Cell geometry regulates the intermingling degrees between specific chromosomes.

Before interrogating the role of 5S RNA pol2 in "chromosome kissing", we analyzed the intermingling degrees between 10 pairs of chromosomes that were selected based on previous microarray data for these two cell geometries [9] (Figure3.9A). In these images we quantified the intermingling degree between pairs of CTs by the intermingling volume normalized by the CT volume as explained in Figure2.1C and Materials and Methods. Due to spatial limit in the interior part of ellipsoidal or spherical nucleus, chromosomes that are positioned inside tend to intermingle more, which was indeed shown from the negative correlation between the averaged radial distance of the 10 chromosome pairs and their intermingling degrees (Figure3.9 B, C).

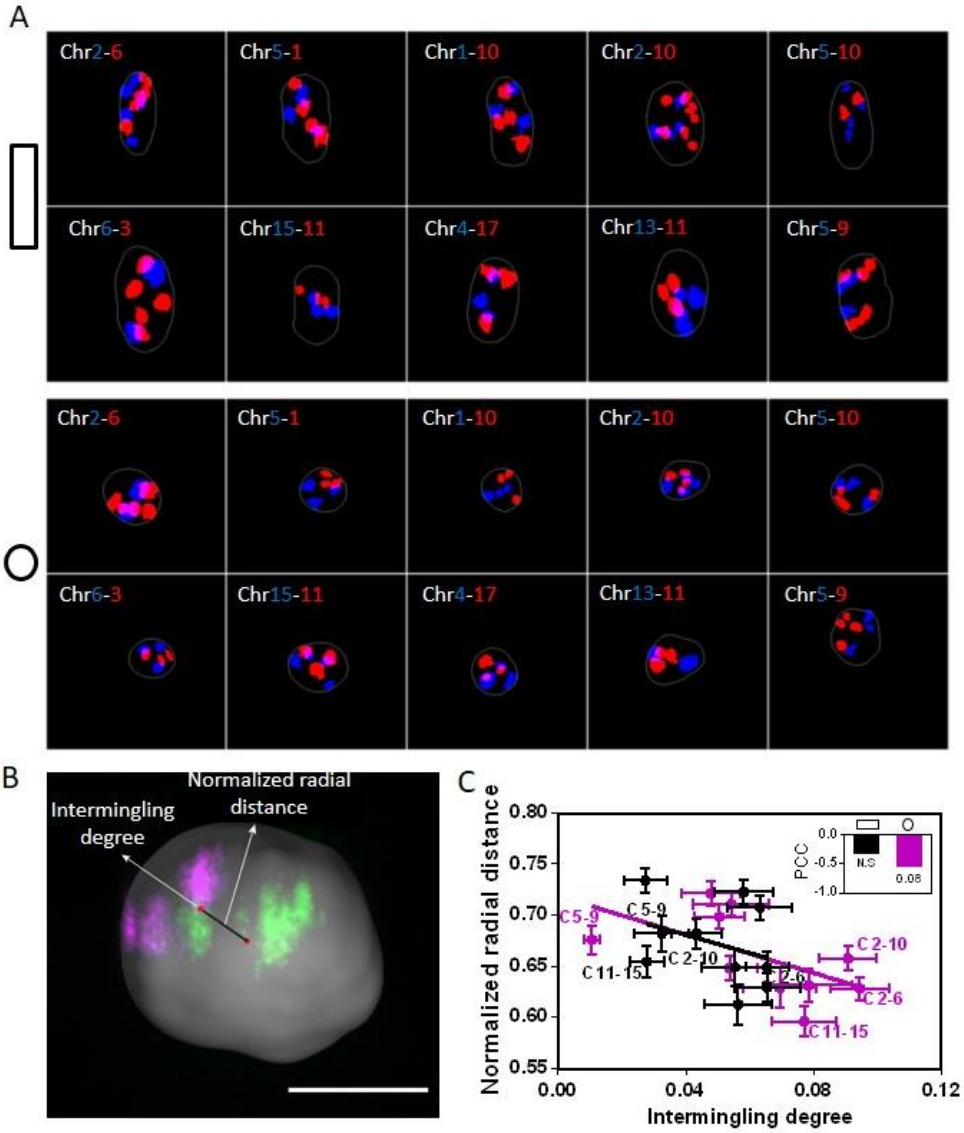

Figure 3.9 Intermingling between chromosomes is negatively correlated with radial distance.

(A) Thresholded images of all the CT pairs painted in this study in AP and IP substrates. (B) Imaris generated surface plot for confocal images of nucleus, with 3D representative Chr2 (green) and Chr6 (purple). Scale bar: 5 μm. (C) Scatter plot between averaged radial distance and intermingling degree of CT pairs. Data is presented as mean ± SE with 20 < n < 30. Inset: bar graph quantifying the Pearson Correlation Coefficient (PCC) between averaged radial distance and intermingling degree. P = 0.08, N.S denotes not significant.

To test the role of cell matrix reduction on chromosome intermingling we compared intermingling degrees of the 10 CT pairs between AP and IP substrates. Figure3.10A shows a global intermingling difference in response to matrix reduction. In particular, the pairs Chr2-Chr6, Chr2-Chr10, and Chr11-Chr15 show a significantly increased intermingling

degree, while the pair Chr5-Chr9 shows a significantly decreased intermingling degree in IP substrates, compared to those in AP substrates, and other chromosomes kept similar intermingling degrees (Figure3.10B, C). These results show that cell geometry affects intermingling degrees between specific chromosomes. Next, we investigated how cell geometry determines the specificity in the chromosome repositioning.

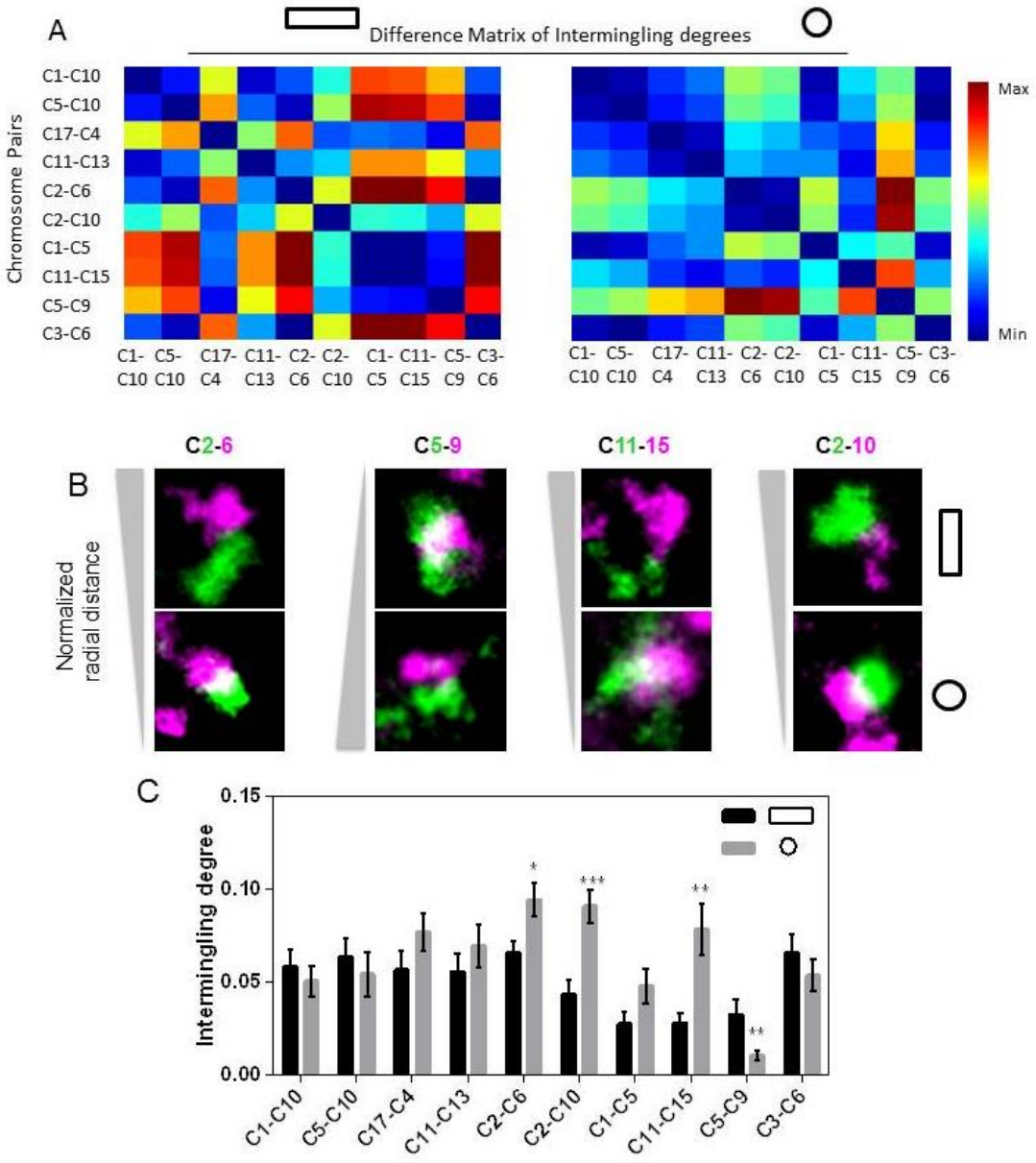

Figure 3.10 Cell geometry regulates the intermingling degrees between specific chromosomes.

(A) Intermingling difference matrix shows the difference of the intermingling degree between two CT pairs in AP and IP substrates. Row and column labels are the CT pairs painted in this study. (B) Representative images showing the intermingling degree of CT pairs (C2-6, C5-9, 11-15, and 2-10) with averaged radial distance. (C) Bar graph quantifying the intermingling degree of all the

CT pairs in AP and IP substrates. Data is presented as mean ± SE with 20 < n < 30. *** $P < 0.001$, ** $P < 0.01$, * $P < 0.05$. Mann-Whitney U test.

3.4 Chromosome orientation correlates with the specificity in intermingling changes.

First, we analyzed the effect of nuclear sphericity on CT orientation by measuring the angles between the long axis of each CT and the elongated mechanical axis of the nucleus as explained in Figure2.1D and Materials and Methods. Chromosomes with smaller γ_x or γ_z are closer to the X or Z axis. Interestingly, we found that in flattened and elongated AP nuclei the CTs preferably oriented along the major X-axis of the nucleus (Figure3.11C), while in spherical IP nuclei the CTs preferably oriented along the Z-axis of the nucleus (Figure3.11D).

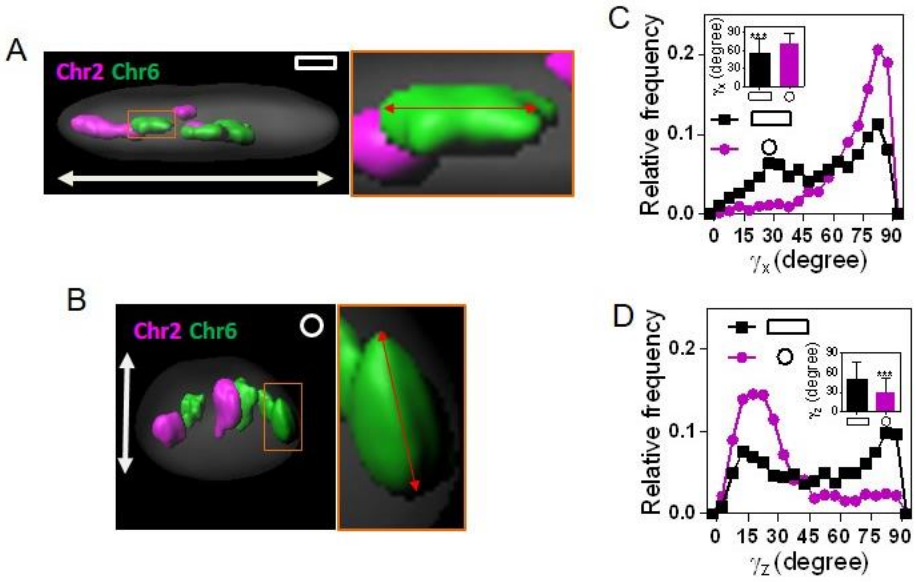

Figure 3.11 Cell geometry reorients chromosomes.

(A) (B) Imaris generated 3D surface plot of nucleus and chromosomes in AP and IP substrates. White double-arrow lines indicate the mechanical axis of nucleus. (C) (D) Angular distribution of γ_x and γ_z for all the painted chromosomes.

While mapping of CTs revealed different trends in CT orientations in the two geometries, analysis of individual CTs showed preferential orientations for different CTs in a given geometry (Figure3.12A, B). Next, we tested the relationship between chromosome orientation and intermingling. In AP substrates, there was a negative correlation between the γ_x and intermingling degrees (Figure3.12C), suggesting that chromosomes that were preferentially oriented along the X axis (defined as mechanical axis) of the nucleus intermingled more. To confirm this, we interrogated the relationship between chromosome orientation and intermingling in IP substrates, where a new mechanical axis (Z axis) was formed, and again a negative correlation was revealed (Figure3.12D). We then compared the effect of cell geometry changes on intermingling degrees with respect to CT orientation. Remarkably, we found that intermingling changes are related to CT orientation in the two cell geometries (Figure3.12E, F). More precisely, the CT pairs Chr2-Chr6, Chr2-Chr10 and Chr11-Chr15 that are most aligned along the Z-axis in IP substrates show the largest intermingling decrease in AP substrates (Figure3.12E). This suggests that chromosomes that align with the mechanical axis are sensitive to cell geometry change. This was confirmed by comparing intermingling change with respect to the angular CT orientations γ_x in AP substrates (Figure3.12F).

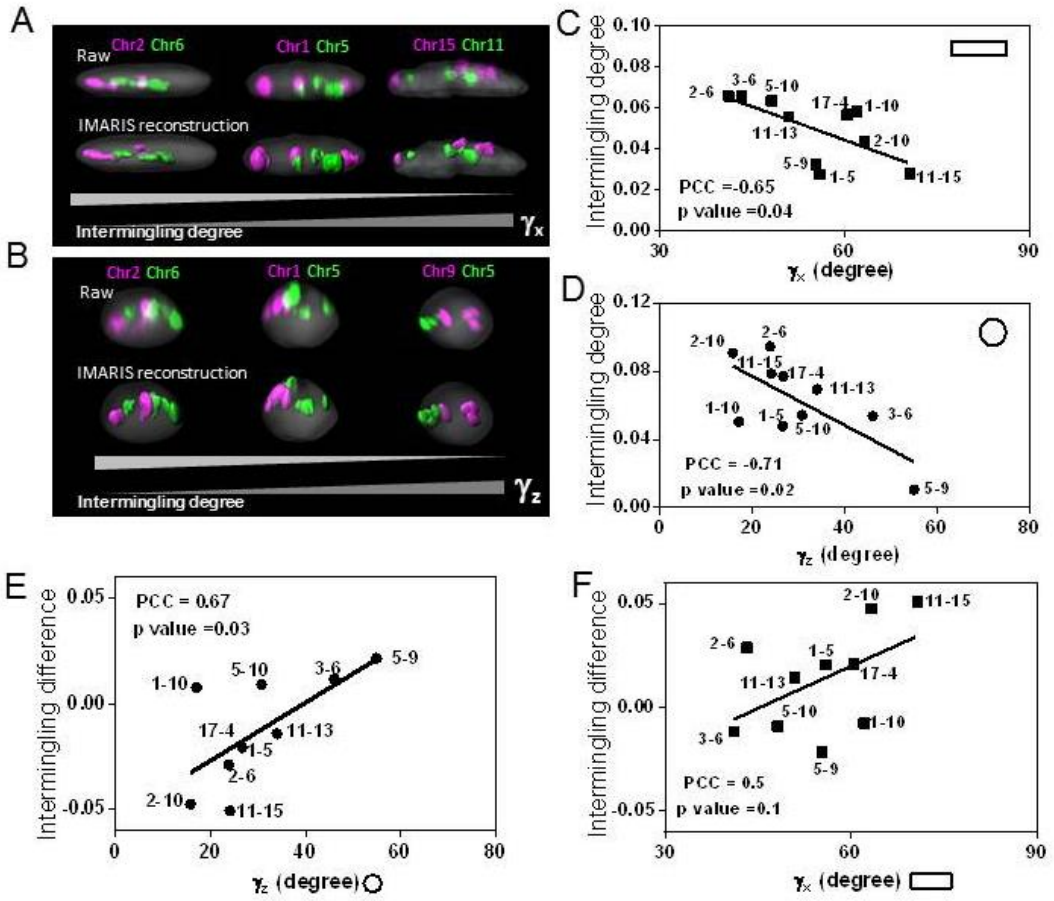

Figure 3.12 Chromosomes orienting along mechanical axis are sensitive to geometry changes.

(A)(B) Imaris generated 3D surface plot of nucleus and chromosomes. (C) Scatter plot between intermingling degree and γ_x in AP substrates. (D) Scatter plot between intermingling degree and γ_z in IP substrates. (E) Scatter plot between the intermingling change and γ_z in IP substrates. (F) Scatter plot between the intermingling change and γ_x in AP substrates.

3.5 Coupling between chromosome reorganization and transcriptome change.

To systematically probe the coupling between chromosome reorganization and transcriptome change upon cell geometry alteration, we performed microarray experiments (similar to the method described in [9]) by isolating RNA from NIH 3T3 cells cultured on anisotropic and isotropic substrates for 3 hrs. Raw microarray data was background corrected, normalized, and summarized using the Robust Multi-Array Average (RMA) method implemented in the *oligo* package in R. The chromosome information of each gene was obtained from the NCBI database (http://www.ncbi.nlm.nih.gov/gene/). Following this, we calculated the transcriptional activity of each chromosome. This was achieved by calculating z score of each gene across two conditions in triplicates and then sum the z scores of all the annotated genes located on one chromosome, defined as

$$Activity\ of\ chromosome\ (i) = \sum_{k} zscore(gene_k\ (\mathrm{i}))$$

Where $gene_k$ denotes the k^{th} gene on chromosome (i). The summarized z score of genes on each chromosome reflects the transcription activity level of this chromosome, and eliminates the bias from genes with high expression level. We plot an activity heatmap of 19 chromosomes in both geometries, where in each geometry the activity values of 19 chromosomes were centered to have mean 0 and scaled to have standard deviation 1 (Figure3.13A). By doing this we normalized the transcription activity of each chromosome to the activity level in one geometry, comparable to the normalization performed for radial distance. By comparing the changes in chromosome radial position and transcription activity, we found that chromosomes relatively more towards nuclear periphery in IP substrates compared to AP substrates had lower transcription activity in IP substrates, and *vice versa* (Figure3.13A, B). Such correlative changes were lost in randomized chromosome activity heatmap (Figure3.13C, D). This stands in the same line with aforementioned results revealing more compacted chromosomes, less 5S RNA pol2, and less intermingling for chromosomes moved towards nuclear periphery as cell geometry chnages.

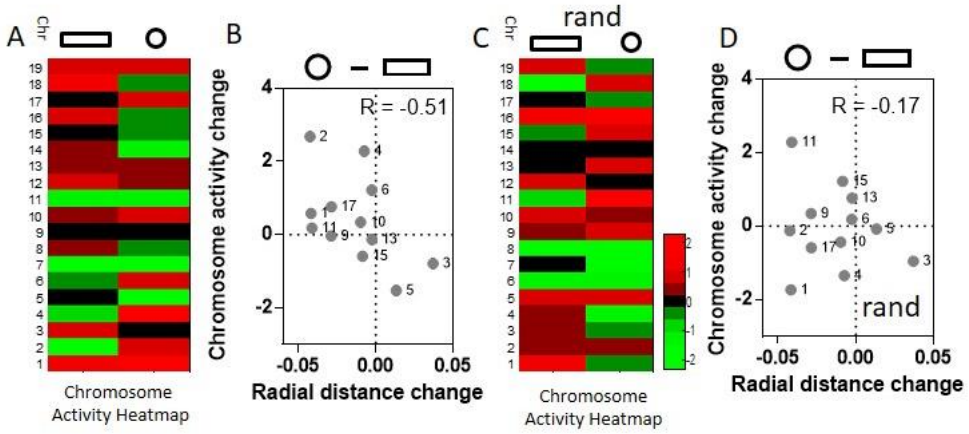

Figure 3.13 Coupling between the radial position change and chromosome activity change.

(A) Heatmap of chromosome activity in anisotropic (AP) and isotropic (IP) substrates. (B) Scatter plot of radial distance change and chromosome activity change between AP and IP substrates. (C)Randomized heatmap of chromosome activity. (D) Scatter plot of radial distance change randomized chromosome activity change.

To further investigate if the geometry-dependent intermingling change was also coupled with transcription activity change, we defined interchromosome activity distance as:

$$Interchromosome\ activity\ distance(i,j) = \frac{abs(Activity\ of\ chromosome\ (i) - Activity\ of\ chromosome\ (j))}{abs\big(Activity\ of\ chromosome\ (i)\big) + abs(Activity\ of\ chromosome\ (j))}$$

A smaller interchromosome activity distance reflects larger similarity of transcription activity between two chromosomes, implying more co-regulated genes [34]. The heatmap of interchromosome activity distance revealed global alterations in transcription configurations between AP and IP substrates (Figure3.14A). Interestingly changes of activity similarity, induced by cell geometry change, negatively correlates with changes of intermingling between two chromosomes (Figure3.14B). Such correlation was lost between randomized interchromsome activity distance and intermingling change (Figure3.14C, D). Particularly, chr5-9 that significantly decreased intermingling in IP substrates showed increased activity distance, whereas Chr2-6 and Chr2-10 that significantly increased intermingling in IP substrates showed decreased activity distance (Figure3.14A, B).

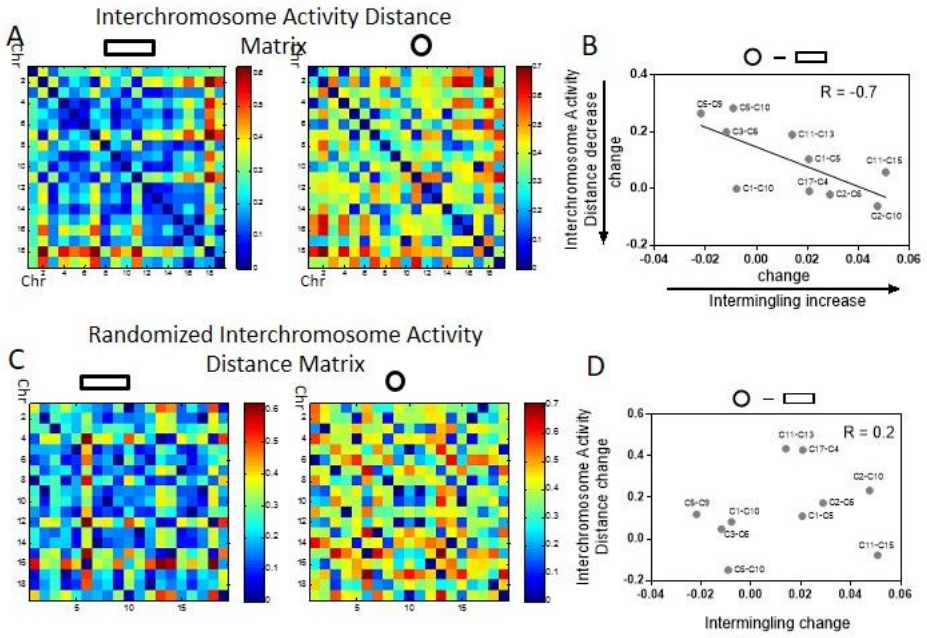

Figure 3.14 Coupling between the intermingling change and interchromosome activity distance change.

(A) Heatmap of interchromosome activity distance in anisotropic (AP) and isotropic (IP) substrates. (B) Scatter plot between intermingling change and interchromosome activity distance change between AP and IP substrates. (C)Randomized heatmap of interchromosome activity distance. (D) Scatter plot between intermingling change and randomized interchromosome activity distance change.

In addition, microarray data also uncovered that compared to polarized cells in AP substrates, rounded cells in IP substrates exhibited higher expression of NF-κB regulated

genes and lower expression of SRF/MRTF-A regulated genes (Figure3.15A, C). Particularly, on Chr2-6, NF-κB target genes such as Il1a, Tgm2, Olr1, Mmp9 etc. were upregulated. On Chr2-10, Tnfaip3, Il1a, Tgm2, Mmp9, Bcl2l1, Ptgds etc. were upregulated. On Chr11-15, Myc, Pdgfb, Stat5a, Ccl4, Rel, Csf3 etc. were upregulated, On Chr5-9, SRF/MRTF-A target genes such as Serpine1, Tagln, Steap1, Bmp2k etc. were downregulated compared to AP substrates (Figure3.15 B, D).

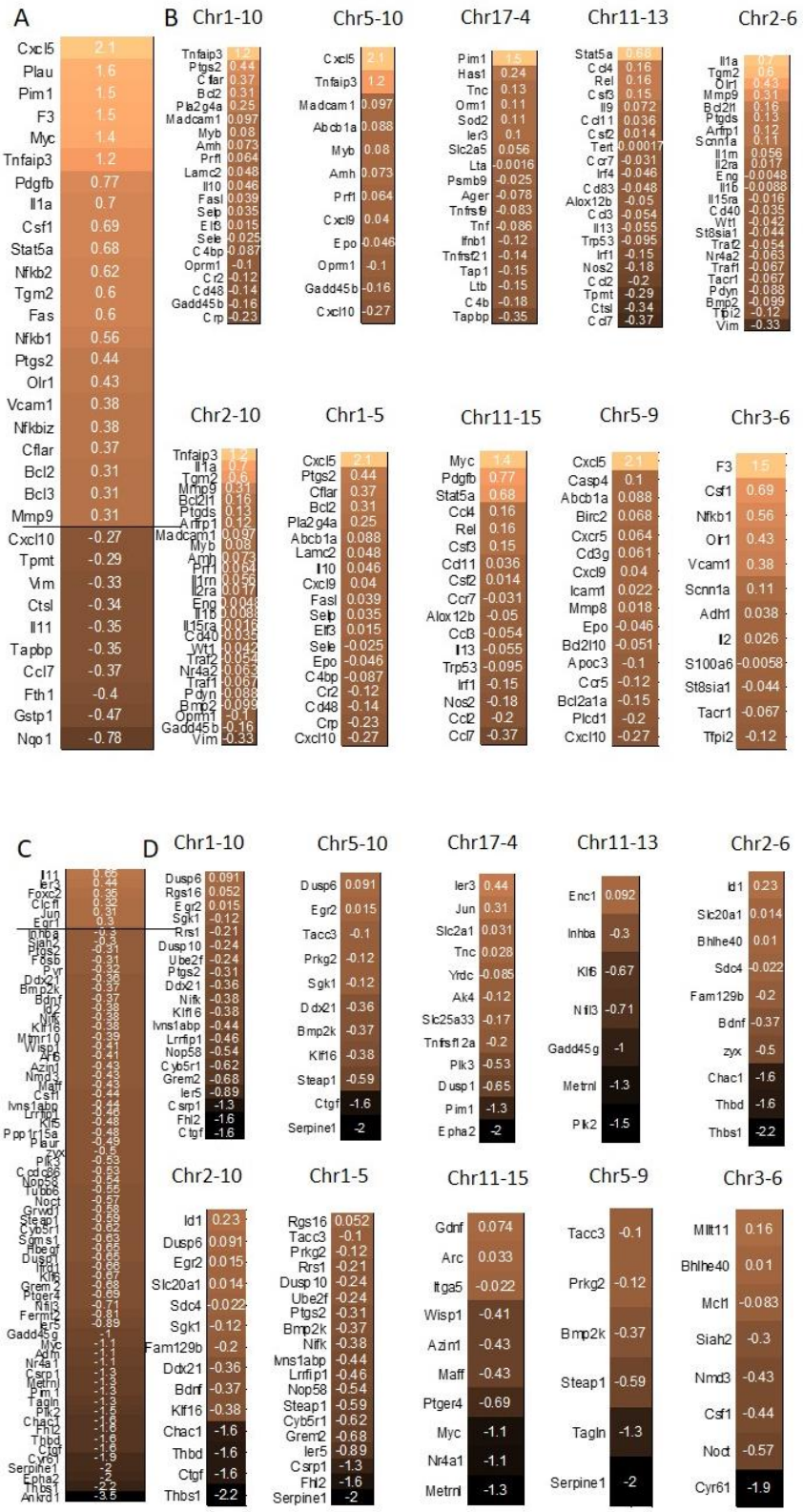

Figure 3.15 NF-κB target genes and SRF/ MRTF-A target genes.

(A) (C) NF-κB target genes and SRF/ MRTF-A target genes across the genome above the foldchange of 1.2 between AP and IP substrates. Values are log2 foldchange of expression of genes in IP substrates divided by that in AP substrates. Positive values (light color) indicate upregulation in IP

substrates and negative values (dark color) indicate downregulation, compared to AP substrates. (B) (D) NF-κB target genes and SRF/ MRTF-A target genes on the painted chromosome pairs.

3.6 The presence of 5S RNA pol2, SRF and its target gene *zyxin* in the intermingling regions is regulated by cell geometry.

Consistent with the observation that 5S RNA pol2 preferentially located at the surface of chromosome territories (Figure 3.8), here we further showed that 5S RNA pol2 enriched in the chromosome intermingling regions (Figure3.16A, B). The level of 5S RNA pol2 increased when intermingling degree was increased by changing cell geometries (Figure3.16C, D).

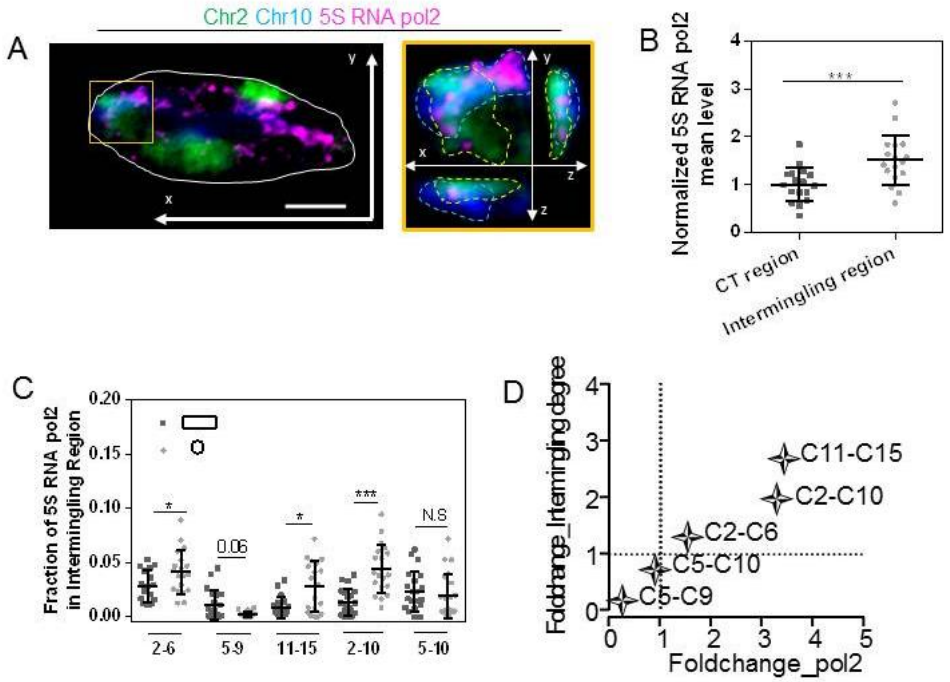

Figure 3.16 5S RNA pol2 enriched in the intermingling regions, the level of which decreases when chromosomes intermingle less.

(A) Chromosome paint combined with immunofluorescent staining of Chr2 (green), Chr10 (blue), and 5S RNA pol2 (pink) with the nuclear outline (white) in xy plane. Scale bar: 5 μm. The right image is the orthogonal view of the outlined region outlined by the orange box. Dotted outlines depicted the edge of each chromosome. (B) Dot plot showing the mean intensity of 5S RNA pol2 in CT regions and intermingling regions. Data is presented as mean ± SD with $15 < n < 20$. *** $P < 0.001$. Two sample student's t test. (C) Dot plot showing the different fraction of 5S RNA pol2 in the intermingling regions between C2-6, 5-9, 11-15, 2-10, and 5-10. Data is presented as mean ± SD with $20 < n < 30$. *** $P<0.001$, * $P<0.05$; N.S denotes not significant. Mann-Whitney U test. (D) Scatter plot between the intermingling foldchange and the RNA pol2 foldchange.

To confirm that transcription is indeed involved in the intermingling increase, we treated cells with a transcription inhibitor α-amanitin, which degrades 5S RNA pol2 [68]. We first confirmed that treatment with 40 μg/ml α-amanitin for 30 min indeed decreased the level of 5S RNA (Figure 3.17).

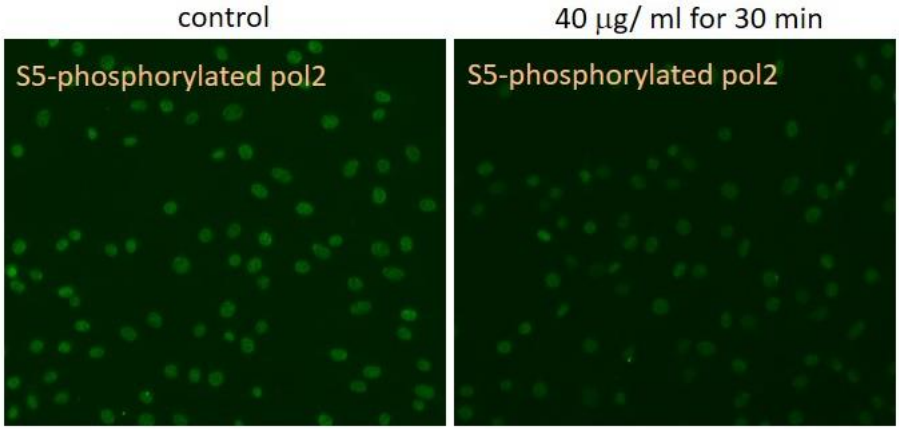

Figure 3.17 Treatment with 40 μg/ml α-amanitin for 30 min decreases the level of 5S RNA pol2.

We then labeled Chr11 and Chr15 in cells cultured on both AP and IP substrates with or without α-amanitin treatment. Consistent with a previous study showing that chromosomes with larger intermingling volume decrease their intermingling after transcription inhibition [36], we found Chr11 and Chr15 that had larger intermingling volume in IP substrates decreased intermingling after transcription inhibition, while in AP substrates where Chr11 and Chr15 had smaller intermingling volume didn't show significant difference after transcription inhibition (Figure3.18A, B). More importantly, we found that the significant intermingling increase was lost upon transcription inhibition even with the same cell geometry change, indicating that transcription activity is involved in the increase of chromosome intermingling while changing cell geometries. This could be because that the recruitment of transcription machinery such as RNA pol2 and specific transcription factors, which is required for transcription initiation and elongation, is also essential for the stabilization of chromosomal contacts or intermingling.

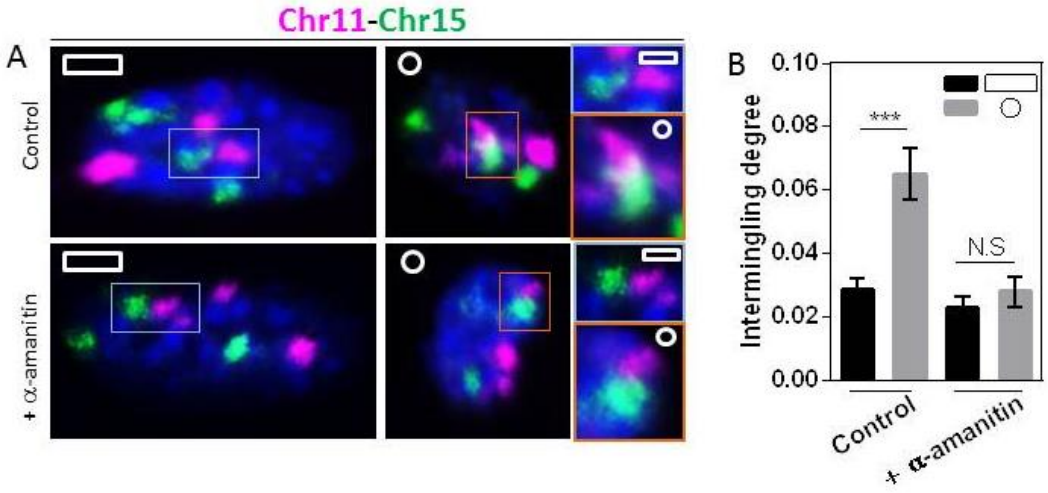

Figure 3.18 Transcription is required for the increase in intermingling degrees.

(A) Representative images of nucleus stained by Hoechst, Chr11 (purple), Chr15 (green) Right: zoomed in image of the outlined regions by light blue and orange boxes. (B) Bar graph showing the intermingling degree of Chr11 and Chr15. Data is presented as mean ± SE with 20<n<30. *** *P*<0.001. N.S denotes not significant. Mann-Whitney U test.

Next, we searched for specific transcription factors and their target genes in intermingling regions. We analyzed a specific chromosome pair as an example, namely Chr5-Chr9 that harbors serum response genes, which have lower activity and less intermingling in IP substrates (Figure 3.15D, Figure 3.10B, and C). First we checked the localization of serum response factor (SRF) that regulates these genes by immunostaining SRF together with Chr5 and Chr9. We found that about 60% of nuclei were enriched with SRF clusters in the intermingling regions in AP substrates while only about 20% were enriched in IP substrates (Figure3.19A, B). Moreover, we found a higher Pearson's correlation coefficient between SRF and 5S RNA pol2 signals in intermingling regions compared to the whole nucleus (Figure3.19C-E). Furthermore, one of the SRF target genes *Zyxin* was found to localize in the intermingling regions (Figure3.19G), and its localization frequency correlated with the expression level of the gene (Figure3.19F-H). These results reveal that, in addition to the coupling between changes in chromosome intermingling and activity distance, specific transcription factor SRF colocalized with 5S RNA pol2, as well

as its target gene *Zyxin* are present in the intermingling regions, which is also regulated by cell geometries.

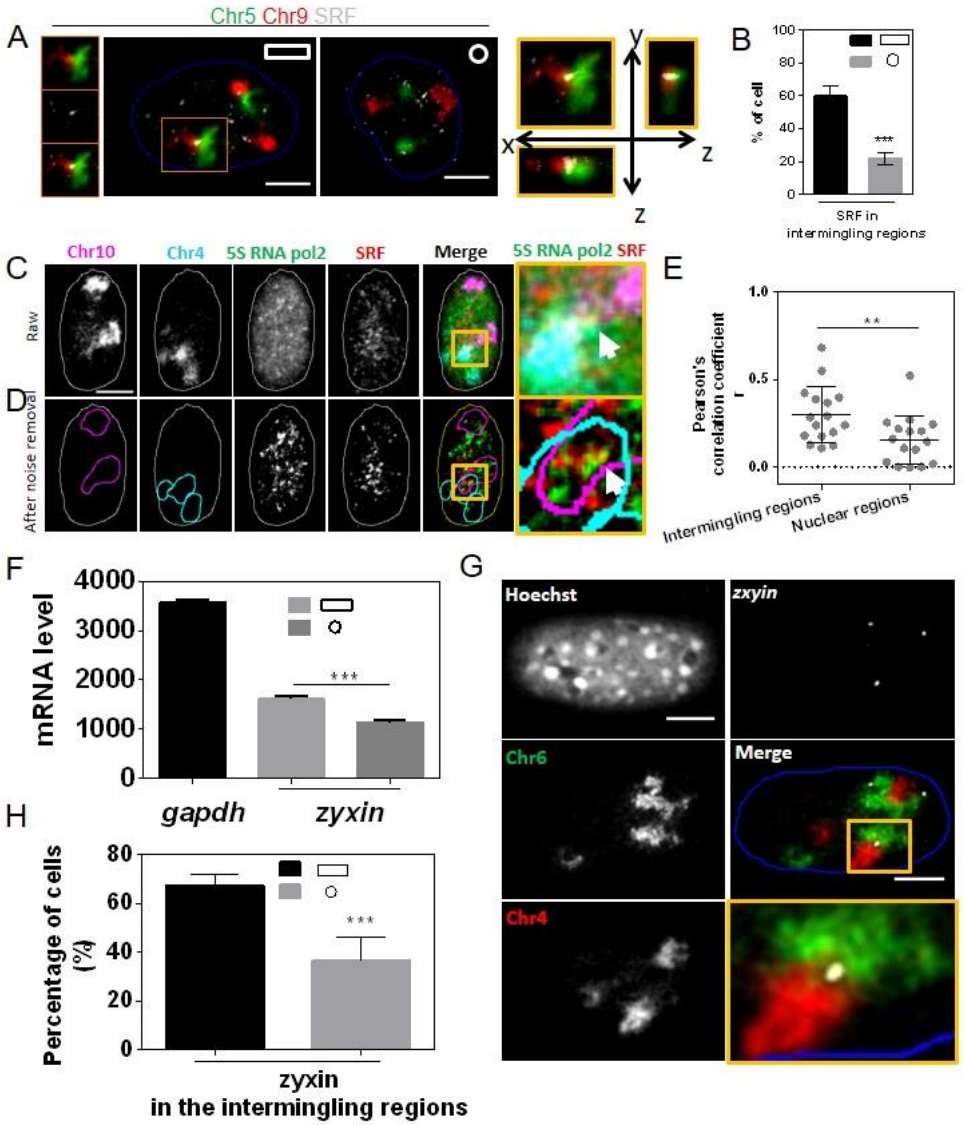

Figure 3.19 Localization frequency of SRF&5S RNA pol2 clusters and *zyxin* in intermingling regions is regulated by cell geometry.

(A) Chromosome paint combined with immunofluorescent staining of Chr5 (green), Chr9 (red), and serum response factor (SRF) (gray) with the nuclear outline (blue) in xy plane. Scale bar: 5 μm. The left images are Chr 5 (green), Chr9 (red), and SRF (gray) from the outlined region with an orange box. The right image is the orthogonal view of the outlined region outlined by the orange box. (B) Bar graph showing the percentage of cells with SRF signals presenting in the intermingling regions. Data is presented as mean ± SE with n = 3. *** $P < 0.001$. Two sample student's t test. (C) Representative raw images of Chr10 (purple), Chr4 (Cyan), 5S RNA pol2 (green), and SRF (red) at one focal plane. Scale bar: 5 mm. Inset: zoomed in image of the outlined regions by orange boxes. (D) Outlines for Chr10 (purple), Chr4 (Cyan), and processed images for RNAPII (green) and SRF (red), by applying a Fourier high pass filter to remove background noise and to highlight the bright features. Inset: zoomed in image of the outlined regions by orange boxes. White arrows indicate the colocalization between 5S RNA pol2 and SRF. (E) Dot plot showing the Pearson correlation

coefficient r between 5S RNA pol2 and SRF within intermingling and whole nuclear regions. Data is presented as mean ± SD with n=16. ** $P<0.01$. Two sample student's t test. (F) Bar graph showing the mRNA level of the gene *gapdh* and *zyxin*. Data is presented as mean ± SD with n=3. *** $P<0.001$. Two sample student's t test. (G) Representative images of nucleus stained by Hoechst, Chr6 (green), Chr4 (red), and *zyxin* (white) at one focal plane. Scale bar: 5 mm. Inset: zoomed in image of the outlined regions by orange boxes. (H) Bar graph showing the percentage of cells showing the localization of *zyxin* in the intermingling regions. Data is presented as mean ± SD with n=3. *** $P<0.001$. Two sample student's t test. Adapted with permission from Nucleic Acid Research.

Until now we have shown a strong correlation between cell geometry, chromosome reorganization and global changes in transcription. While chromosome intermingling is sensitive to transcription inhibition, we found that chromosome reorientation and changes in radial position were not affected by transcription inhibition (Figure3.20).

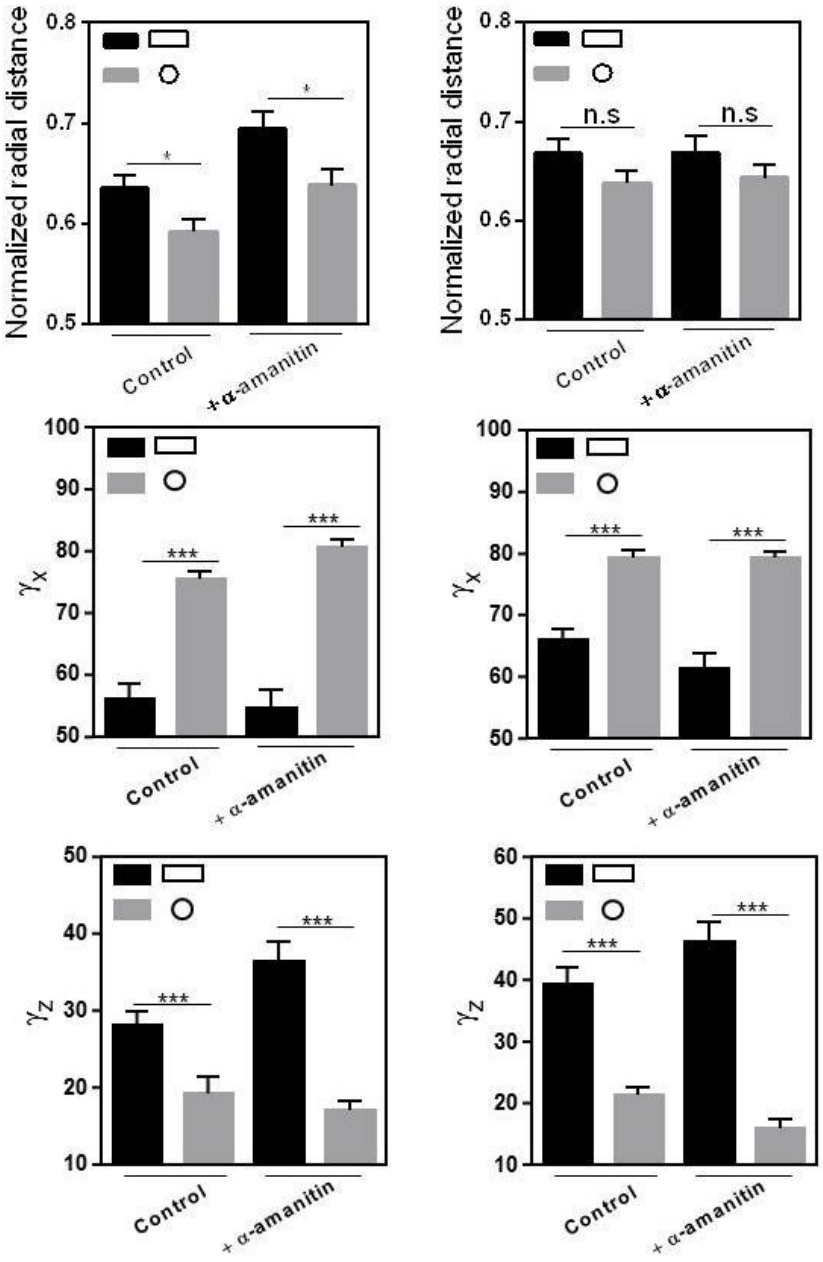

Figure 3.20 Chromosome reorientation and reposition is not due to global changes in transcription.

Bar graph showing changes in normalized radial distance, and 3D orientations of chromosomes by cell geometry with or without transcription inhibition.

3.7 Ellipsoid packing models predict cell geometry specific CT orientations and new neighbourhoods.

In order to quantitatively describe experimental realizations of chromosome arrangements and predict their rearrangements under nuclear shape alterations, we developed a geometric model of chromosome organization and gene expression. We model the spatial organization of chromosomes in the cell nucleus as a minimal overlap arrangement of ellipsoids of a given size and shape (the chromosomes) into an enclosing container (the cell nucleus) under spatial constraints given by the gene expression pattern. This allows us to predict the 3D organization of chromosomes when altering the cell geometry by solving a constrained optimization problem.

The constrained optimization problem takes as input a set of 60 ellipsoids, representing the triploid state of NIH3T3 cells, of diverse size and shape given by the chromosome shape measurements from FISH images and a larger enclosing ellipsoid given by the nucleus measurements in AP substrates. Given a configuration of ellipsoids we compute a vector consisting of all weighted (by expression similarity) pairwise overlaps of the 60 ellipsoids. We score the configuration by the maximum entry of this vector, i.e. the maximum weighted pairwise overlap between any two chromosomes. Starting in a random configuration of ellipsoids, our algorithm iteratively produces new ellipsoid configurations, whose scores are reduced at each step, and converges to a weighted minimal overlap configuration that represents the preferential chromosome neighborhoods (see MATERIAL AND METHODS). Such a weighted minimal overlap packing is shown in Figure3.21A. The algorithm then deforms the nucleus stepwise into the shape taken in IP substrates and computes the respective minimal overlap configurations (Figure3.21B).

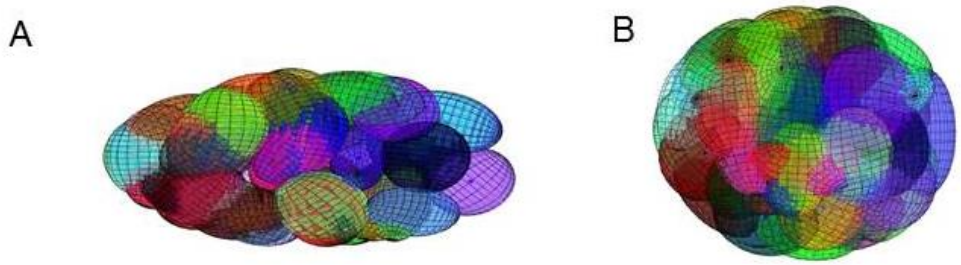

Figure 3.21 Ellipsoid packing models.

(A) and (B) show examples of optimal configurations of chromosomes modeled as ellipsoids packed into the ellipsoidal nucleus in AP and IP geometries, respectively.

Since the experiments established the importance of angular orientation of the chromosomes for intermingling and gene expression, we analyzed the angular distribution in the simulations. Figure3.22B, D shows the distribution in γ_x and γ_z obtained from the simulations. These distributions are qualitatively in agreement with the experimental trends (Figure3.22A, C), demonstrating that nucleus shape with activity-similarity based chromosome arrangement is able to predict the angular distributions of the chromosomes.

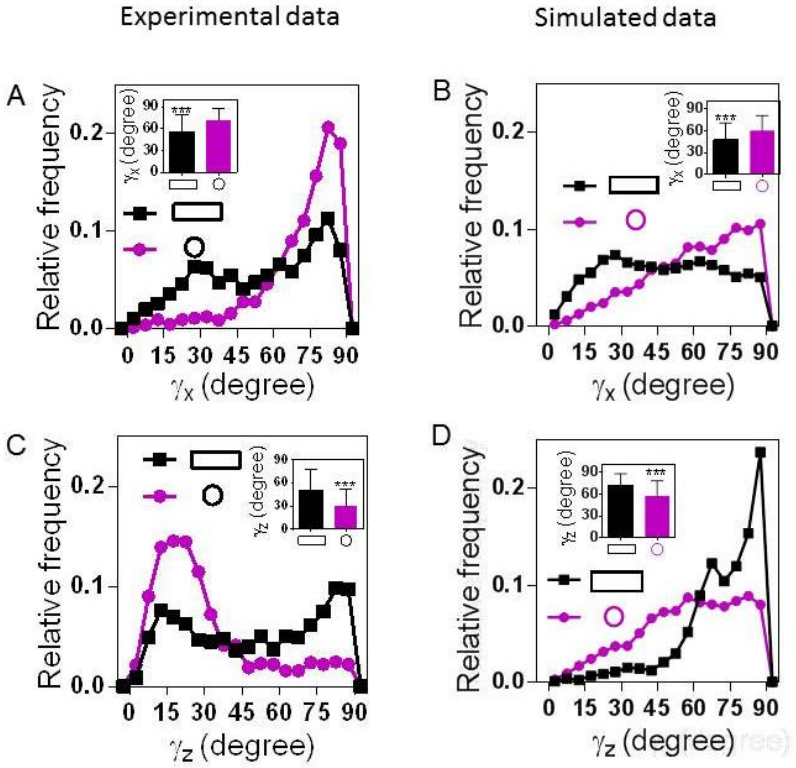

Figure 3.22 Ellipsoid packing models predict cell geometry specific chromosome orientations. (A) (B) Angular distribution of γ_x. (C) (D) Angular distribution of γ_z.

Next, we analyzed the radial distance in ellipsoidal and spherical nuclei. Compared to the experimental results (Figure3.23A), the average radial distance values show less variability overall (Figure3.23B). But interestingly, when altering cell shape from ellipsoidal to spherical cell nucleus, the radial distance values exhibit the same behavior as in the experiments (Figure3.23B, C). For example, Chr 1, 2, 11, and 17 are found more towards the center of the nucleus in spherical cell nuclei, i.e. IP substrates, compared to AP substrates, whereas Chr 3 exhibits the opposite behavior. In addition, in concordance with the experimental observations Chr 5, 6, 9, and 13 do not change radial distance when altering cell shape. Finally, the remaining Chr 4, 10, and 15 show the same trend as in experiments, but give more pronounced results in the simulations (Figure3.23B, C).

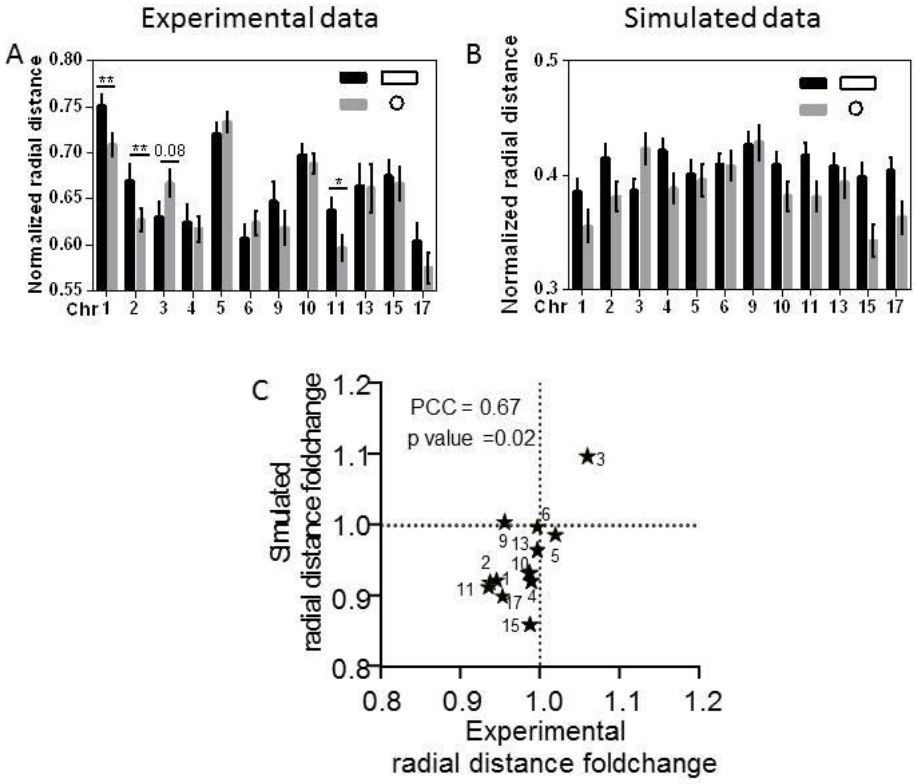

Figure 3.23 Ellipsoid packing models predict cell geometry specific chromosome radial positions.

(A)(B) Bar graphs showing the normalized radial distance of the painted chromosomes in experiment and simulation. (C) Scatter plot of averaged radial distance foldchange between IP and AP substrates.

To analyze the predictive power of this geometric model of chromosome organization, we further analyzed the changes in intermingling degrees when altering cell shape (Figure3.24). Here the simulations do not include any chromosome activity similarity weighting for the spherical cell nuclei. As a consequence, the intermingling degree values for different chromosome pairs in spherical nuclei are similar in size and cover only a small range. Remarkably, the geometric model is able to predict the new neighborhoods and interactions between chromosomes. In agreement with the experimental results, the pair Chr5-Chr9 shows minimal intermingling in ellipsoidal as well as in spherical cell nuclei, the pair Chr11-Chr15 shows a significantly increased overlap in spherical cell nuclei compared to ellipsoidal cell nuclei, the pair Chr2-Chr10 does not show overlap in ellipsoidal nuclei, but does overlap in spherical nuclei, and the pair Chr2-Chr6 shows a high intermingling degree in ellipsoidal as well as in spherical cell nuclei. These results show that for a nucleus with optimized chromosome arrangement, changes in nuclear shape could predict chromosome orientations, radial position and new neighborhoods.

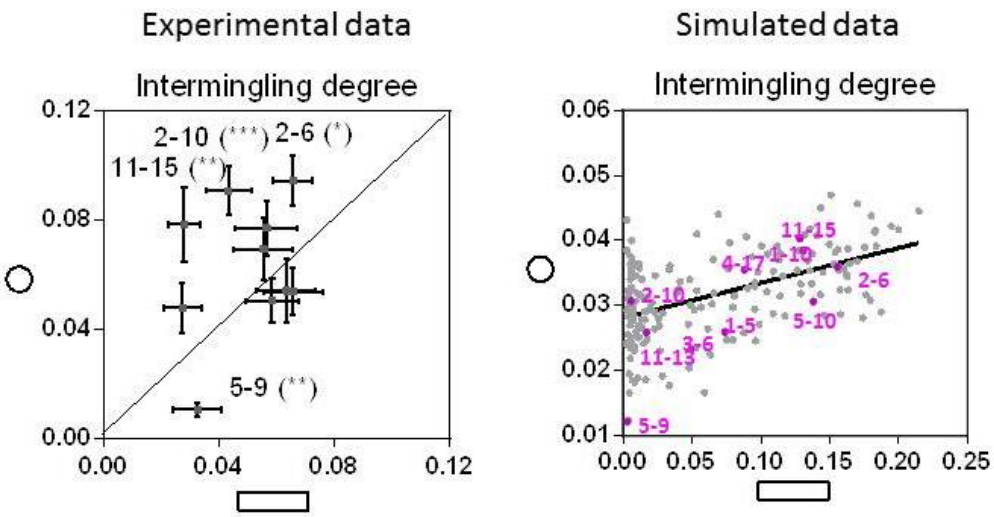

Figure 3.24 Ellipsoid packing models predict cell geometry specific new neighborhoods.

Scatter plot of intermingling degree between AP and IP geometries in experiments and simulations; the marked purple pairs represent the experimentally measured chromosome pairs.

Our results show that cell geometry induces cytoskeleton reorganization leading to nuclear morphology remodeling (Figure3.25A), which affects the orientation, 3D radial position, compaction, and intermingling of CTs in a non-random and predictable manner (Figure3.25B). These spatial rearrangements of the CTs were accompanied by alterations in their transcriptional activity. More precisely, intermingling increase is associated with recruitment of 5S RNA pol 2 (Figure3.25C), which is located in pockets within the intermingling regions, and such recruitment is necessary for intermingling. While it has been shown that chromosomal contact facilitates co-expression of a group of genes [41], our study highlights the importance of geometric constraints to regulate the rearrangements of CTs and formation of new chromosomal intermingling to modulate genomic programs. The next chapter describes a technique that directly visualizes chromosomal contacts using superresolution microscopy, and also interrogates the role of cell geometry on specific contacts formation.

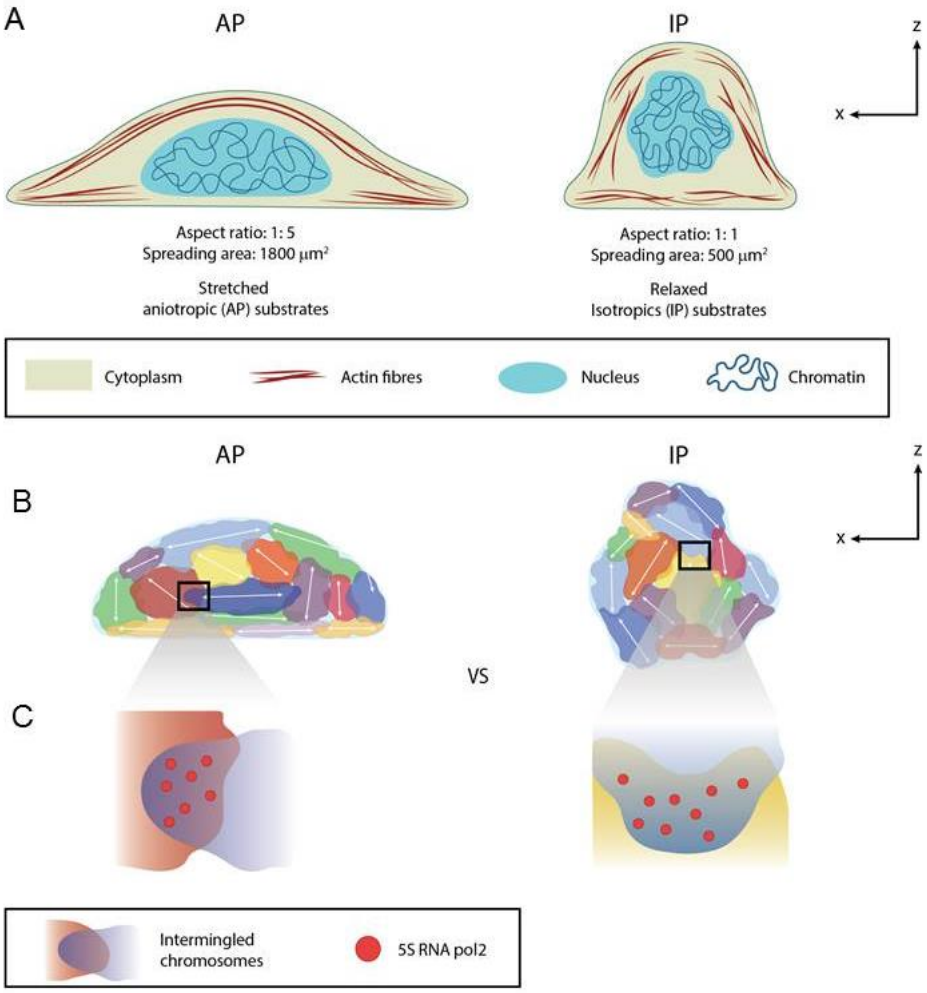

Figure 3.25 Model for the 3D chromosome reorganization in facilitating the geometry-dependent genome regulation.

(A) Cell geometry induced cytoskeleton reorganization, nuclear morphology remodeling, and alteration of global chromatin compaction. (B) The remodeling of nuclear morphology resulted in the reorientation of individual chromosomes and their radial positions. The orientation of chromosomes correlates with their sensitivity to cell geometry in creating specific new neighborhoods. (C) The new neighborhoods result in the formation of geometry-dependent new chromosomal contacts with the help of 5S RNA pol2 for differential gene expressions.

CHAPTER4 SUPERRESOLUTION MICROSCOPY REVEALS DECONDENSED CHROMATIN STRUCTURE AND CHROMOSOMAL CONTACTS AT ACTIVE TRANSCRIPTION SITES

4.1 Characterization of chromatin fibers

To surmount imaging difficulties arising from the crowded nuclear environment, we isolated nuclei from HeLa cells, seeded them on polylysine-coated glass microscopy slides and expanded the nuclei using deionized (DI) water for 10-30 minutes. Following this, we applied a mechanical force by moderate tapping through a coverslip on the expanded nuclei, thus highly organized chromatin within an intact nucleus was spread into strands, which were subsequently visualized by TIRFM (Figure4.1A, B). This sample preparation method produced long chromatin fibers on the coverslip with the preservation of large-scale chromatin structures. Histone protein H2B, and the highly dynamic H1 [69], co-localized with DNA in the chromatin spreads (Figure4.1B).

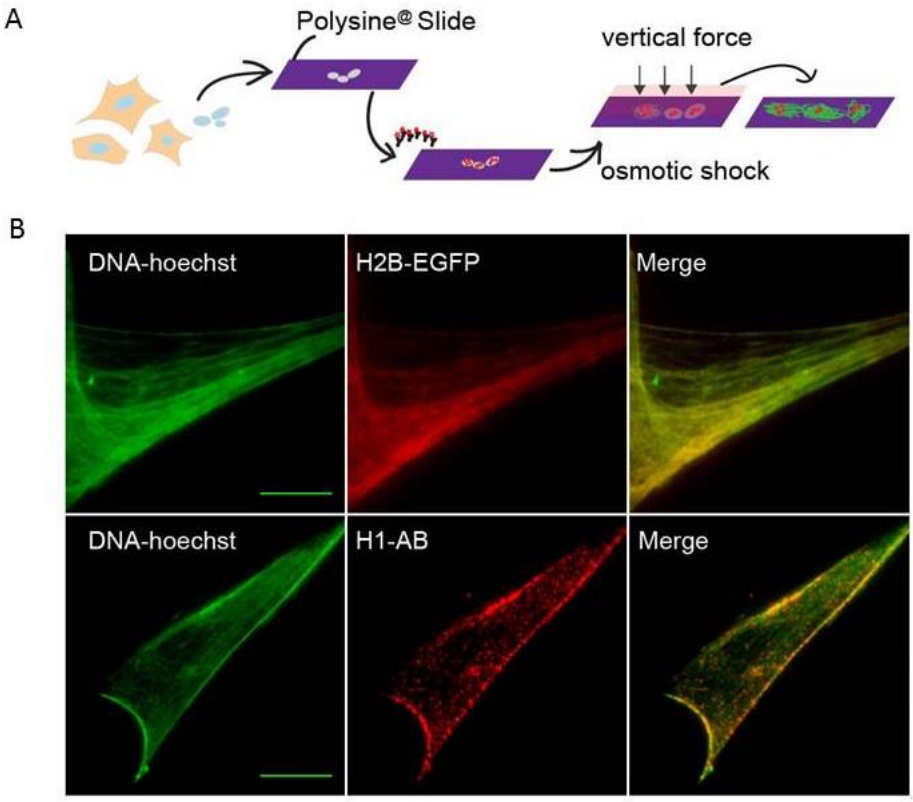

Figure 4.1 Functionality of chromatin fibers.

(A) Schematic of chromatin fiber preparation (B) Representative TIRFM images of the colocalization of DNA and histone proteins on chromatin fibers. Scale bar: 10 μm.

We quantified chromatin fiber width (CW) by measuring the full width at half maximum (FWHM) on the line intensity plot (averaging 10 pixels) across the fiber (Figure4.2A, inset) [63]. The final width of the chromatin was calculated by averaging measurements taken at multiple positions on multiple fibers. Four different labelling methods were used in the visualization and quantification of chromatin width. These were DNA labelled with Hoechst (DNA-Hoechst) (460±80 nm), DNA labelled with YOYO-1 (DNA-YOYO-1) (450±30 nm), H2B tagged with EGFP (H2B-EGFP) (400±50 nm), and H1 stained with antibodies (H1-AB) (500±80 nm). No significant difference in chromatin width existed when comparing the first three methods, however, compared to H2B-EGFP, H1 stained with antibodies (H1-AB) resulted in chromatin fibers that were 25% thicker (Figure4.2B). The extra width observed using H1-AB may be the consequence of two factors: firstly, H1 is the linker histone on the surface of the nucleosome, while H2B is a core histone located in the center of nucleosome. Secondly, H1 was labelled by primary and secondary antibodies (approximately 150kDa), whose size cannot be ignored, while H2B was tagged with a small GFP protein (approximately 27kDa). Also, compared to other fibers, the fibers labelled with H1-AB are more discontinuous, and this could be because of the highly dynamic nature of linker histone H1. Table4.1 describes the probe binding sites for the four labelling methods.

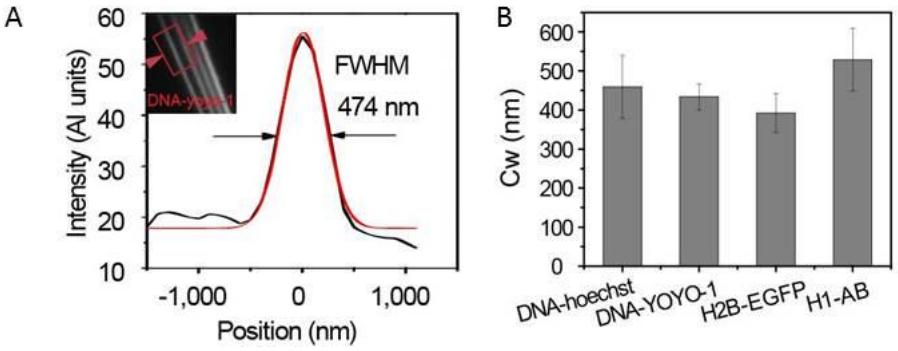

Figure 4.2 Measurement of fiber thickness.

(A) Line profile for determination of FWHM (representing chromatin width (Cw) in the inset red box) (B) Bar graph showing chromatin width (Cw) in four labeling ways: DNA stained with hoechst (DNA-hoechst), DNA stained with YOYO-1 (DNA-YOYO-1), H2B tagged with EGFP (H2B-

EGFP), and H1 immunolabeled with antibodies (H1-AB) (n≥20, all the 'n' in the following text refers to the number of fibers) (*P<0.05; Student's t-test).

Chromatin staining methods	Chromatin width (nm)	Probe binding site
DNA-Heochst	460±80	The minor groove of double-stranded DNA
DNA-YOYO-1	450±30	Intercalating in double-stranded DNA
H2B-EGFP	400±50	Tagged to core histone H2B
H1-AB	500±80	Immunostained to linker histone H1

Table4.1 Chromatin staining methods.

Various durations of incubation with DI water resulted in different degrees of nuclear expansion. A short incubation time (< 1 min) resulted in poor spreading whilst a long incubation time (> 1 hour) produced well-expanded spreads (Figure4.3A). Statistical analysis showed that after a longer incubation period (> 1 hour) there was no significant difference in the width of the spread fibers (Figure4.3B). However, the histone protein density, as well as RNA pol II density, decreased approximately 30% with the longer incubation (Figure4.3C). To obtain good spreading, and retain the maximum number of DNA binding proteins, the nuclei were expanded for 10-30 min. During this time the loss of linker histone H1 was less than 20%, and no significant loss of RNA pol II was observed when compared to a shorter expansion time (time < 1 min) (Figure4.3C).

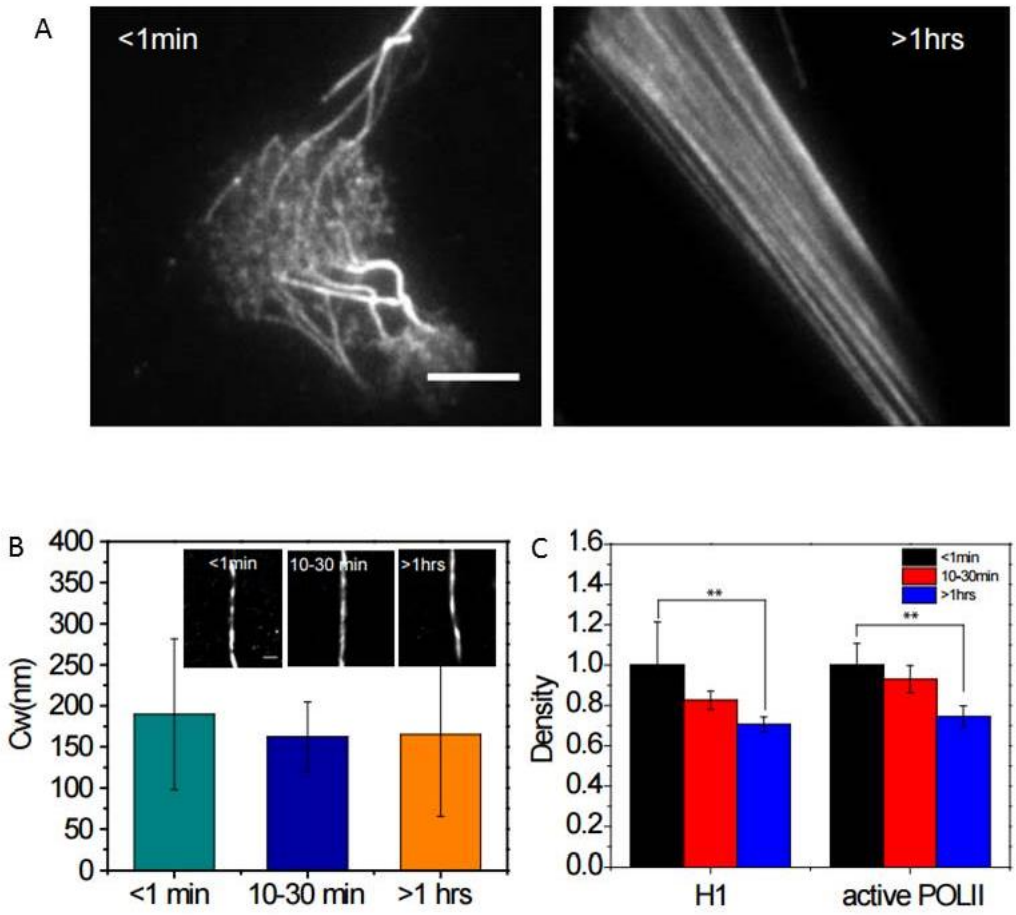

Figure 4.3 Effect of expansion time on the structure of chromatin fibers and the loss of histone proteins as well as transcription machinery.

(A) TIRF images of chromaitn spreads after expasion for 1 hrs. Scale bar: 5 µm. (B) Box graph shows the chromatin width after expansion for 1 hrs .Inset: representative BALM images of chromatin fibers in the three expansion time. Scale bar: 500 nm. (C) Bar graph shows the density of histone proteins and RAN pol II in the three expansion time (n≥20) (***P < 0.001; Student's t-test).

4.2 Enhancing the resolution of chromatin using BALM

We next exploited the binding activatable localization microscopy (BALM) to yield further insights into the organization of chromatin fibers. This super-resolution technique was developed by Schoen, I., *et al.*[63] in 2011. It resembles photoactivatable localization microscopy (PALM) [55] and stochastic optical reconstruction microscopy (STORM) [53], both of which are based on the detection of single-molecule, and provide single-molecule sensitivity with a spatial resolution of tens of nanometers. Cycles of stochastic switching,

detection, and localization of single molecules on a TIRFM microscope were used to reconstruct super-resolution images (*Materials and Methods*). YOYO-1, a DNA intercalating dye that fluoresces around 800-1000 times more upon binding to DNA, has been reported to be a good marker for STORM imaging of DNA in a reducing buffer[70]. However, due to photobleaching during the progressive imaging process employed by STORM, the labelling density of YOYO-1 was found to be too low, and yielded a lower density of localization events on the chromatin fibers, as well as a loss of detail for many structures (Figure4.4A). This problem was overcome by Schoen, I., *et al.*, and YOYO-1's labeling density improved, when its property of enhanced fluorescence following DNA binding was exploited by providing dynamic binding conditions. This gave rise to binding activatable localization microscopy (BALM) and using this imaging method, we were able to obtain more detailed images of chromatin fiber structures with thickness ranging from less 100 nm to ~500 nm (Figure4.4B, C).

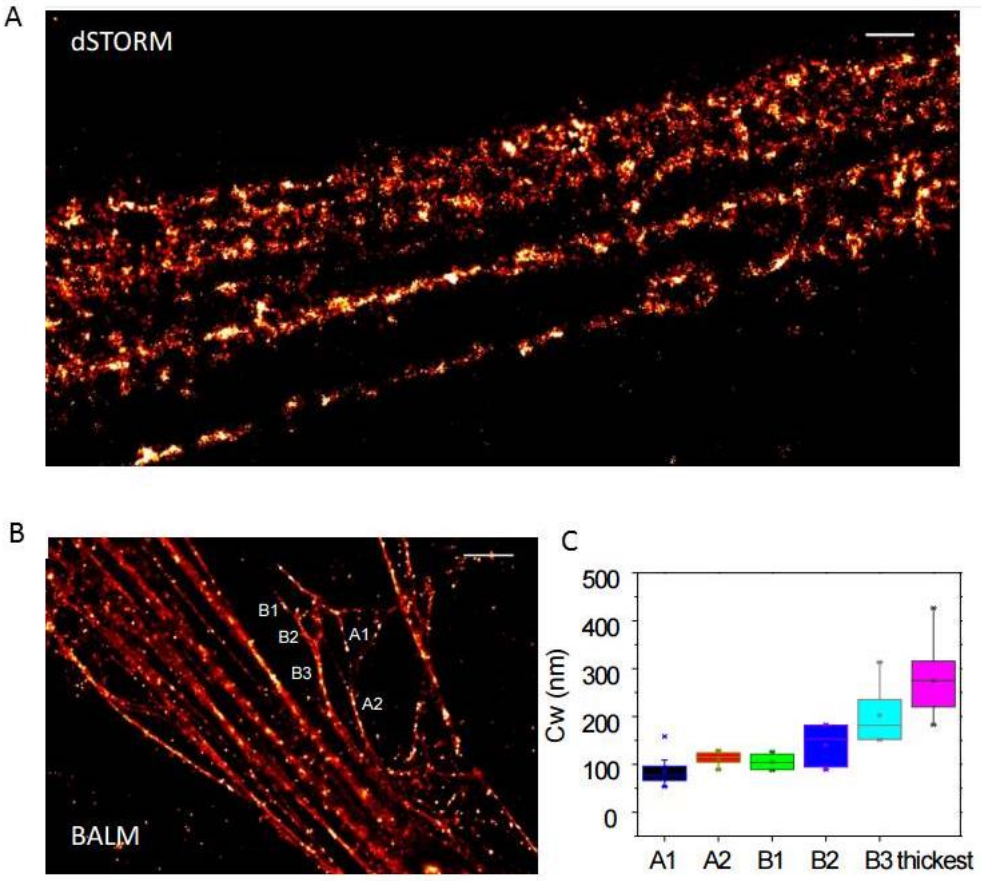

Figure 4.4 Chromatin fibers detected in PALM and BALM.

(A) Representative PALM image of chromaitn spreads. Scale bar: 2 μm. (B) Representative BALM image of chromatin spreads. Scale bar: 2 μm. (C) Box graph of chromaitn width (Cw) at different regions marked in (B).

To further optimize the labelling regime and the imaging conditions, we imaged the well-characterized λ DNA using BALM. However, the commercial λ DNA was coiled in solution (Figure 4.5A). We tried to find a simple way to stretch λ DNA onto glass slides. A droplet of λ DNA solution was added onto glass slides coated with positively charged (3-Aminopropyl) triethoxysilane (APTES). Combing of λ DNA was achieved either through dipping the slide into buffer and slowly lifting the slide, or via capillary effect induced by sucking solution with a piece of tissue paper, or through capillary effect combined with drying, or by spin-coating. The experimental conditions and outcomes of these four methods are summarized in Table 4.2. Figure. 4.5 and Table 4.2 show that capillary combing combined with drying results in the best and uniform stretching of λ DNA, and the procedure of this method is illustrated in Figure 4.6A.

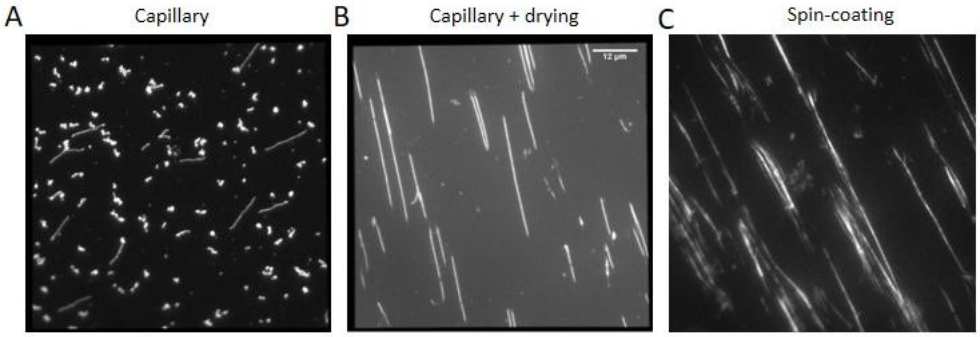

Figure 4.5 TIRFM images of λ DNA stretched using different methods.

Coverslip surface	buffer	pH	Combing method	result
APTES coated	PBS	6/7	dipping	✔
APTES coated	PBS	6/7	Spin-coating	✔✔✔
APTES coated	PBS	6/7	capillary	✔✔
APTES coated	PBS	6/7	Capillary + drying	✔✔✔✔
APTES coated	TRIS/H_2O	6/7	Capillary + drying	✗

Table 4.2 λ DNA combing methods.

We next labelled the stretched λ DNA fibres with YOYO-1 diluted in a reducing-oxidizing (ROXS) buffer (*Materials Methods*) and the stochastic subsets of blinking events were captured at a rate of 20 Hz. In solution, the YOYO-1 molecules remained dark until binding to DNA, at which point they became bright. This resulted in low background signals. Accumulated images of individual fluorophores localizing to the DNA allowed for the optical reconstruction of stretched double-stranded DNA (dsDNA) molecules (Figure4.6B) with a FWHM, which is a measure of the lambda DNA width (Lw), of 30±9 nm (mean ± SD) (Figure4.6C, D), much smaller than the thickness measured in the TIRFM images of λ DNA (Figure4.8B, inset i). The resolution was defined by the finest fiber width that could be detected in BALM, which was ~20 nm (Figure4.6B, C insets). Since ROXS enhanced both the binding and disassociation rates of YOYO-1 [63], DNA was continuously bound and unbound by dye molecules from the solution. As a result, the number of localization events remained high (Figure4.7) even in the later frames of acquisition. This ensured a decent reconstruction of the λDNA structure was obtained (Figure4.6B, inset). To get a well separated single molecule of λDNA on the coverslip, the λDNA stock was diluted to a concentration of 1 μg/ml, and most of the molecules that were selected for quantification possessed a length of ~20 μm, which is close to the predicted size of full-length λDNA.

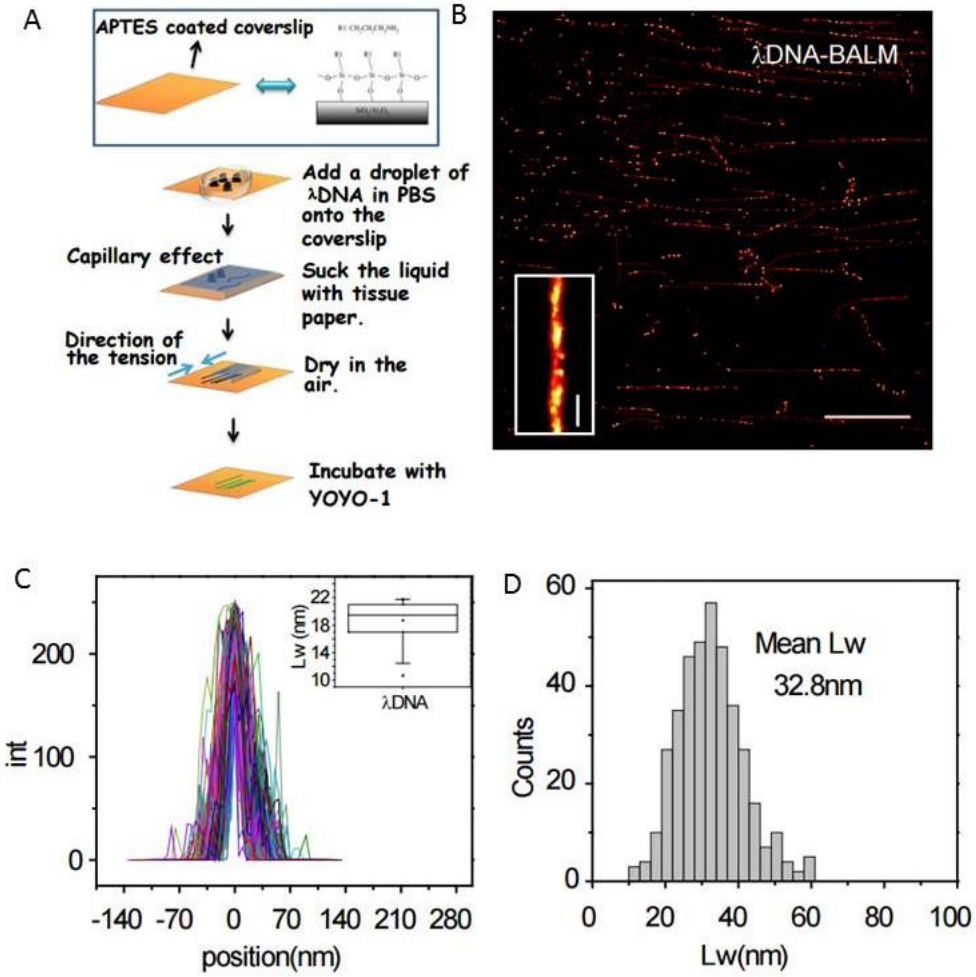

Figure 4.6 Characterization of λDNA in BALM.

(A) Schematic of λDNA combing (B)RepresentativeBALMimage of λDNA. Scale bar: 10 μm. Inset: zoomed in BALM image of λDNA. Scale bar: 50 nm. (C) Intensity line profiles at different regions of λDNA in BALM. Inset: as shown in inset of (B). (D) Histogram of lambda DNA width (Lw).

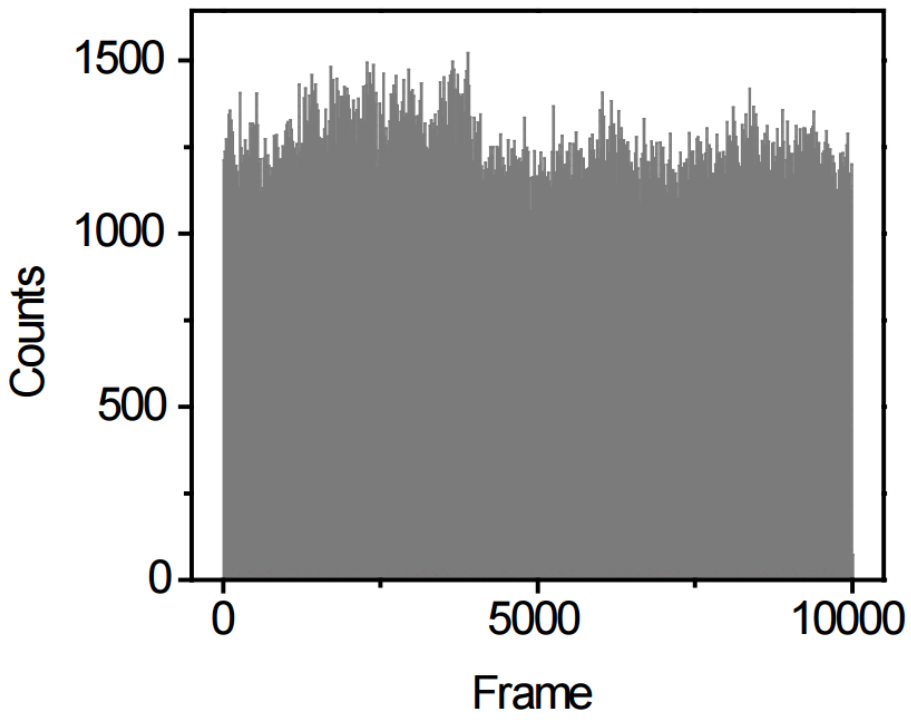

Figure 4.7 Number of localization events at each of the ten thousand frames.

After using well-studied λDNA as a control to characterize the super-resolution imaging technique, we applied similar imaging conditions to visualize chromatin spreads. The reconstructed image of chromatin fibers with a width of 150±45 nm (mean ± SD) showed dramatic enhancement in resolution when compared with diffraction-limited TIRFM image of chromatin fibers that have a width of 450±30 nm (mean ± SD) (Figure4.8A, B, inset i, ii).

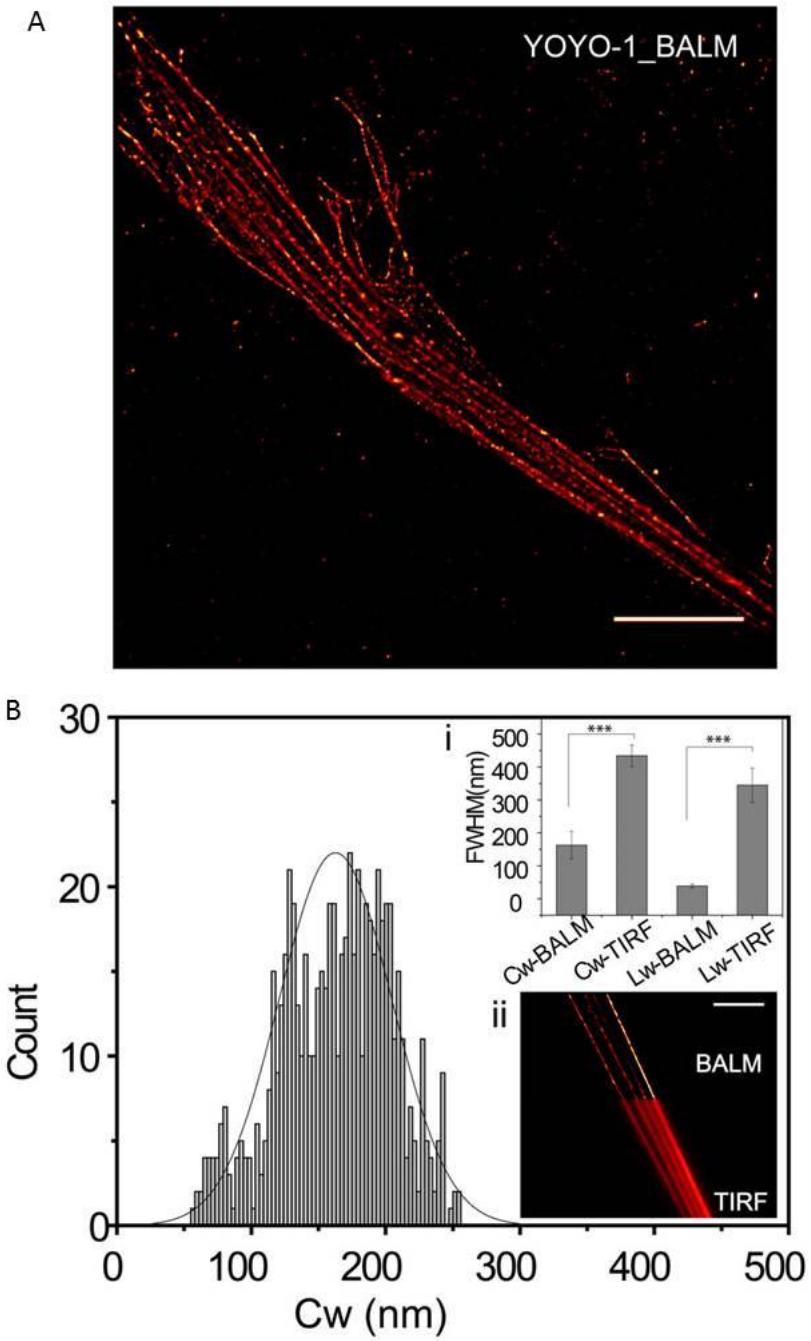

Figure 4.8 BALM images of chromatin fibers.

(A) A representative BALM image of chromatin fibers stained with YOYO-1. Scale bar: 10 μm. (B) Histogram showing the distribution of chromatin width (Cw). Inset i shows the chromatin width (Cw) and λDNA width (Lw) in BALM image and TIRF image ($n \geq 20$) (***$P < 0.001$; Student's t-test). Insect ii shows a combination of BALM and TIRF images of the same sample. Scale bar: 10 μm.

4.3 Serum starvation induced chromatin condensation

Next, we tested if BALM could detect structural changes in chromatin induced by transcriptional quiescence. Cells were switched to a quiescent state by withdrawing serum from their growth medium for 36 hrs [71-73]. Chromatin spreads were subsequently obtained from these cells. Under serum withdrawal (serum (-)) conditions, the width of the observed chromatin fibers was 80 ±40 nm (mean ± SD), which was substantially thinner than those observed under serum (+) conditions, which averaged 150 ±45 nm (mean ± SD) (Figure4.9). From the BALM images, serum (-) chromatin fibers had a higher photon density (Figure4.9 insets), which was caused by the higher DNA labeling density in serum (-) fibers.

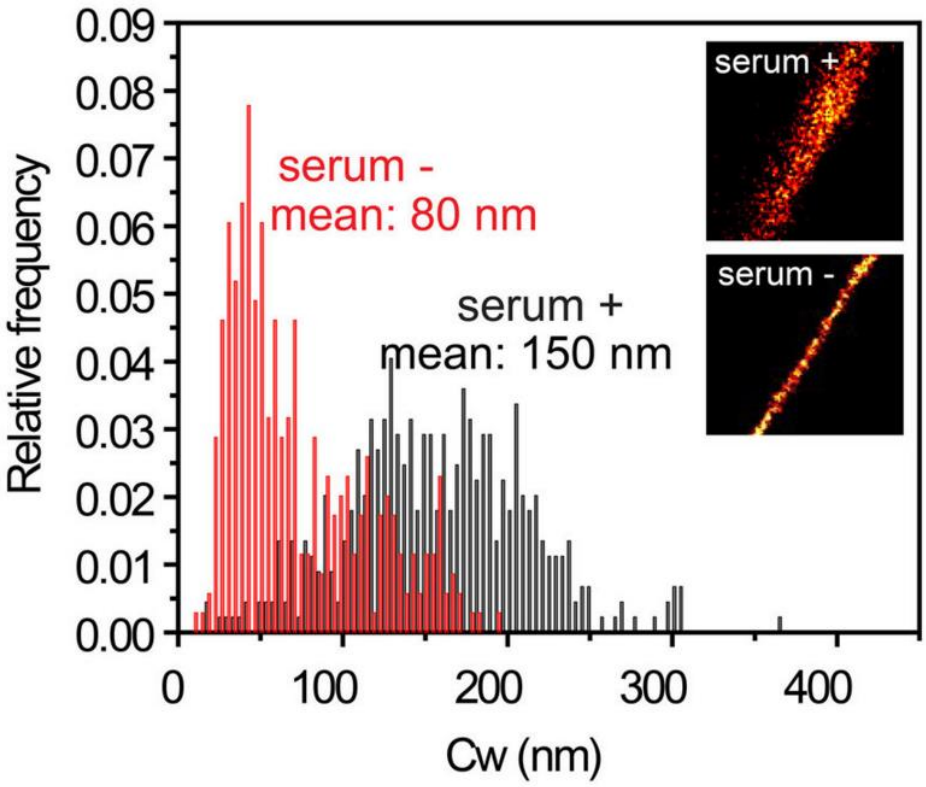

Figure 4.9 Condensed chromatin after serum starvation.

Normalized histogram of the chromatin width (Cw) in serum +/− conditions. Insets are the representative BALM images of serum +/− chromatin.

After filtering out low-level noise signals, distinct punctate structures (nodes) along fibers were observed (Figure4.10 A, C). Additionally, spatial correlation analysis (*Method and Materials*) showed smaller intervals (164±37 nm (mean ± SD)) between two punctate structures in serum (-) chromatin fibers. This was compared to serum (+) chromatin fibers of the same length where the distance between two punctate structures was 673±187 nm (mean ± SD) (Figure4.10).

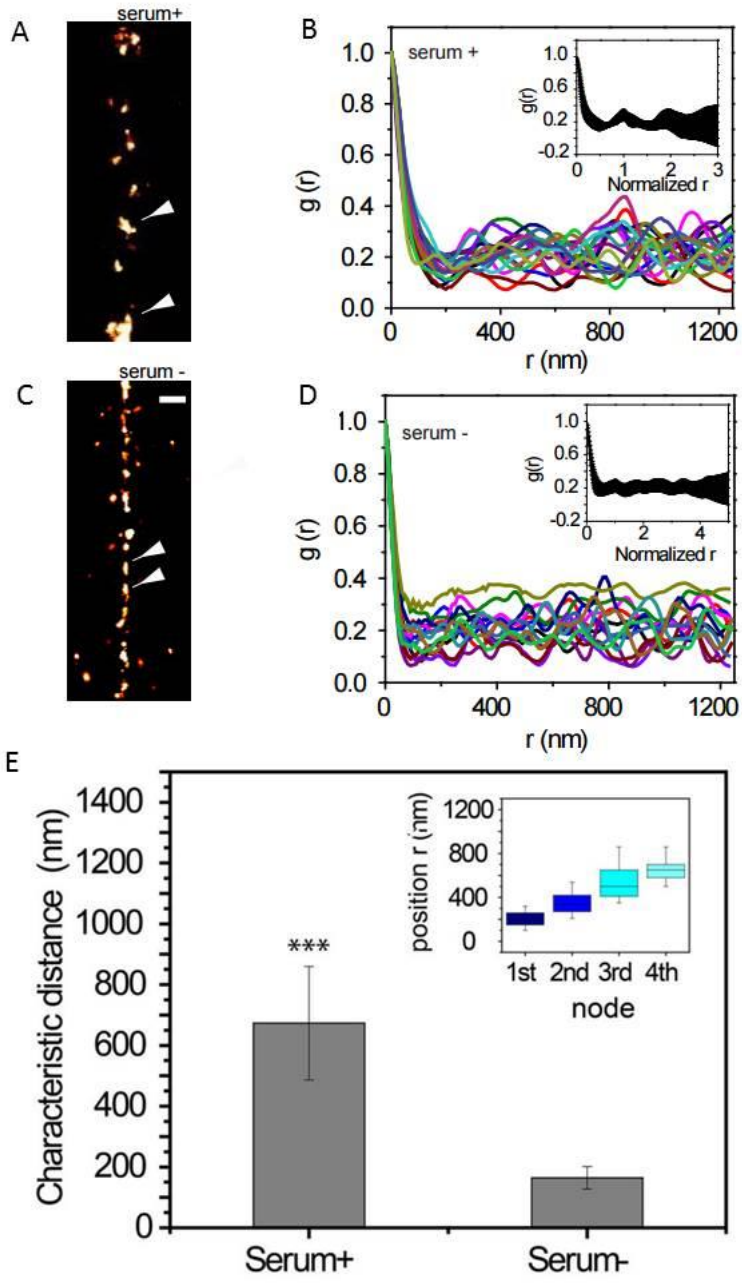

Figure 4.10 Spatial correlation analysis of chromatin fibers in serum -/ + conditions.

(A) Filtered image of super-resolution serum + chromatin spread. White arrow heads indicate the nodes. (B) Spatial correlation of multiple serum + chromatin fibers. Inset: averaged spatial correlation of multiple serum + chromatin fibers. (C) Filtered image of super-resolution serum - chromatin spread. White arrow heads indicate the nodes. Scale bar: 200 nm. (D) Spatial correlation of multiple serum - chromatin fibers. Inset: averaged spatial correlation of multiple serum - chromatin fibers. (E) Bar graph shows the characteristic distance between two nodes of chromatin fibers ($n \geq 15$) in serum +/− conditions from spatial correlation analysis (***$P < 0.001$; Student's t-test). Insets: Box graph shows the periodicity of nodes.

The structural changes of chromatin at actively transcribing and quiescent states are important for the function and localization of transcriptional machinery. Because of this we next investigated regions of chromatin that are enriched with transcriptional machinery. The colocalization of chromatin and RNA pol II in chromatin spreads prepared with and without serum conditions were also compared.

4.4 BALM detects transcriptional regions on chromatin fibers

Transcriptionally active RNA pol II (phospho S5CTD) was immunolabeled in isolated nuclei and this was followed by chromatin spreading. Chromatin fibers were labeled with YOYO-1. RNA pol II was labeled with a primary antibody (anti-RNA polymerase II CTD repeat YSPTSPS (phosphor S5), ab5131) and a secondary antibody conjugated with Alexa 647. Super-resolution images of RNA pol II were taken via direct STORM (dSTORM) by first increasing laser power to 100% and then decreasing to 2% for imaging. Resolution of 5S RNA pol2 was significantly increased using BALM imaging compared to TIRF imaging (Figure4.11).

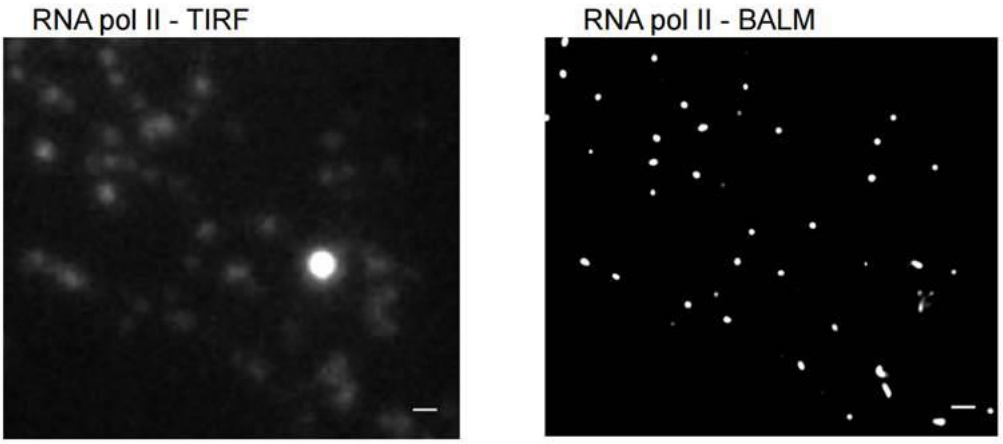

Figure 4.11 TIRFM and BALM imaging of 5S RNA pol2.

Scale bar: 500nm.

Interestingly, after superimposing signals of RNA pol II and chromatin fibres, RNA pol II was found to be enriched in gap structures, which were characterized by regions of low YOYO-1 fluorescence intensity (Figure4.12).

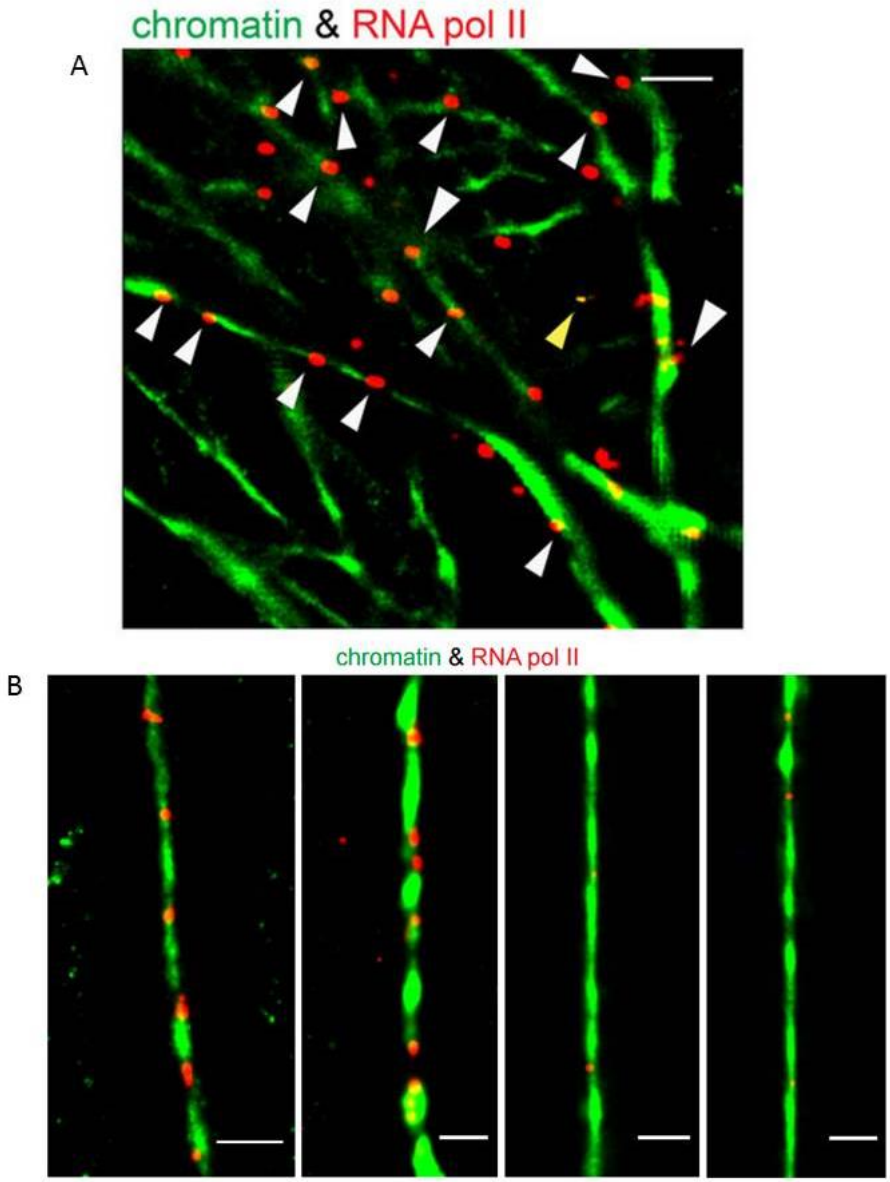

Figure 4.12 Colocalization of decondensed regions with 5S RNA pol2.

(A) BALM imaging of 5S RNA pol2 (red) and chromatin spreads (green). Scale bar: 1 μm. (B) BALM imaging of 5S RNA pol2 (red) and chromatin spreads (green). Scale bar: 500 nm.

To quantitatively assess the correlation between 5S RNA pol2 and gap structures, BALM data sets, which were obtained from visualizing chromatin fibers, and dSTORM data sets, which were obtained from visualizing 5S RNA pol2, were post-processed. This involved reconstructing ten thousand diffraction-limited images and subsequently retaining points with a localization precision of < 20 nm in both data sets. The final images were constructed

by fitting a Gaussian function (*Materials and Methods*) to each selected point in the images and merging them together. Line intensity profiles were plotted along fibers in the final image, and regions with a mean intensity at least two times lower than that of the neighbouring region was defined as a gap structure (Figure4.13A). Gap structures were characterized by measuring their length (gap chromatin length: GCl) and width and were found to be 388±170 nm (mean ± SD) and 60±25 nm (mean ± SD) respectively (Figure4.13A-C).

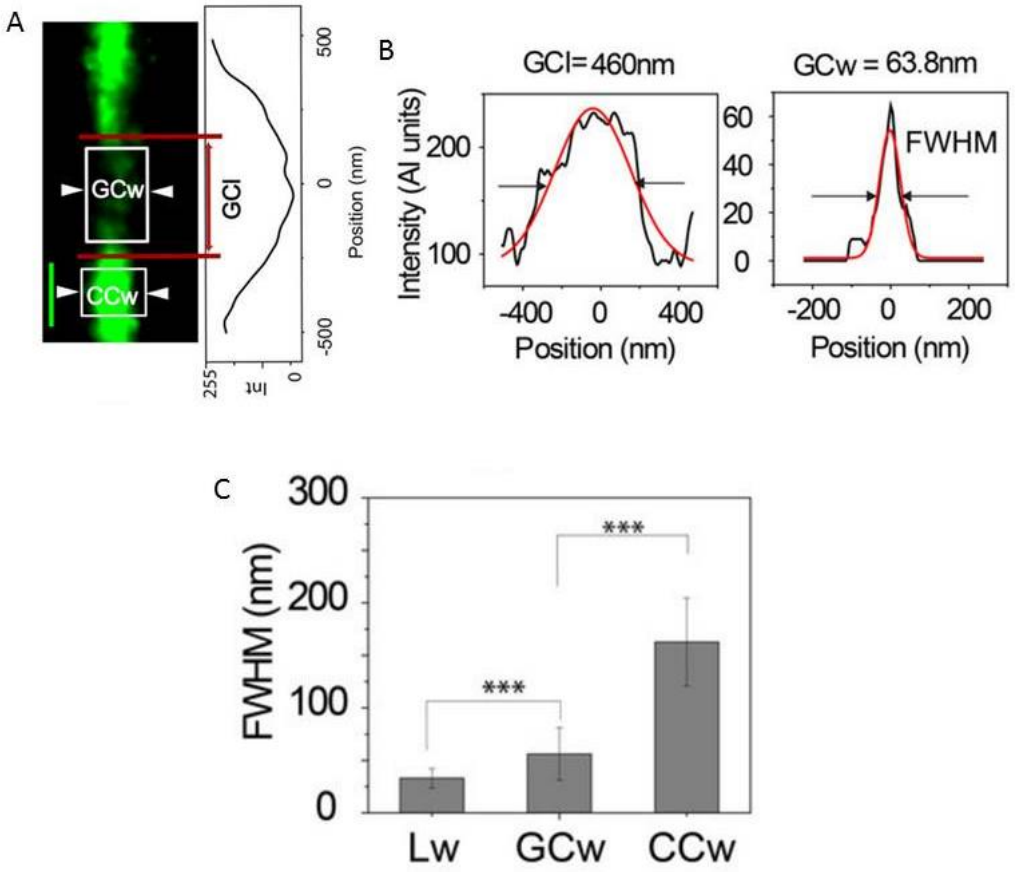

Figure 4.13 Quantification of gap structures detected by BALM imaging.

(A) A representative zoomed in BALM image of gap structure with an intensity line plot along the structure. Scale bar: 200 nm. (B) Representative line profile for the gap chromatin length (GCl) and gap chromatin width (GCw) denoted by the red lines and white boxes in (A). (C) Bar graph showing the λDNA width (Lw) (n = 50), gap chromatin width (GCw) (n = 50), and condensed chromatin width (CCw) (n = 50) (***P < 0.001; Student's t-test).

Reconstruction of super resolution images from a different number of acquisition frames

ruled out the possibility that gap structures were an imaging artefact. Gap structures colocalized with 5S RNA pol2 remained gap structures even after reconstructing ten thousand frames, while an artificial gap structure was gradually filled up when more frames were collected (Figure4.14A, B). To filter out artificial gap structures, Figure 4.14C shows that at least 7000 frames are required.

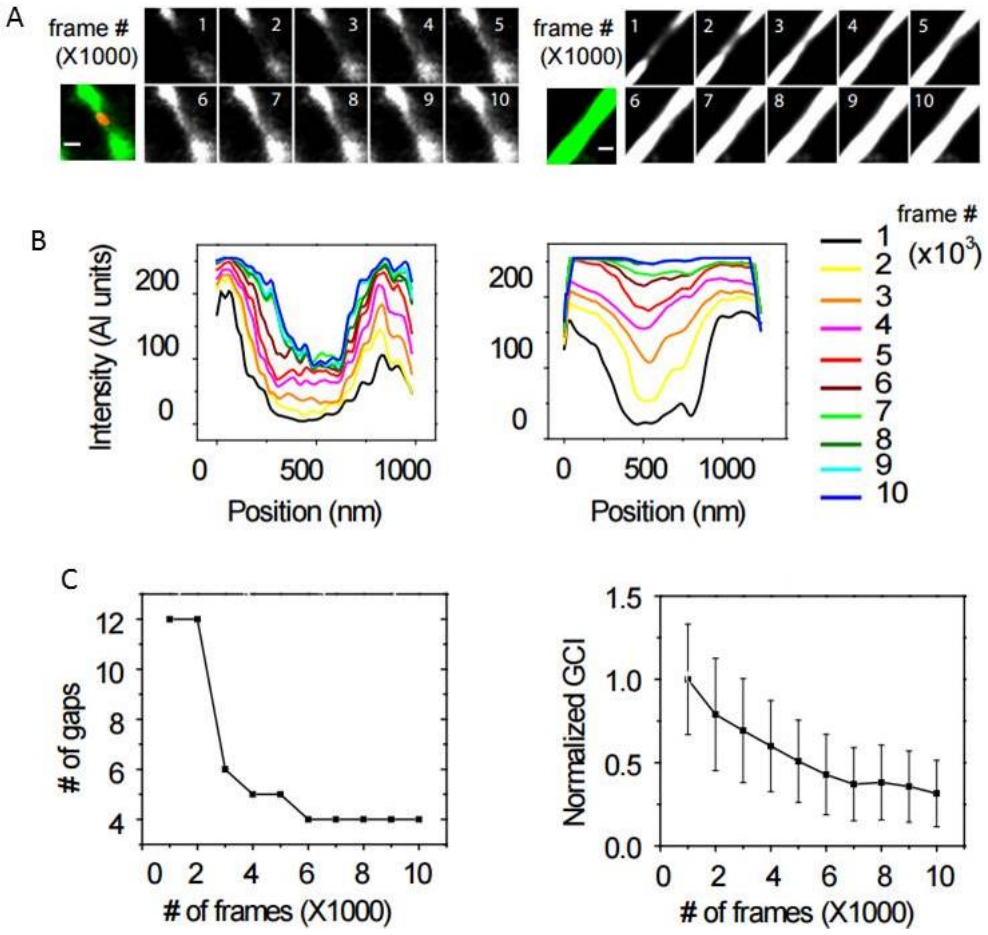

Figure 4.14 Transcriptionally active gap structures are independent of frame numbers or photons collected while imaging.

(A) Collage of BALM images of chromatin fiber with different frame numbers. The cluster in red is 5S RNA pol2. Scale bar: 200 nm. (B) Intensity line profiles showing that the active gap still remained, while the inactive gap was filled up with the increase in the frame number. (C) The graphs showing that the number of gaps as well as the normalized gaps length (GCl) decrease as the frame number goes up and finally became almost constant after ~7000 frames.

5S RNA pol2 signals were considered to co-localize with chromatin fibers if the distance between their center point and the center of the fiber cross-section (D_{p2c}) was within 20 nm

(Figure4.15). This distance also represented the upper limit of the localization precision in our experiments.

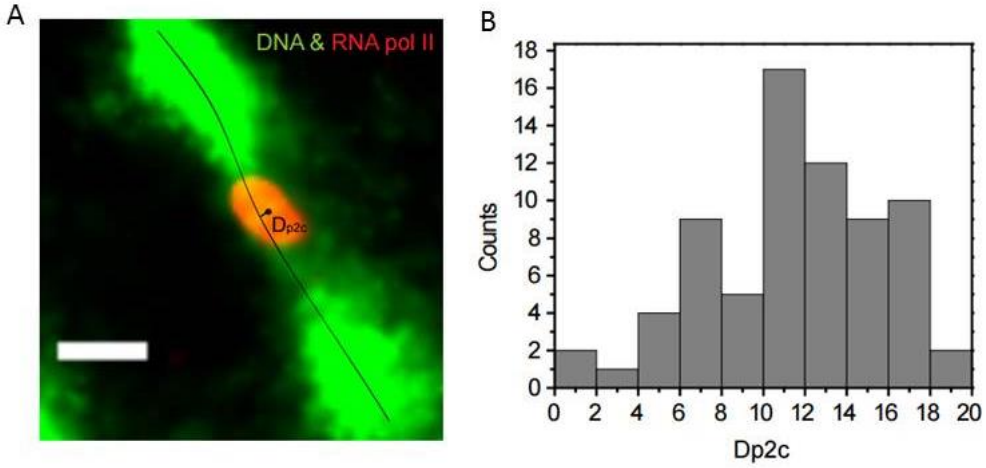

Figure 4.15 Colocalization analysis for gap structures and 5S RNA pol2.

(A) A representative dual-colorBALM image of gap structures (green) and RNA pol II (red). Scale bar: 200 nm. The distance between the centroid of 5S RNA pol2 staining and the cross-section center of gap (Dp2c) is denoted in black on the image. (B) Histogram of Dp2c shows that the selected 72 gap strucutres enriched with 5S RNA pol2 have Dp2c within 20 nm.

Similar post-processing was carried out when analyzing the localization of the transcription factor Serum Response Factor (SRF) on chromatin fibers. This transcription factor was also enriched in gap structures (Figure4.16).

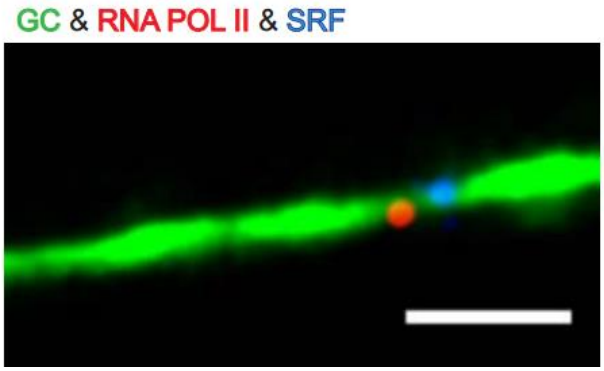

Figure 4.16 The presence of 5S RNA pol2 and SRF at serum+/- conditions.

Representative three-color BALM images of chromatin (green), 5S RNA pol2 (red) and SRF (blue) in serum +/- conditions. Scale bar: 500 nm.

To statistically quantify the correlation between 5S RNA pol2 and the gap structures, we analyzed one hundred gap structures, which were chosen randomly from dual color images of 5S RNA pol2 and chromatin fibers. 5S RNA pol2 was found to be co-localized with ~70% of the gap structures analyzed (Figure4.17). Similar analysis of one hundred randomly chosen 5S RNA pol2 signals showed 75% to be co-localized with gap structures (Figure4.17). In contrast to this observation, only ~10% of the heterochromatin protein 1α (HP1 α) signals were found to co-localize with gap structures (Figure4.17).

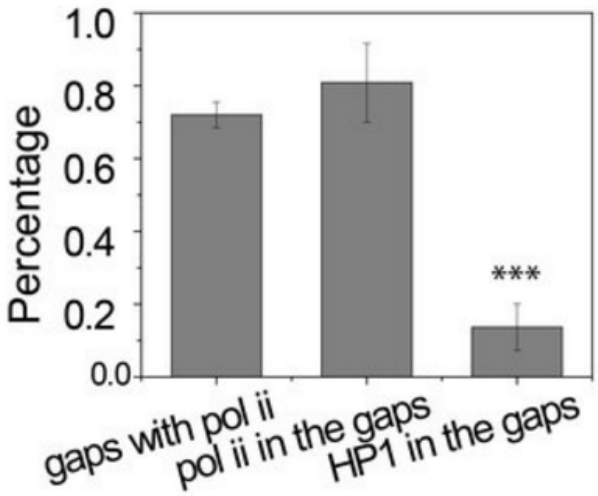

Figure 4.16 Quantification of gap structures.

Bar graph showing the percentage of gaps with 5S RNA pol2, the percentage of 5S RNA pol2 sitting in gaps, and the percentage of HP1α sitting in gaps (n = 20) (***P < 0.001; Student's t-test).

The transcriptional relevance of gap structures was further tested by inducing transcriptional repression by withdrawing serum from culture medium. In serum (-) conditions, the normalized density of gap structures along 10-μm chromatin fibers was less than half of that measured under serum (+) conditions (Figure4.18A). Concomitantly there was a decrease in 5S RNA pol2 number, as well as SRF co-localization, on chromatin fibers (Figure4.18B).

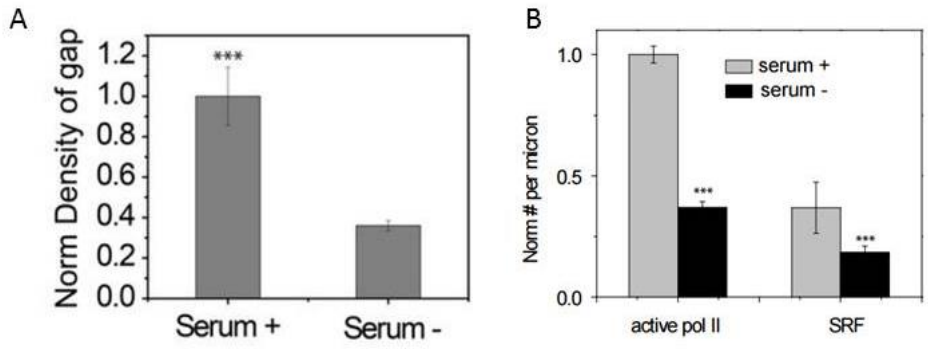

Figure 4.17 Quantification of gap structures after serum starvation.

(A) Bar graph showing the normalized density of gap structures along 10-µm fibers in serum +/– conditions (n = 30) (***P < 0.001; Student's t-test). (B) Bar graph of the density of 5S RNA pol2 and SRF along chromatin fibers in serum +/- conditions (n≥10) (***P<0.001; Student's t-test).

By combining open chromatin spreads with BALM, we have generated a robust yet simple strategy for visualizing the structure of active chromatin with a spatial resolution of ~20 nm. This approach allows for the detection of structural changes in chromatin, specifically in fiber width, or in the characteristic distances between two punctate structures. It also reveals transcriptionally active regions characterized with 5S RNA pol2 and decondensed chromatin structures, which are sensitive to serum starvation. Moreover, the open chromatin spreads can be modified for direct visualization of chromosomal contacts using BALM, which enables the investigation into the role of cell geometry on specific chromosomal contacts formation for genome regulation. Results regarding chromosomal contacts are described in the following sections.

4.5 BALM imaging of digested chromatin fragments

To dissociate chromosomal contacts from chromosome territories, we incorporated a DNA digestion step while preparing open chromatin spreads. Isolated nuclei were digested using the HindIII restriction enzyme (Figure4.19), which cleaves the A-A bond within the short AAGCTT sequence. Transcription-dependent chromosomal contacts requires transcription machinery such as RNA pol2 and specific transcription factors to co-regulate multi-gene

complexes. Masking with transcription machinery makes DNA not accessible for restriction enzymes. Hence, digestion of an intact nucleus resulted in short chromatin fragments including chromosomal contacts encapsulated by the nuclear envelope. The isolated nuclei with digested chromatin fibers and immunostained proteins were swollen and burst, allowing chromatin fragments associated with transcription machinery to spread on glass slides (Figure 4.19). On the other hand, digested chromatin fragments with immunostained proteins were pulled down by magnetic beads coated with antibodies to specific transcription factors. The pulled-down fragments were reverse crossed-linked, purified, and amplified, which were then subjected to an EpiTect ChIP qPCR array (Figure 4.19).

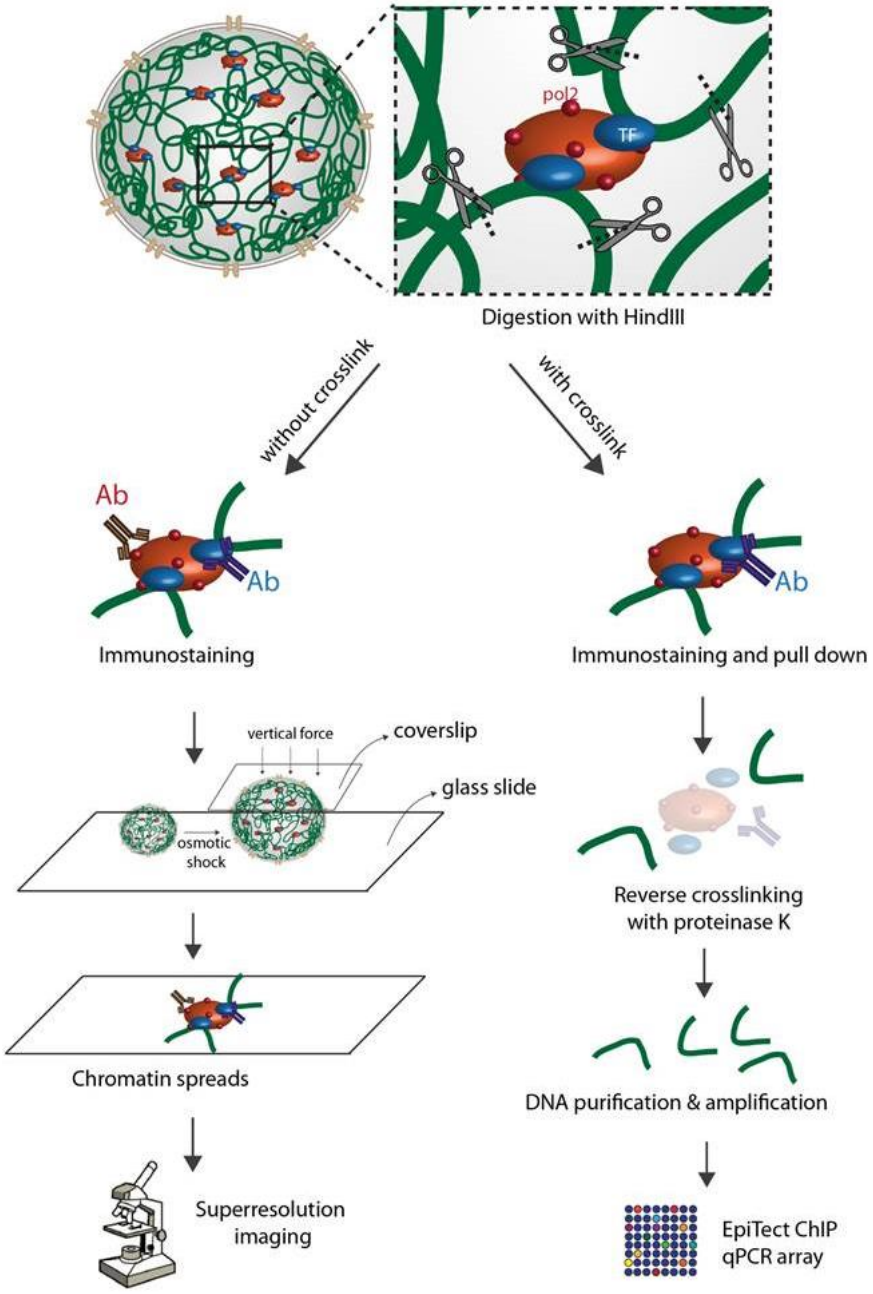

Figure 4.18 Brief overview of the chromosomal contacts preparation.

DNA is digested by HindIII within the intact nucleus. For superresolution imaging, nuclei are not crosslinked, and the chromatin is immunostained with antibodies recognizing 5S RNA pol2 and transcription factors (TFs). Following that, nuclei are subjected to osmotic shock, and then burst with compressive load to spread chromatin fragments on glass slides for imaging. For EpiTect ChIP analysis, crosslinked and digested chromatin fragments are pulled down with magnetic beads coated with an antibody recognizing the transcription factor NF-κB (p65). Chromosomal contacts associated with p65 are reversely crosslinked, and the DNA from the chromosomal contacts is purified and amplified, before performing EpiTect ChIP qRCR assay.

TIRFM imaging of digested chromatin spreads revealed short chromatin fragments with an average length of 1.5 μm. This is consistent with theoretical length of HindIII digested chromatin fibers (Figure 4.20). The undigested chromatin spreads, on the other hand, were long and continuous fibers (Figure4.20A).

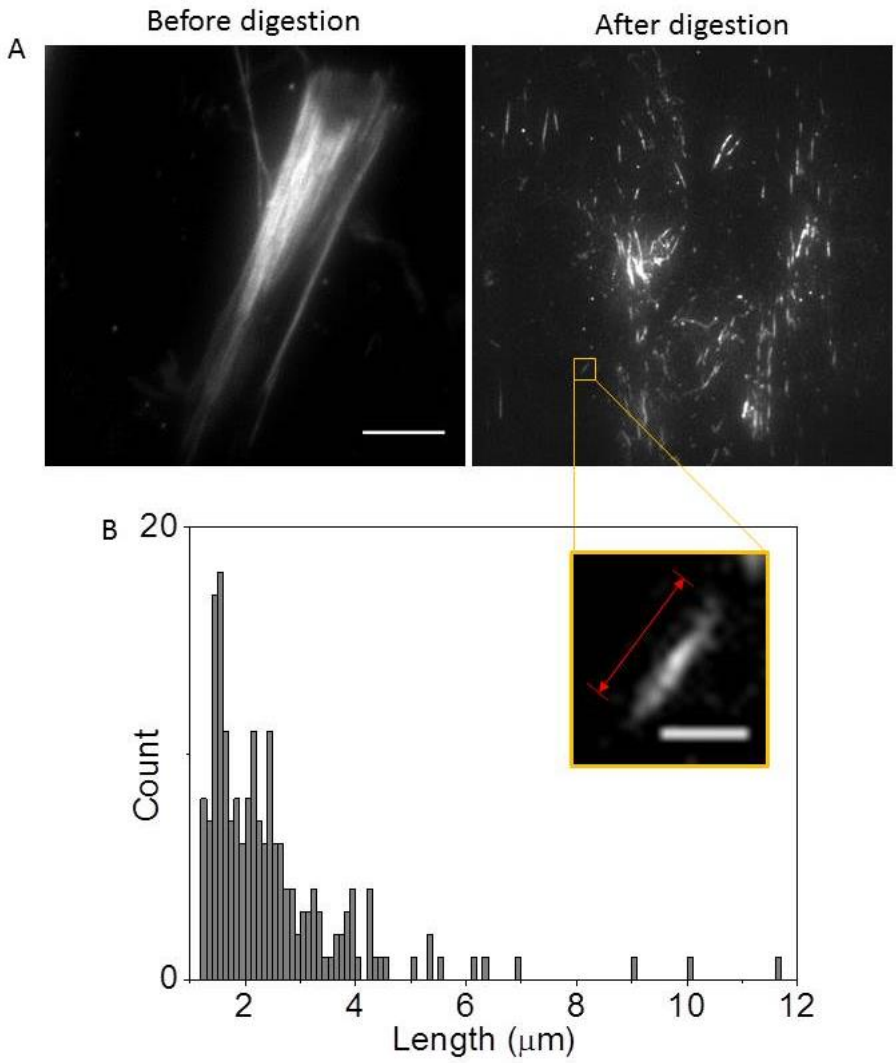

Figure 4.19 TIRFM imaging of digested chromatin fragments.

(A) TIRF images of chromatin spreads with and without digestion. Scale bar: 10 μm. (B) Length distribution of digested chromatin fragments. Inset: zoomed in image of the region outlined by the orange box in (A). Scale bar: 1 μm.

Unlike other biochemical techniques such as 3C-based methods, cells were not fixed for superresolution imaging. This fixation step was omitted for three reasons. Firstly, the fixatives would introduce imaging artifacts of non-specific contacts. Secondly, fixed nuclei are more difficult to burst through swelling and mechanical rupturing, and therefore the chromatin fragments would be poorly spread (Figure 4.21). Thirdly, the strong binding affinity between active transcription machinery and DNA preserves activated RNA pol2 and specific transcription factors on digested chromatin fragments even without fixation.

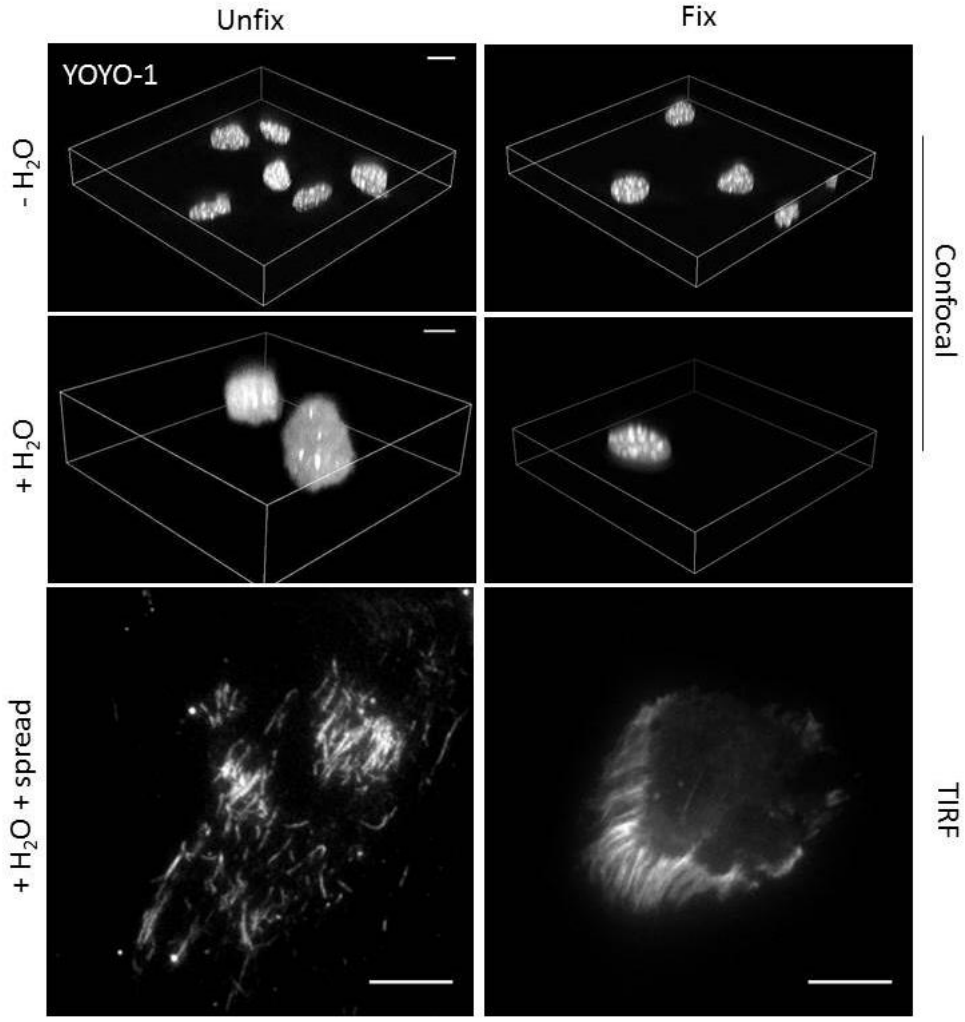

Figure 4.20 Digested chromatin spreads prepared with/ without fixation.

Confocal images of intact nuclei and TIRF images of digested chromatin spreads with or without fixation. Scale bar: 10 μm.

Next we visualized the digested chromatin fragments using BALM [59]. Chromatin fragments were again labeled with YOYO-1 and imaged in the ROX buffer. Whereas conventional microscopy only resolved the chromatin fragments as blur structures (Figure 4.22A, B), BALM imaging of these digested fragments resolved the fine "chromosomal contact" structures that contained more than one DNA fiber (Figure 4.22C). To characterize these well-resolved chromosomal contacts, we measured the thickness of the thinnest DNA fiber within one chromosomal contact. We found that the average thickness was 30-35 nm. Notably, we previously measured the thickness of λDNA using the same imaging strategy and found that the average thickness was also ~30nm [74]. This suggested that the fibers in digested fragments are not necessarily real 30-nm chromatin fibers whose existence has been in controversial [75].

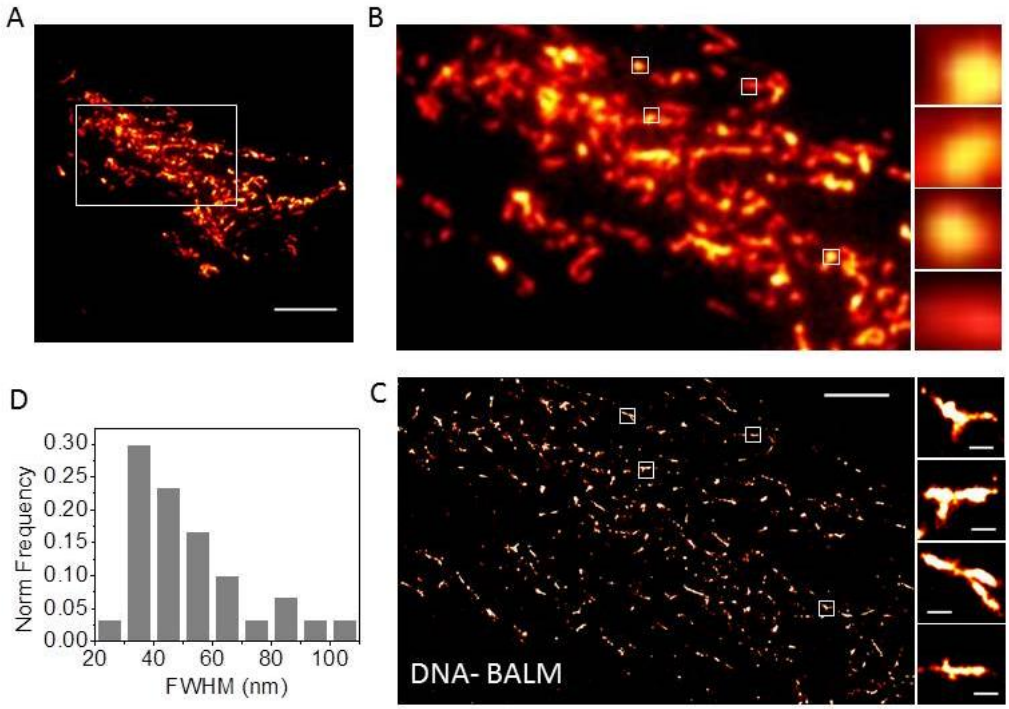

Figure 4.21 BALM imaging of digested chromatin fragments reveals chromosomal contacts.

(A) TIRFM image of digested chromatin fragments. Scale bar: 10 μm. (B) Zoomed in TIRF image of the region outlined by a white box in (A). Inset: zoomed in images of the regions outlined by white boxes in (B). (C) Zoomed in superresolution image of the region outlined by a white box in (A). Scale bar: 2 μm. Inset: zoomed in images of the regions outlined by white boxes in (C). Scale bar: 200 nm. (D) Width distribution of chromosomal contacts visualized by superresolution microscopy.

4.6 Chromosomal contacts are lost upon transcriptional quiescence

To check whether chromosomal contacts are formed randomly (i.e. through the overlapping of one DNA fiber on top of another), or by functional clustering, we forced cells into a transcriptionally quiescent state by serum starving them for 36 hrs. A proportion of the serum starved cells were stimulated with 10% FBS for 12 hrs to reboot their transcription activity. Interestingly, we found that in cells cultured with a normal serum supply, ~60% of the fragments were found to be chromosomal contacts. However, in transcriptionally quiescent cells, only ~20% of digested chromatin fragments comprised of chromosomal contacts (Figure 4.23). This indicated that the formation of the chromosomal contacts visualized using superresolution microscopy was dependent on the cells transcriptional activity.

To further confirm the chromosomal contacts are transcriptionally specific, we immunostained 5S phosphorylated RNA polymerase II (5S RNA pol2) and the serum response factor (SRF) together with chromosomal contacts, and performed three-color BALM imaging. TetraSpeck™ beads were used for channel alignment and drift correction. To avoid bias in quantification, we selected a small region of interest (ROI) around the chromosomal contact in the channel of DNA, and then we checked the channels of 5S RNA pol2 and SRF respectively to see whether there are 5S RNA pol2 and SRF clusters in this region. ROIs with both 5S RNA pol2 and SRF signals were scored as positive. We found that in serum stimulated cells ~30% of the chromatin fragments were chromosomal contacts associated with 5S RNA pol2 and SRF, whereas in serum starved cells less than 10% were 5S RNA pol2/SRF associated contacts (Figure 4.23).

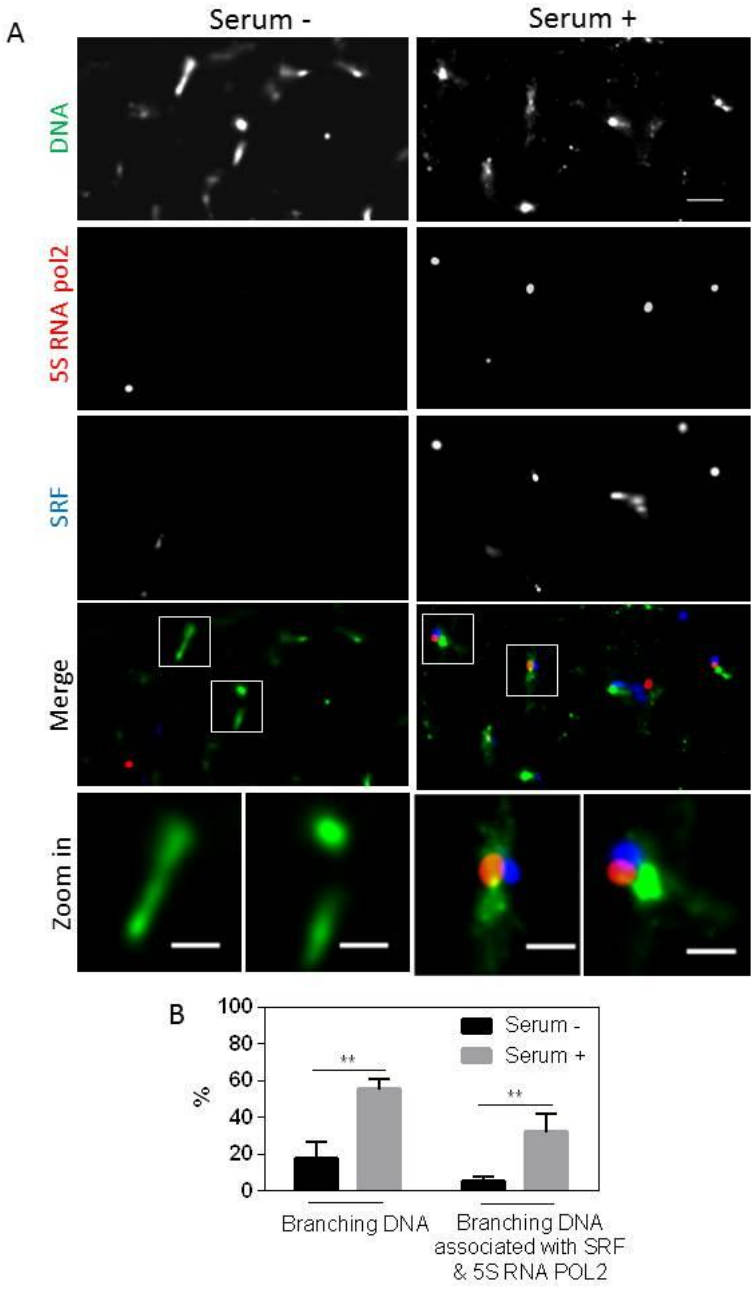

Figure 4.22 Three-color BALM imaging of chromosomal contacts with 5S RNA pol2 and the transcription factor SRF in serum +/- system.

(A) Three-color superresolution image of chromosomal contacts (green), 5S RNA pol2 (red), and SRF (blue). Scale bar: 500 nm. Insets: zoomed in images of the regions outlined by white boxes. Scale bar: 200 nm. (B) Bar graph quantifying the percentage of chromosomal contacts associated with both 5S RNA pol2 and SRF. Data is given as mean ± SD with 10<n<20. **P<0.01; Two sample student's t test.

4.7 Visualization of YAP target chromosomal contacts

Next we went on to visualize other specific chromosomal contacts under different conditions. Firstly, we cultured mouse fibroblasts on micro-fabricated fibronectin-coated patterns to generate different cell shapes. We then examined the localization of YAP, and its influence on chromosomal contacts. YAP, a transcription coactivator, relays mechanical signals exerted by ECM rigidity and cell shape to the nucleus [15]. Using patterned substrates to confine cells in a particular geometry, we tested whether our method could detect differential levels of YAP targeted chromosomal contacts regulated by cell geometric constraints.

To achieve this, we removed the cytoplasm from the cells cultured on different substrates (Figure4.24). Big anisotropic substrates were used to spread cells in a manner reflective of physiological conditions, where YAP is predominantly localized in nucleus and its target genes are activated. Meanwhile, small isotropic substrates were used to exclude YAP from the nucleus, and retain it in the cytoplasm [15]. We then prepared chromatin spreads by opening up the nuclei on big anisotropic and small isotropic substrates.

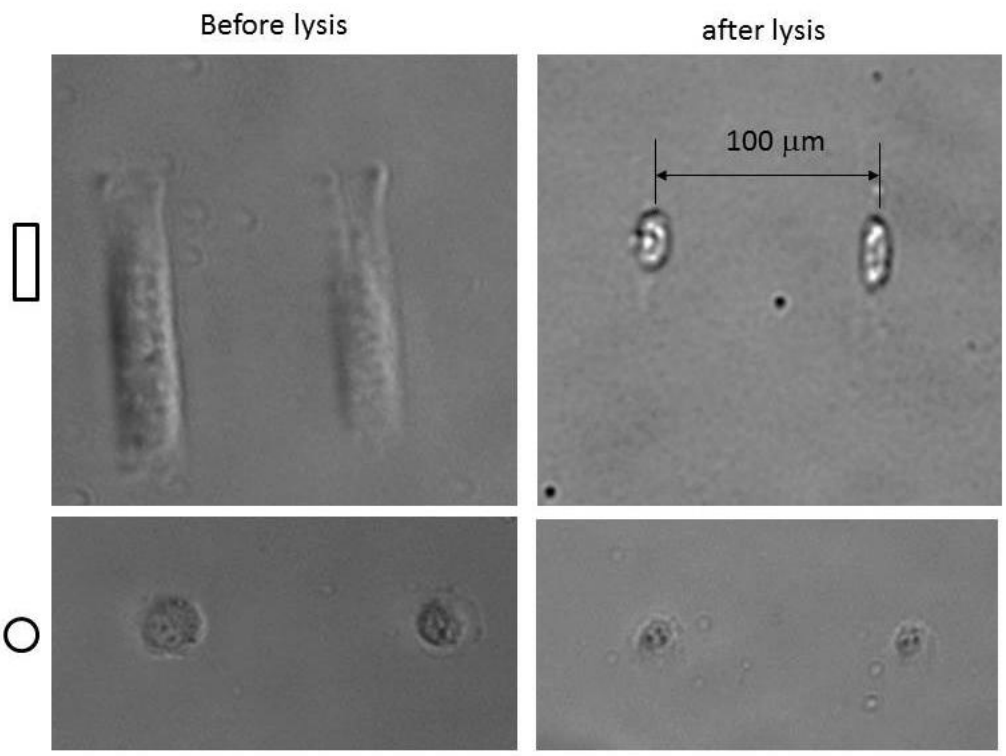

Figure 4.23 Nuclear shape was maintained after cytoplasm removal.

Bright field images of cells and nuclei on either anisotropic (rectangle) or isotropic (circle) substrates.

TIRFM imaging of digested chromatin fragments showed that 5S RNA pol2 was preserved on both AP and IP substrates. However, YAP was more highly associated with chromatin fragments in cells cultured on AP substrates (Figure 4.25).

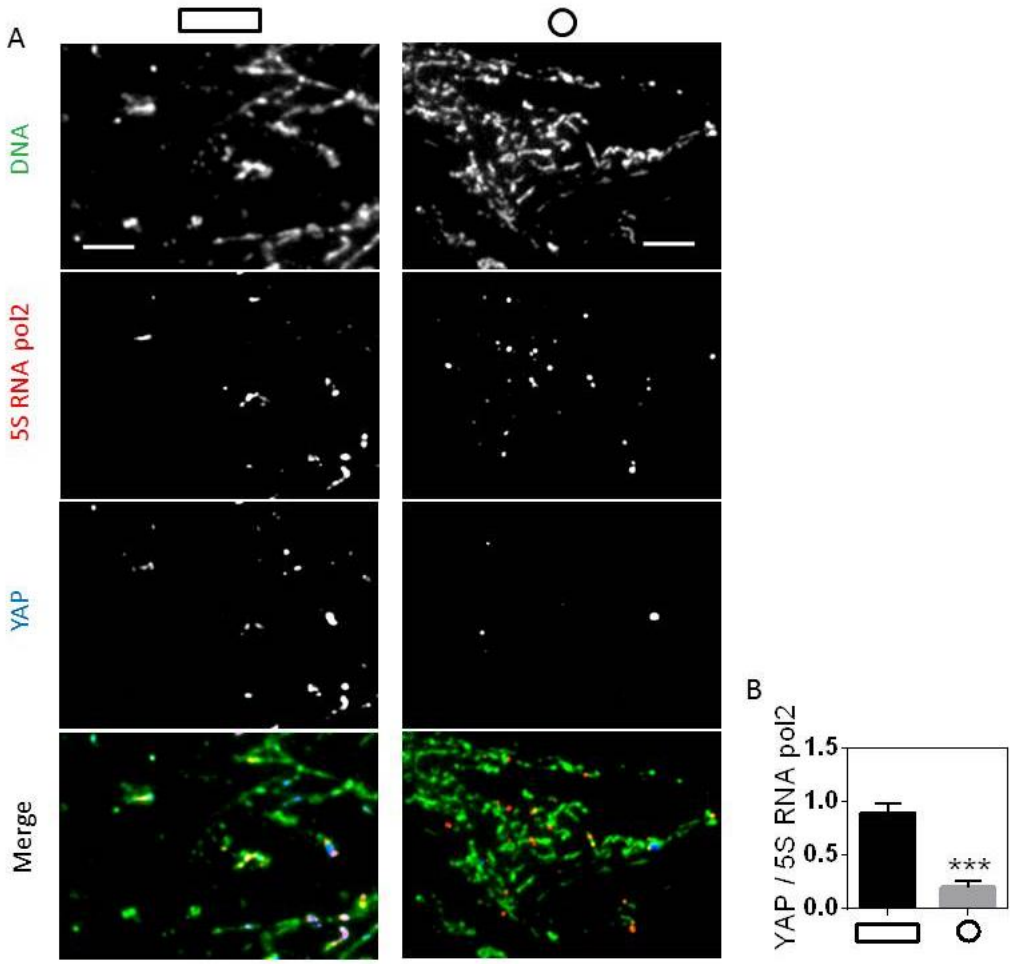

Figure 4.24 TIRFM images of digested chromatin fragments with 5S RNA pol2 and the transcription factor YAP under geometric confinement.

(A) Three-color TIRF images of chromatin fragments (green), 5S RNA pol2 (red), and YAP (blue). Scale bar: 5 μm. (B) Bar graph quantifying the ratio of YAP and 5S RNA pol2 total intensity. Data is given as mean ± SD with 10<n<20. ***P<0.001; Two sample student's t test.

BALM imaging of these digested fragments further revealed chromosomal contacts associated with 5S RNA pol2 and YAP (Figure 4.26A-E), with a significantly higher level of such contacts in spreading cells (Figure 4.26F). Some of the chromatin fragments were longer and not resolved as chromosomal contacts. These fragments were not considered in our quantification as they could be due to incomplete digestion of the DNA. These results suggested that our method could detect differential levels of YAP targeted chromosomal contacts regulated by cell shape.

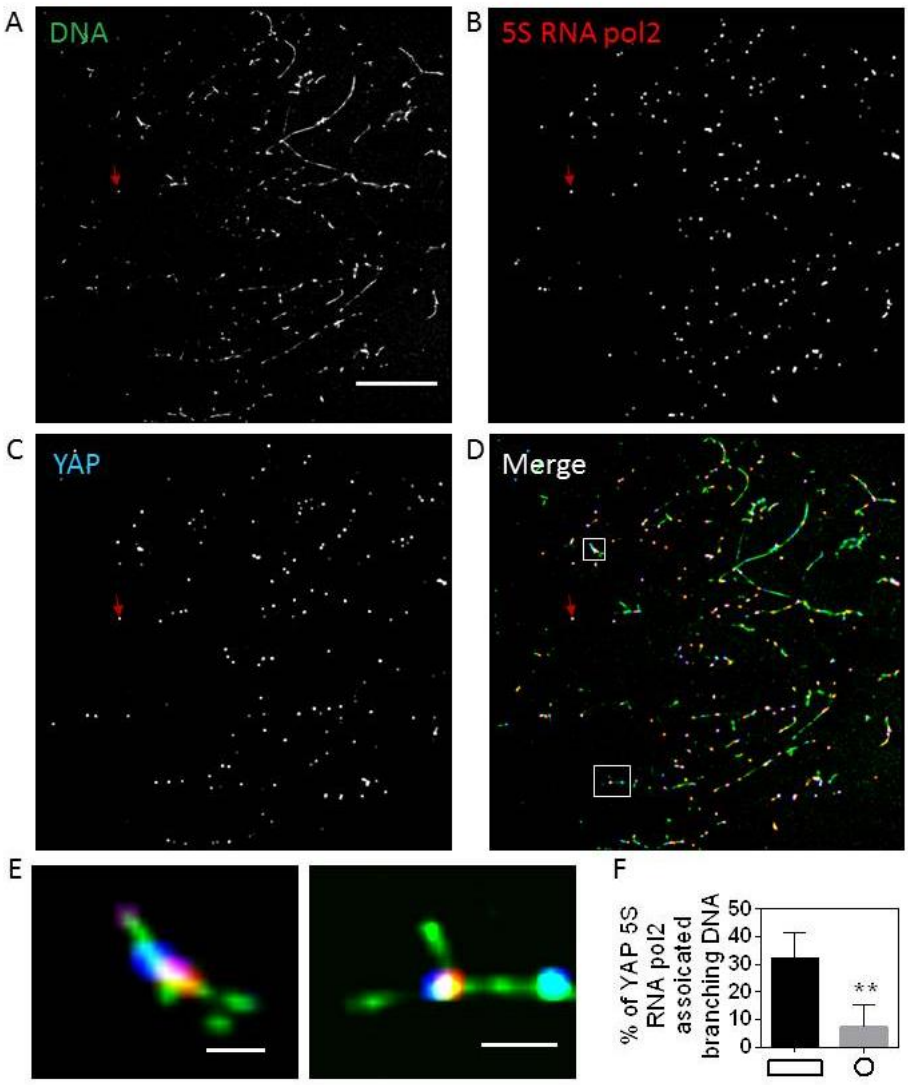

Figure 4.25 BALM imaging of digested chromatin fragments reveals YAP targeted chromosomal contacts.

Superresolution images of (A) chromosomal contacts, (B) 5S RNA pol2, (C) YAP. The red arrows indicate a TetraSpeck™ bead. Scale bar: 10 μm. (D) Three-color superresolution image of chromosomal contacts (green), 5S RNA pol2 (red), and YAP (blue). The red arrow indicates a TetraSpeck™ bead. (E) Zoomed in images of regions indicated by white boxes in (D). Scale bar: 200 nm. (F) Bar graph quantifying the percentage of chromosomal contacts associated with both 5S RNA pol2 and YAP in cells cultured on either anisotropic (rectangle) or isotropic (circle) substrates. Data is given as mean ± SD with 10<n<20. **P<0.01; Two sample student's t test.

4.8 Visualization of SRF target chromosomal contacts

We also visualized chromosomal contacts involved in the serum responsive pathway, which is known to be more active in pre-stressed cells with stabilized actin filaments as

shown in Chapter3 and [9]. Consistently, more SRF was associated with digested chromatin fragments in spreading cells cultured on big anisotropic substrates (Figure4.27). Interestingly, these chromatin fragments spread specifically throughout the AP substrates after nucleus rupture (Figure4.27A), allowing the quantification of chromosomal contacts at a single cell level.

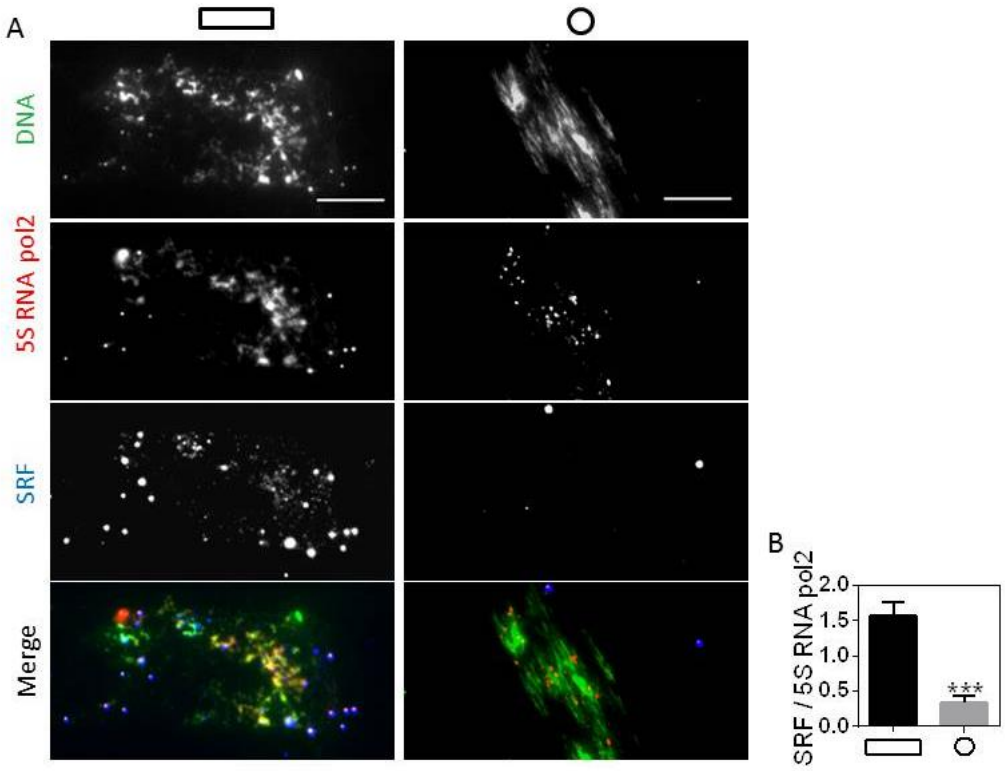

Figure 4.26 TIRFM images of digested chromatin fragments with 5S RNA pol2 and the transcription factor SRF under geometric confinement.

(A) Three-color TIRF images of chromatin fragments (green), 5S RNA pol2 (red), and SRF (blue). Scale bar: 10 μm. (B) Bar graph quantifying the ratio of SRF and 5S RNA pol2 total intensity. Data is given as mean ± SD with 10<n<20. ***P<0.001; Two sample student's t test.

BALM imaging of these fragments again revealed chromosomal contacts associated with 5S RNA pol2 and SRF (Figure4.28A, B), with a significantly higher level in cells cultured on AP substrates (Figure4.28C). Moreover, the distance between isolated nuclei was large enough to capture the digested fragments of a single nucleus, which allowed us to quantify the level of SRF targeted contacts within single cells. The error bars in Figure4.28C indicate

the variability in the amount of SRF target contacts among different cells. However, it should be noted that the percentage of the functional contacts might be under-estimated as some contacts might be lost during sample preparation.

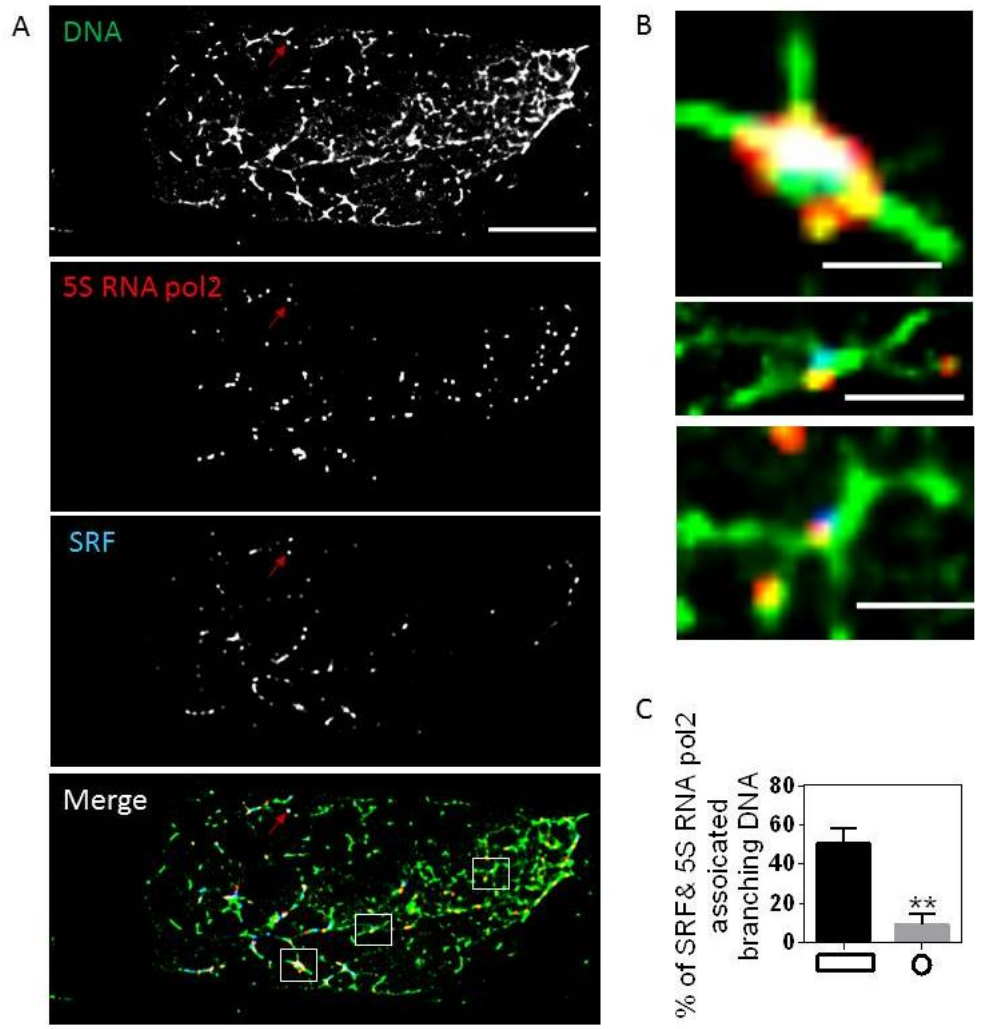

Figure 4.27 BALM imaging of digested chromatin fragments reveals SRF targeted chromosomal contacts.

(A) Three-color superresolution image of chromosomal contacts (green), 5S RNA pol2 (red), and SRF (blue). The red arrows indicate a TetraSpeck^{TM} bead. Scale bar: 10 μm. (B) Zoomed in images of regions outlined with white boxes in (A). Scale bar: 200 nm. (C) Bar graph quantifying the percentage of chromosomal contacts associated with both 5S RNA pol2 and SRF in cells cultured on either anisotropic (rectangle) or isotropic (circle) substrates. Data is given as mean ± SD with $10<n<20$. **$P<0.01$; Two sample student's t test.

4.9 Visualization of NF-κB target chromosomal contacts

Next, we checked if our method of visualizing chromosomal contact formation was sensitive to changes in the cytoplasmic to nuclear localization of transcription factors induced by cytokines. For this, we treated mechanically constrained cells with tumor necrosis factor alpha (TNF-α). TNF- α induces the nuclear localization of NF-κB transcription factors, and the subsequent expression of their target expression. As shown in Figure 4.29, we first established the nuclear localization of p65, a subunit of NF-κB, in the IP, and AP cells, as well as AP cells treated with TNF- α. Cells on IP substrates show higher nuclear localization of p65 compared to AP cells. Treatment of TNF- α on AP cells increases nuclear p65 levels.

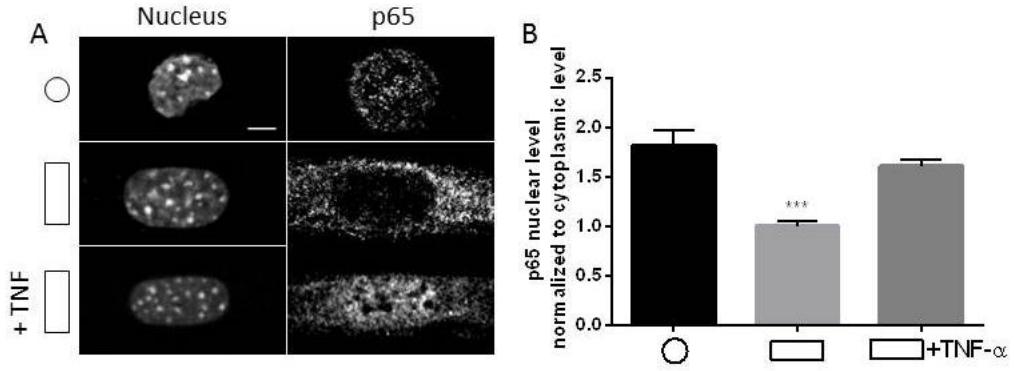

Figure 4.28 Nuclear localization of p65 regulated by cell geometry and cytokine treatment.

(A) Representative images of the nucleus, and p65. Scale bar: 5 μm. (B) Bar graph quantifying the nuclear to cytoplasmic ratio (N2C) of p65 in three conditions normalized to the condition in anisotropic substrates . Data is presented as mean ± SE with 20 < n < 30. *** P<0.001; Two sample student's t test.

TIRFM imaging of chromosomal contacts was then carried out in the aforementioned three cases. Consistent with nuclear localization of p65, there was higher amount of digested fragments associated with p65 in IP cells. Addition of TNF- α to AP cells also increased the amount of p65 associated chromatin fragments (Figure4. 30).

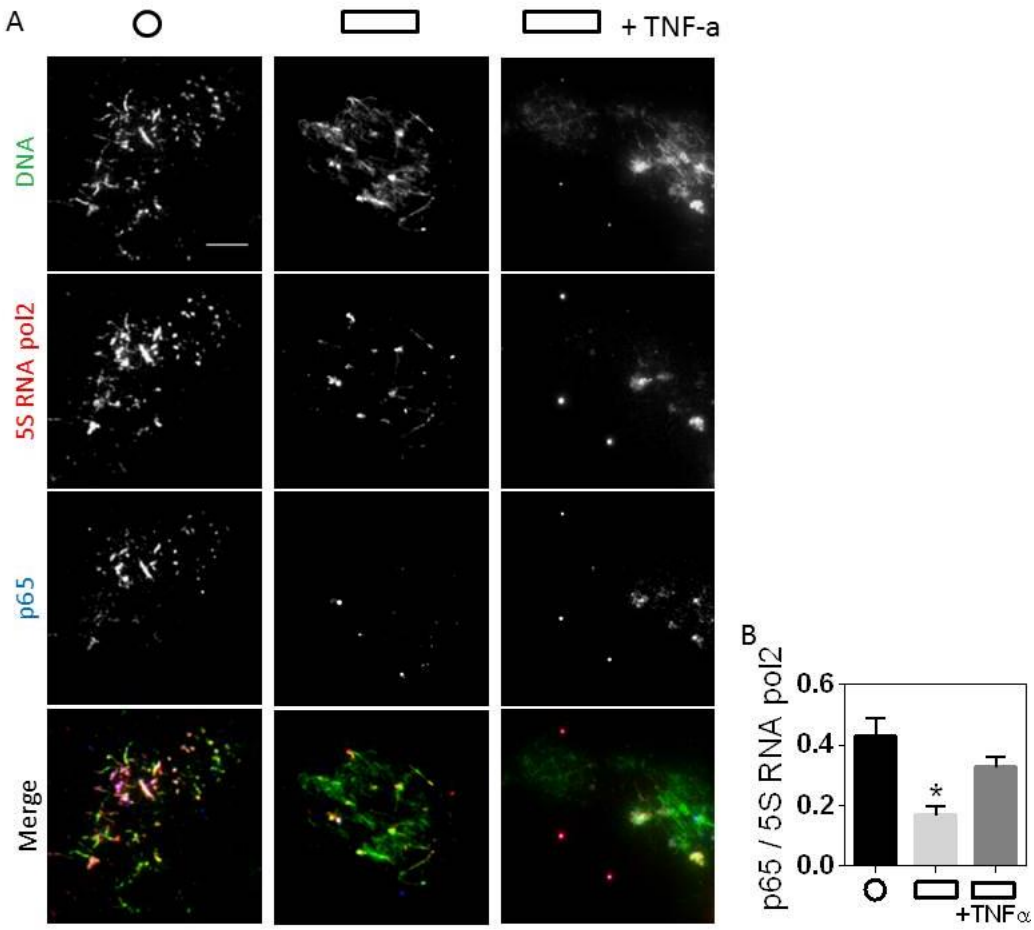

Figure 4.29 TIRFM images of digested chromatin fragments with 5S RNA pol2 and the transcription factor p65 under geometric confinement and cytokine induction.

(A) Three-color TIRF images of chromatin fragments (green), 5S RNA pol2 (red), and p65 (blue). Scale bar: 10 μm. (B) Bar graph quantifying the ratio of p65 and 5S RNA pol2 total intensity. Data is given as mean ± SD with 10<n<20. *P<0.05; one-way ANOVA test.

Furthermore, superresolution imaging revealed p65 target chromosomal contacts (Figure4.31A), particularly enriched in IP cells and AP cells induced with TNF-α (Figure4.31B).

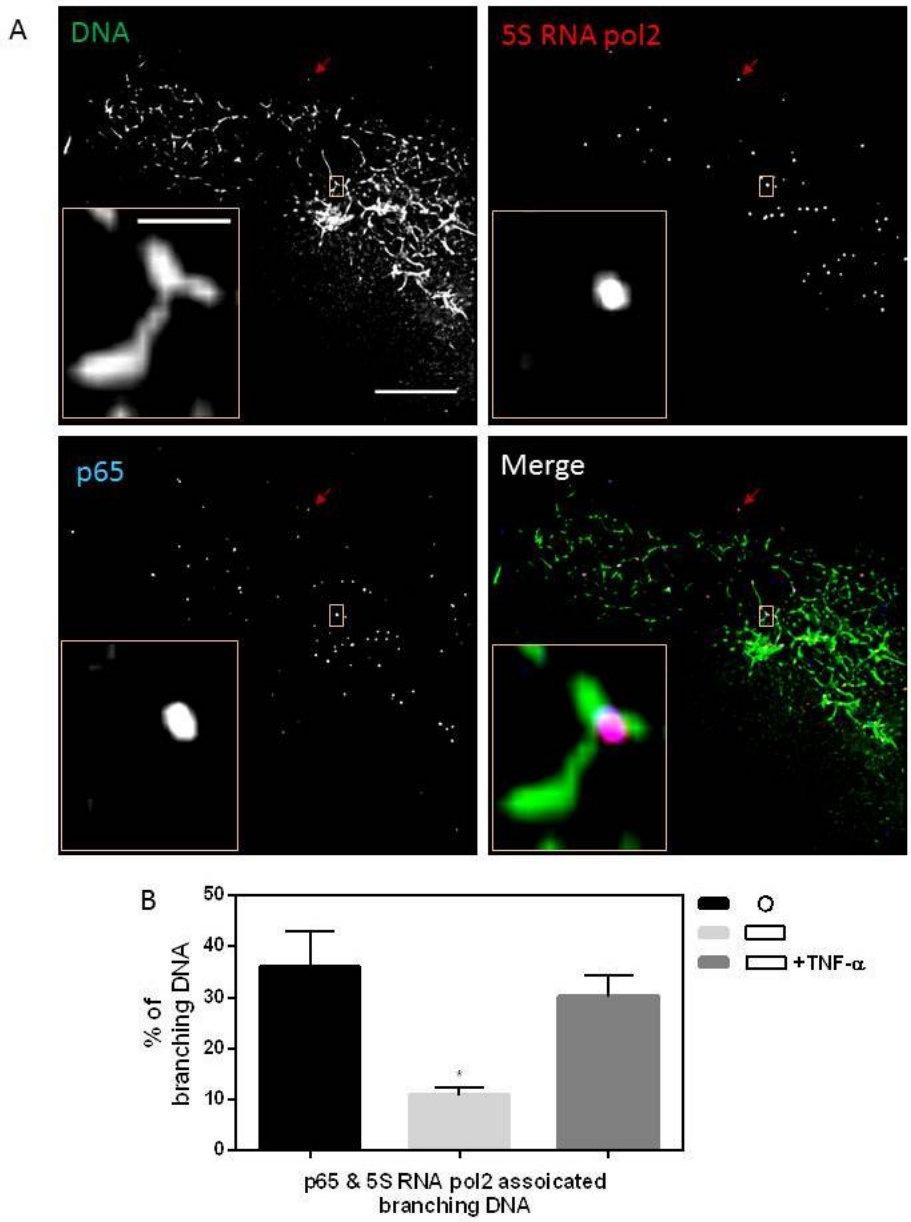

Figure 4.30 BALM imaging of digested chromatin fragments reveals a differential amount of p65 target chromosomal contacts in response to geometric confinement or cytokine induction.

(A) Three-color superresolution image of chromosomal contacts (green), 5S RNA pol2 (red), and p65 (blue). The red arrows indicate a TetraSpeck™ bead. Scale bar: 10 μm. Insets: zoomed in images of the regions outlined by orange boxes. Scale bar: 200 nm. (B) Bar graph quantifying the percentage of chromosomal contacts associated with both 5S RNA pol2 and p65. Data is given as mean ± SD with $10<n<20$. *$P<0.05$; one-way ANOVA test.

Here we visualized functional chromosomal contacts target by three specific transcription factors using superresolution microscopy in digested open chromatin spreads, suggesting

that with the availability of specific antibodies, our method could detect the level of chromosomal contacts targeted by various transcription factors under different conditions.

4.10 EpiTect ChIP analysis reveals promoter occupancy of NF-κB on its target chromosomal contacts

Although superresolution microscopy reveals the fine structures of the chromosomal contacts, the genetic information of these contacts is still lacking. To confirm the specific chromosomal contacts indeed contain particular promoter sites, we pulled down chromosomal contacts with magnetic beads coated with an antibody to p65, which served as a representative transcription factor. The DNA was then subjected to an EpiTect ChIP qPCR array with a library of primers for approximately 80 known p65 target genes. This experiment reveals the promoter occupancy of p65 on a set of genes that are likely to be contained in the pull-down chromosomal contacts.

Under different conditions, the overall trend in the p65 promoter occupancy was similar to the trend of the chromosomal contacts level targeted by p65 (Figure 4.32, Figure 4.31).

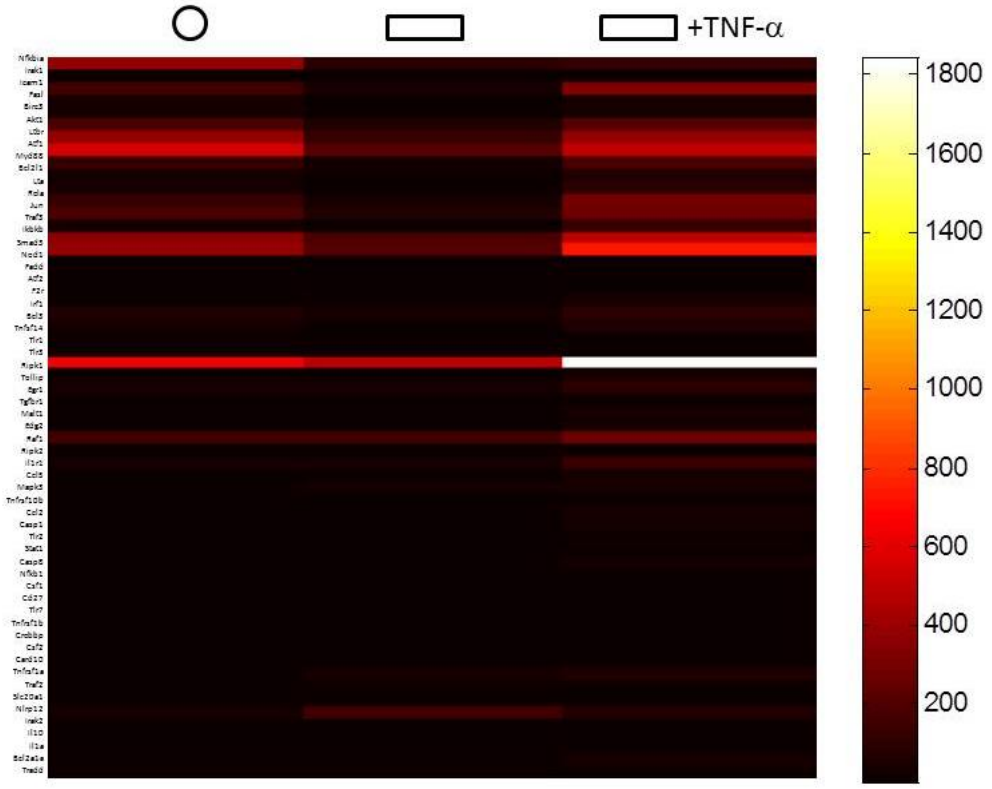

Figure 4.31 Color map of the whole set of genes with differential p65 enrichment.

Specifically, among the ~80 known p65 target genes, we found that 22 differential associations with p65 in responsive to geometric confinement and cytokine induction. Changes in association were defined by a fold change cutoff of 1.5 (Figure 4.33). More interestingly, the genes that were sensitive to geometry confinement and cytokine induction generally were more enriched with p65 compared to those with less sensitivity. This suggested that the promoters of these genes were more likely to be contained in the chromosomal contacts targeted by p65. These results confirmed that the p65 target chromosomal contacts, visualized in less-spread cells or cells with TNF-α treatment, contain promoter sites recognized by p65. Similarly, using libraries of primers for other groups of genes, one could know the genetic information of chromosomal contacts targeted by various transcription factors.

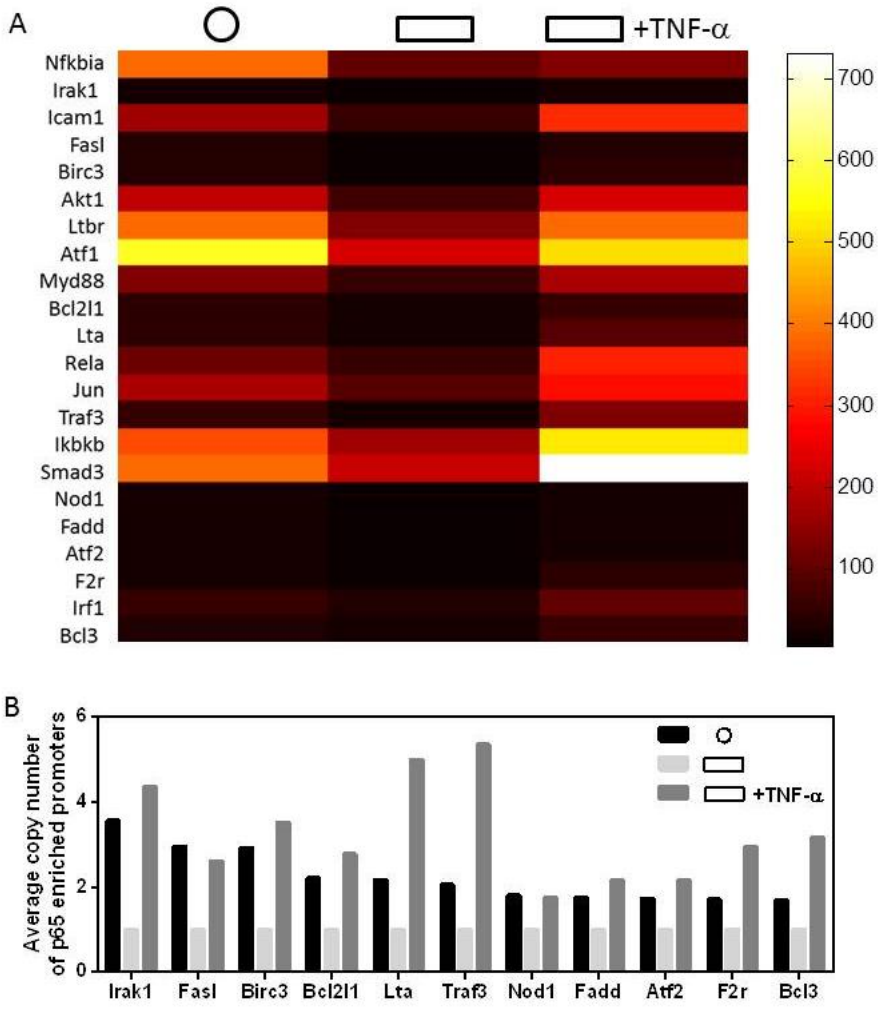

Figure 4.32 EpiTect ChIP qRCR analysis reveals particular genes with differential enrichment of p65 at the promoters in response to geometric confinement or cytokine induction.

(A) Color map of genes with differential p65 enrichment. The cutoff of fold change is 1.5. (B) Bar graph quantifying the p65 enrichment of genes indicated with darker colors in (A).

Using digested open chromatin spreads combined with superresolution microscopy, we have revealed that cell geometry indeed regulates the formation of specific chromosomal contacts. For example, in AP substrates, we observed a high level of SRF target chromosomal contacts and high expression of SRF target genes, whereas low level of p65 target chromosomal contacts was accompanied by low expression of p65 target genes. With the help of EpiTect ChIP qPCR assay we have further shown that low level of p65 target chromosomal contacts correlates with low promoter occupancy of p65 of genes such as *Nfkbia*, *Icam1*, *Akt1*, *Ltbr*, *Atf1*, *Myd88*. Interestingly, addition of cytokine in AP cells

induced the nuclear localization of p65 as well as the level of p65 target contacts, and its promoter occupancy on the same genes.

CHAPTER5: CONCLUSION, DISCUSSION, AND FUTURE DIRECTIONS

In the ***first project***, we investigated the role of cell geometry on 3D chromosome position and its implications in genome regulation. To achieve this, mouse fibroblasts were cultured on fibronectin-coated micropatterns for 3 hrs to either mimic the physiological spreading conditions, or to reduce the matrix attachment. Chromosome FISH revealed that reduction in the matrix attachment resulted in the interior movement of Chr1, 2, 11, whereas the peripheral movement of Chr3. Alterations in the radial position was concomitant with chromosome remodeling, as well as its transcription activity measured by whole genome transcriptome and level of 5S RNA pol2. Alterations in the radial position also created new chromosome neighborhood: reduction in the matrix attachment led to the increased intermingling between Chr2 - Chr6, Chr2 - Chr10, and Chr11 - Chr15, whereas the decreased intermingling between Chr5 - Chr9, in a transcription-dependent manner. Importantly, our results reveal that CTs are sensitive to the mechanical axis of the cell: when changing from IP to AP substrates, CT pairs that orientate along the Z-axis in IP substrates (e.g. Chr2-Chr10, Chr2-Chr6, and Chr11-Chr15) are moved towards the nuclear periphery, more compacted, intermingle less with other CTs, and recruit less 5S RNA pol2 in the intermingling regions. However, CT pairs that deviate most from the Z-axis in IP substrates (Chr5-Chr9) relocate towards the interior of the nucleus, are less compacted, intermingle more with each other, and recruit more 5S RNA pol2. We further showed that the intermingling regions were also enriched with a transcription factor SRF, and its target gene *zyxin*, the localization frequency of which was regulated by cell geometries. Alterations in intermingling degrees coupled with corresponding changes in chromosome activity distance as measured from the whole genome transcriptome assay.

Furthermore, our geometric model emphasizes the importance of cell geometry on chromosome reorientation and chromosome repositioning. While chromosome conformation capture models have been successful in describing the configurations in chromatin folding and activity-dependent genome-wide contacts, our geometric model can be used to analyze the coupling between chromosome packing, orientation of the CTs,

intermingling, and gene expression. When weighting the overlap by chromosome activity similarity, the resulting simulated CT arrangements showed a correlation of 0.99 between intermingling degree and chromosome activity similarity in ellipsoidal nuclei. This correlation reduces to 0.44 in spherical cell nuclei arising due to formation of new CT angular orientations and intermingling degree, suggesting that cell shape alterations lead to drastic changes in CT neighborhoods. Most importantly, without any information about chromosome activity similarity in spherical cell nuclei, our model is able to predict the qualitative changes in radial distance, angular distributions, and partially intermingling degree when going from AP to IP substrates in experiments. Results from our modelling and the transcription inhibition experiments point to conclusion that geometry change of cells is the cause of chromosome reorientation and 3D radial reorganization, which creates new neighborhoods for new contacts formation with the help of activated RNA pol2.

To further investigate the role of cell geometry on specific gene clusters at a higher resolution, we developed a novel open chromatin spreads in the ***second project***. The eukaryotic nucleus is an organelle that is densely packed with DNA and proteins. This density makes visualizing the local chromatin structure, as well as its interactions with functionally relevant proteins such as 5S RNA pol2, particularly difficult. In this study we overcame these difficulties by swelling nuclei and preparing chromatin spreads via a technique that does not disrupt chromatin architecture, as evidenced by the retention of highly dynamic linker histones, as well as the core histones on the chromatin.

The super-resolution microscopy technique, BALM, provided a direct snapshot of previously unobserved gap structures on the chromatin fiber. These images, together with images captured on a dSTORM system, further revealed a correlation between gap structures and 5S RNA pol2. ~75% of transcriptionally active RNA pol2 was co-localized with gap structures, while only ~10% of the heterochromatin protein 1 α (HP1 α) was found in gap structures. A decrease in the transcriptional activity of cells, which was

induced by withdrawing serum from their growth media, leads to a decrease in the number of gap structures, as well as 5S RNA pol2 and SRF punctae. These results suggested that our super-resolution microscopy revealed decondensed chromatin regions at active transcription sites. This method can be used to probe the physical localization of proteins relative to DNA fibers.

We further modified the open chromatin spreads method and succeeded to visualize physical chromosomal contacts or clusters, and investigated the role of cell geometries on specific chromosomal contacts. This method takes advantage of the fact that chromosomal contacts are tightly fixed by active transcription machinery and transcription factors. After dilution, non-specific contacts, which were present due to crowded environment, were removed. Functional chromosomal contacts were spread onto glass slides. DNA was stained and antibodies to active transcription machinery and transcription factors were used to visualize these structures. We again employed BALM, and revealed the nanoscale structures of serum responsive clusters. The level of such clusters significantly decreased after serum starvation, suggesting that these were transcriptionally functional clusters, instead of non-specific structures. We also visualized YAP, and NF-κB target gene clusters. More interestingly, by incorporating micropatterning into our method, we were able to test the level of these specific clusters with different cell geometries. The trend of specific clusters in different cell geometries was consistent with expression levels of their target genes from microarray analysis [9].

These data collectively suggested that cell geometry reorients, repositions chromosome territories to alter the level of specific gene clusters visualized at a resolution of ~30 nm for differential genome regulation.

Regarding future directions, we've started to understand the molecular mechanisms behind geometry-regulated chromosome reorganization. Lamin A/C, responsible for tethering chromatin to the nuclear envelope [76], has been suggested as a regulator of chromosome

positioning [77]. In our study, both western blot and immunofluorescence showed a decrease in the protein level of Lamin A/C on IP substrates, while the protein level of Lamin B1 remained the same (Figures5.1A, B).

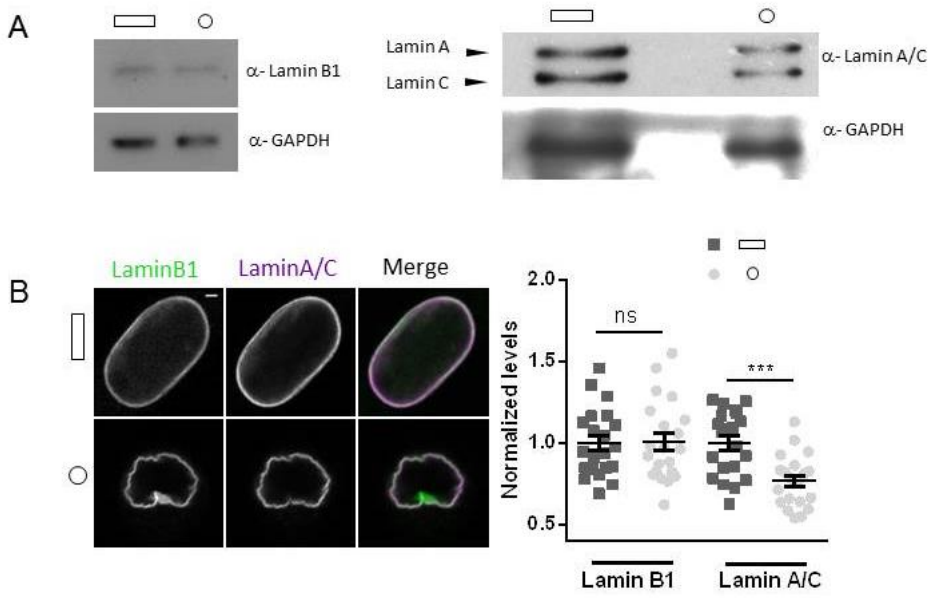

Figure 5.1 Lamin A/C protein level is decreased after cell matrix reduction. (A) Western blot of Lamin A/C and Lamin B1. (B) Confocal images of Lamin B1 (green), and Lamin A/C (pink). Dot plot showing the normalized protein level of Lamin B1 and Lamin A/C in the two geometric constraints. Data is given as mean ± SE. **P<0.01; ***P<0.001 Two sample student's t test.

To see whether Lamin A/C level was directly involved in geometry-dependent CT positioning, we overexpressed (OE) Lamin A/C in IP cells where Lamin A/C was downregulated, and found that Chr2, which previously localized to the nuclear interior on IP substrates, moved back towards the periphery (Figures5.2A). Furthermore, knocking out Lamin A/C from cells on AP substrates resulted in the movement of Chr2 to the interior nucleus (Figures5.2 B, C). As a result, Chr2 in LMNA -/- cells was transcriptionally more active with a higher level of 5S RNA pol2 at the chromosome surface (Figure5.2 D).

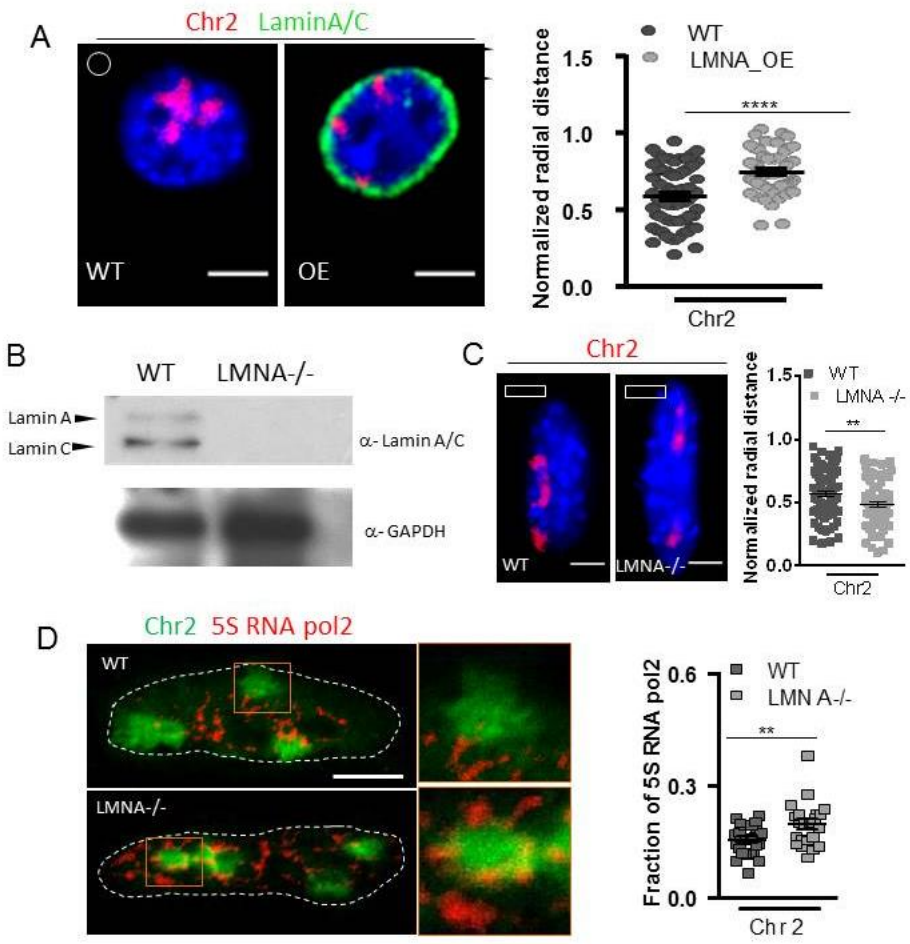

Figure 5.2 Lamin A/C regulates chromosome radial position and transcription activity. (A) Confocal images of Lamin A/C (green), Chr2 (red), and nucleus (blue). Scale bar: 5 μm. Dot plot showing the normalized radial distance in wild type (WT) cells and laminA/C overexpressed (LMNA OE) cells on IP substrates. Data is given as mean ± SE. ****P<0.0001 Two sample student's t test. (B) Western blot of Lamin A/C. (C) Confocal images of Chr2 (red), and nucleus (blue). Scale bar: 5 μm. Dot plot showing the normalized radial distance in WT cells and LaminA/C knockout (LMNA -/-) cells on AP substrates. Data is given as mean ± SE. **P<0.01. Two sample student's t test. (D) Confocal images of Lamin A/C (green), 5S RNA pol2 (red), and nuclear outline (white). Dot plot showing the fraction of 5S RNA pol2 on Chr2 in WT cells and LMNA -/- cells in AP substrates. Data is given as mean ± SE. **P<0.01 Two sample student's t test.

Transcription factors are critical in regulating gene expression. Interestingly, we found that the serum response cofactor MRTF-A localized inside the nucleus of AP cells which had enhanced actin stress fibers and flattened nucleus, while in IP cells MRTF-A resided in the cytoplasm where there was less stabilized actin filaments (Figure5.3A, C, E). In contrast, another transcription factor NF-κB (p65) mostly localized in the nucleus of IP cells, and within the cytoplasm of AP cells (Figure5.3B, D, E).

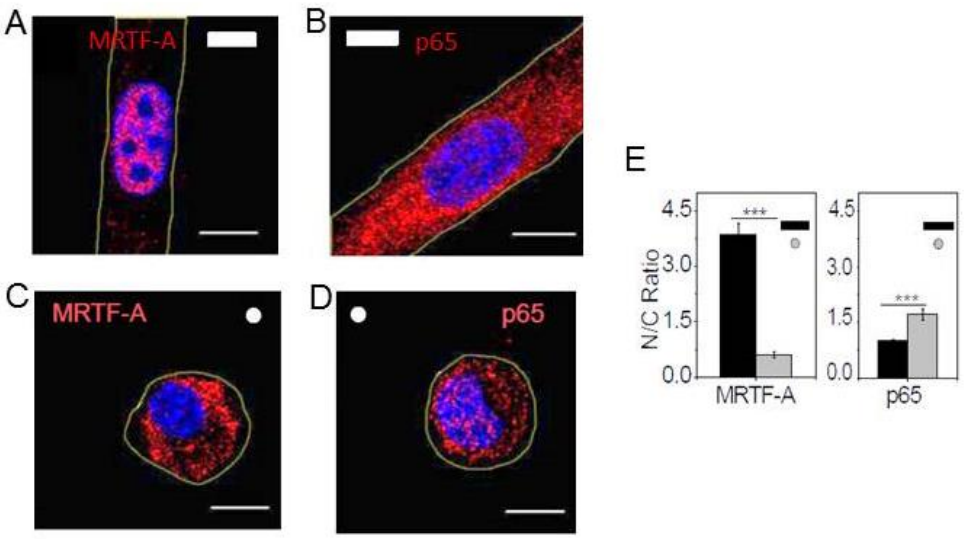

Figure 5.3: Compartmentalization transcription factors by cell geometry. (A-D) Representative images of nucleus stained by Hoechst and MRTF-A or p65 (red). Scale bar: 5μm. (E) Bar graph showing the nuclear to cytoplasmic (N/C) ratio of MRTF-A and p65. Data is presented as mean ± SE with 40<n<50. *** P<0.001. Two sample student's t test.

To check whether the nuclear fraction of the transcription factors was transcriptionally active, we did the colocalization analysis between the transcription factors and 5S RNA pol2 in confocal microscopy as well as superresolution microscopy (see Materials and Methods). 3D confocal images of 5S RNA pol2 and transcription factors were thresholded to remove the background noise (Figure5.4A, B). Colocalization fraction measures the level of colocalization within the 3D nuclear volume, which was not sensitive to the degree of image thresholding at a proper range (Figure5.4 C, D).

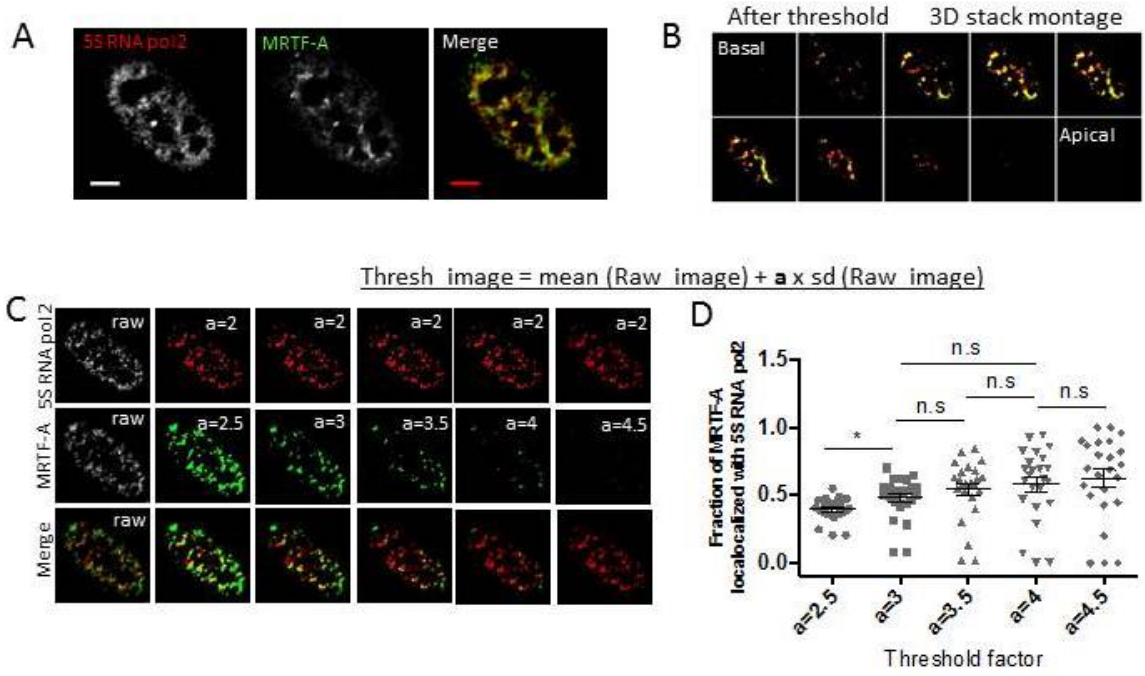

Figure 5.4: Colocalization fraction is not sensitive to image thresholding. (A) Confocal images of 5S RNA pol2 (red) and MRTF-A (green). Scale bar: 5 μm. (B) Montage of the 3D stack of 5S RNA pol2 (red) and MRTF-A (green) after thresholding. (C) Confocal images of 5S RNA pol2 (red) and MRTF-A (green) under different thresholding conditions. (D) Dot plot showing the fraction of MRTF-A colocalized with 5S RNA pol2 under different thresholding conditions. Data is given as mean ± SE. **P*<0.05 Two sample student's t test.

With this colocalization analysis, we found more MRTF-A/SRF/5S RNA pol2 clusters (regarded as SRF/MRTF-A regulated transcription units) in AP patterns, while more p65/5S RNA pol2 clusters (regarded as NF-κB regulated transcription units) were found in IP patterns (Figure5.5 A-C). The formation of SRF/MRTF-A regulated transcription units required the SRF binding domains on MRTF-A (Figure5.5 D-F). Structured illumination microscopy (SIM) revealed better-resolved structures of these specific transcription units (Figure5.5 G).

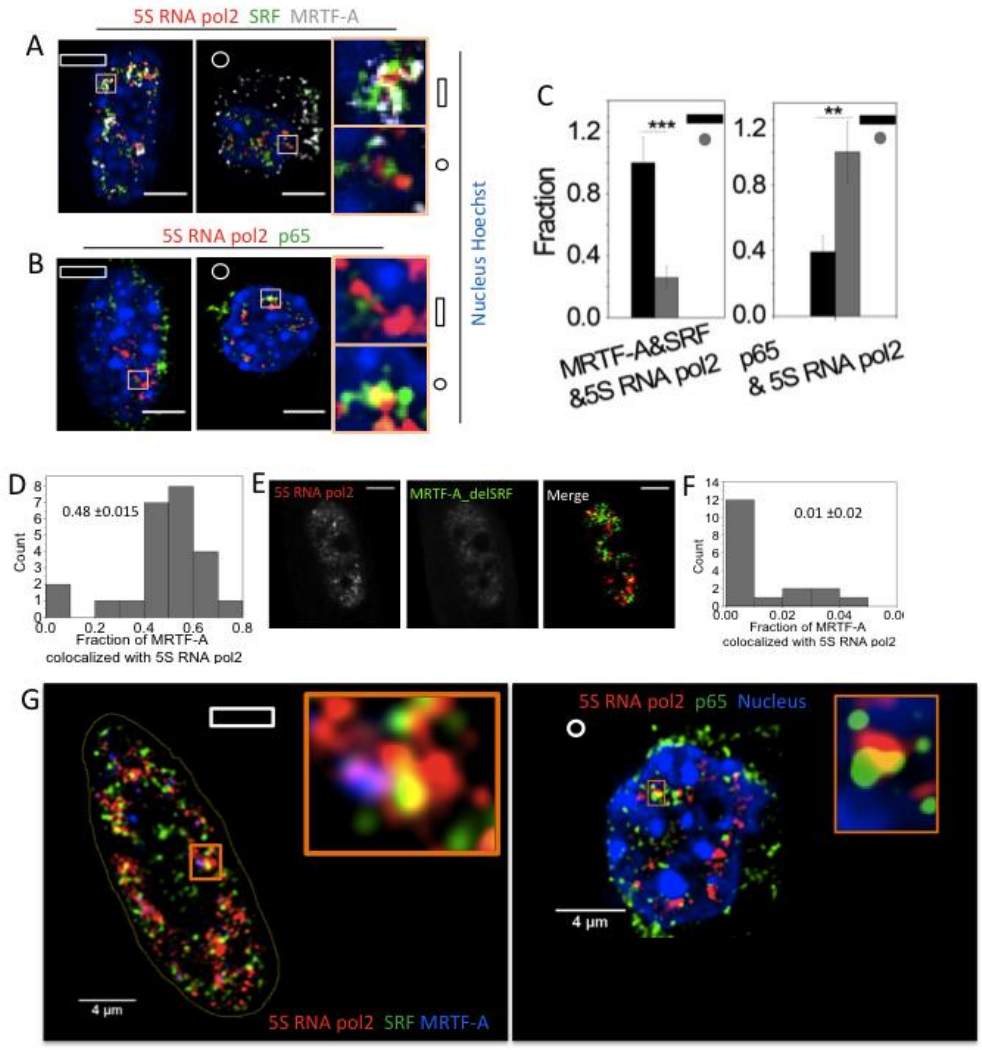

Figure 5.5: Colocalization of transcription factors and 5S RNA pol2. (A) Confocal images of nucleus (blue), 5S RNA pol2 (red), MRTF-A (grey), and SRF (green). Scale bar: 5 μm. Insets: Zoomed in images of the outlined regions by orange boxes. (B) Confocal images of nucleus (blue), 5S RNA pol2 (red) and p65 (green). Scale bar: 5 μm. Insets: Zoomed in images of the outlined regions by orange boxes. (C) Bar graph showing the different fraction of 5S RNA pol2 & SRF & MRTF-A or 5S RNA pol2 & p65 clusters in both geometries. Data is presented as mean ± SE with $50 < n < 60$. ** $P<0.01$, *** $P<0.001$; Two sample student's t test. (D) Histogram of the fraction of MRTF-A colocalized with 5S RNA pol2. (E) Confocal images of 5S RNA pol2 (red) and MRTF-A without SRF binding domain (MRTF-A_delSRF, green). Scale bar: 5 μm. (F) Histogram of the fraction of MRTF-A _delSRF colocalized with 5S RNA pol2. (G) The representative SIM images of 5S RNA pol2 (red), SRF or p65 (green), MRTF-A or hochst (blue), and the nuclear outline (yellow) in the two geometries. Scale bar: 4 μm. Insets: the zoomed images of the outlined regions with white boxes.

To decouple the effects from the compartmentalization of transcription factors and cell geometry, we relocated MRTF-A from nucleus to cytoplasm while not changing cell shapes significantly by adding TNF-α (Figure5.6A, B). Interestingly, Chr5 and Chr9 that had large

intermingling volume in AP substrates showed a decrease in their intermingling degrees after MRTF-A was excluded from nucleus (Figure5.6 C, D). These results indicate that transcription factors are required for chromosome intermingling. More interestingly, inducing nuclear localization of MRTF-A by stabilizing actin filaments with Jasplokinolide [14] while the nuclear morphology and chromosome orientations remained similar didn't not increase the intermingling between Chr5 and Chr9 (Figure5.6 E, F). This suggests that transcription factor alone is not sufficient for new contacts formation. The nuclear morphology change which reorients and repositions chromosomes is also indispensable.

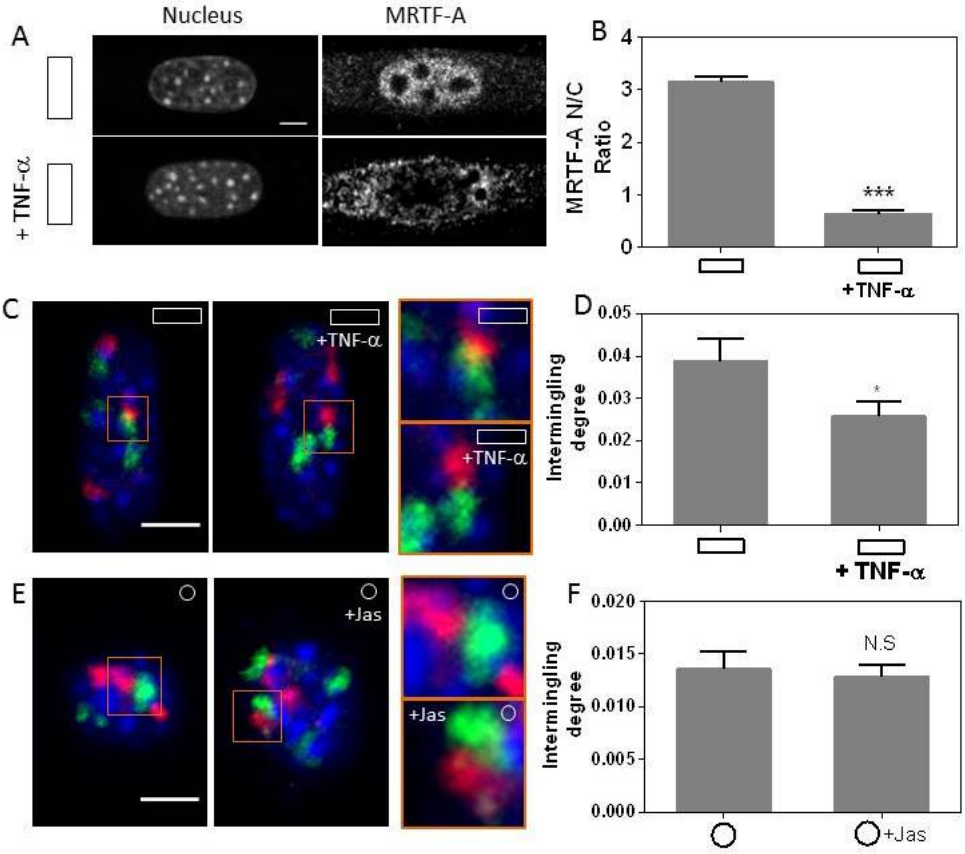

Figure 5.6: Nuclear localization of MRTF-A and nuclear morphology changes are both required for new contacts formation. (A) Representative images of nucleus stained by Hoechst and MRTF-A. Scale bar: 5mm. (B) Bar graph showing the nuclear to cytoplasmic (N/C) ratio of MRTF-A. Data is presented as mean ± SE with 40<n<50. *** P<0.001. Two sample student's t test. (C) and (E) Representative images showing the intermingling between Chr5 and Chr9. (D) and (F) Bar graph quantifying the intermingling degree between Chr5 and Chr9. Data is presented as mean ± SE with 40<n<50. N.S indicates not significant. Mann-Whitney U test.

To fully understand the molecular mechanisms of the mechano-sensitive chromosome reorganization, we are planning to systematically investigate the role of Lamin A/C on the radial position of chromosomes. While we have shown preliminarily that the geometry-sensitive transcription factors regulate the formation of their target chromosomal contacts, we will also investigate further about the role of specific transcription factors on stabilizing chromosome intermingling.

Taken together, this thesis proposed that changes in nuclear morphology facilitate the formation of new chromosomal contacts to optimize transcription programs. Alterations in nuclear shape result in chromosome reorientation and repositioning due to spatial constraints as well as differential Lamin A/C levels regulated by cell geometry. The specificity of chromosomes repositioning is attributed to chromosome orientations with respect to nuclear mechanical axis. However, we did not exclude the possibility that the specific chromosome repositioning can also be regulated by differential tethering between Lamin A/C and chromosomes, which might be the upstream of chromosome orientations. Alterations in chromosome radial position creates new neighborhoods with different intermingling degrees. The intermingling regions were enriched with 5S RNA pol2, SRF, and SRF target gene *zyxin*. Superresolution imaging of digested chromatin fragments further revealed various specific contacts including SRF target contacts, the level of which was positively correlated with the expression of SRF target genes in both cell geometries. While transcription machinery and specific factors are necessary for contacts formation and stabilization, cell geometry was shown to compartmentalize specific transcription factors, which coordinates with chromosome reorganization to form the optimized chromosome neighborhoods and specific chromosomal contacts to achieve differential expression patterns. These results are highly suggestive of a combined mechano-chemical regulation of chromosomal organizations to bring about cell shape specific gene expression patterns.

Under normal ECM conditions cells maintain a nuclear mechanical homeostasis and fix a

particular CT orientations and organization that is optimized for the specific gene expression program. Alterations in matrix signals can lead to a number of diseases, including fibrosis and tumor initiation and progression [78]. Such ECM modulations can also result in induction of mesenchymal to epithelial transition (MET) or in the formation of cancer associated fibroblasts [79]. These trans-differentiation programs involve the remodeling of cytoskeletal organization and thus nuclear morphology. These changes lead to the reorientation and rearrangement of CTs and their intermingling, facilitating differential regulation of gene expression. Understanding CT arrangements and the precise link to gene expression patterns across various cell types [80], could serve as a "zip code" for controlling gene expression, leading to interesting applications for cell reprogramming using geometric constraints.

BIBILIOGRAPHY

1. Wang, N., J.D. Tytell, and D.E. Ingber, *Mechanotransduction at a distance: mechanically coupling the extracellular matrix with the nucleus.* Nature reviews Molecular cell biology, 2009. **10**(1): p. 75-82.
2. Humphrey, J.D., E.R. Dufresne, and M.A. Schwartz, *Mechanotransduction and extracellular matrix homeostasis.* Nature reviews Molecular cell biology, 2014.
3. Folkman, J. and A. Moscona, *Role of cell shape in growth control.* 1978.
4. Lu, P., et al., *Extracellular matrix degradation and remodeling in development and disease.* Cold Spring Harbor perspectives in biology, 2011. **3**(12): p. a005058.
5. Levental, K.R., et al., *Matrix crosslinking forces tumor progression by enhancing integrin signaling.* Cell, 2009. **139**(5): p. 891-906.
6. Chen, C.S., et al., *Geometric control of cell life and death.* Science, 1997. **276**(5317): p. 1425-1428.
7. Engler, A.J., et al., *Matrix elasticity directs stem cell lineage specification.* Cell, 2006. **126**(4): p. 677-689.
8. Kilian, K.A., et al., *Geometric cues for directing the differentiation of mesenchymal stem cells.* Proceedings of the National Academy of Sciences, 2010. **107**(11): p. 4872-4877.
9. Jain, N., et al., *Cell geometric constraints induce modular gene-expression patterns via redistribution of HDAC3 regulated by actomyosin contractility.* Proceedings of the National Academy of Sciences, 2013. **110**(28): p. 11349-11354.

10. Desprat, N., et al., *Tissue deformation modulates twist expression to determine anterior midgut differentiation in Drosophila embryos.* Developmental cell, 2008. **15**(3): p. 470-477.
11. Iskratsch, T., H. Wolfenson, and M.P. Sheetz, *Appreciating force and shape [mdash] the rise of mechanotransduction in cell biology.* Nature reviews Molecular cell biology, 2014.
12. Zullo, J.M., et al., *DNA sequence-dependent compartmentalization and silencing of chromatin at the nuclear lamina.* Cell, 2012. **149**(7): p. 1474-1487.
13. Guelen, L., et al., *Domain organization of human chromosomes revealed by mapping of nuclear lamina interactions.* Nature, 2008. **453**(7197): p. 948-951.
14. Iyer, K.V., et al., *Mechanical activation of cells induces chromatin remodeling preceding MKL nuclear transport.* Biophysical journal, 2012. **103**(7): p. 1416-1428.
15. Dupont, S., et al., *Role of YAP/TAZ in mechanotransduction.* Nature, 2011. **474**(7350): p. 179-183.
16. Le, H.Q., et al., *Mechanical regulation of transcription controls Polycomb-mediated gene silencing during lineage commitment.* Nature Cell Biology, 2016.
17. Langmore, J. and C. Schutt, *The higher order structure of chicken erythrocyte chromosomes in vivo.* 1980.
18. Belmont, A.S. and K. Bruce, *Visualization of G1 chromosomes: a folded, twisted, supercoiled chromonema model of interphase chromatid structure.* The Journal of cell biology, 1994. **127**(2): p. 287-302.
19. Kornberg, R.D. and Y. Lorch, *Twenty-five years of the nucleosome, review fundamental particle of the eukaryote chromosome.* Cell, 1999. **98**: p. 285-294.
20. Thomas, J.O., *Histone H1: location and role.* Current opinion in cell biology, 1999. **11**(3): p. 312-317.
21. Happel, N. and D. Doenecke, *Histone H1 and its isoforms: contribution to chromatin structure and function.* Gene, 2009. **431**(1): p. 1-12.
22. Fedorova, E. and D. Zink, *Nuclear architecture and gene regulation.* Biochim Biophys Acta, 2008. **1783**(11): p. 2174-2184.
23. Schneider, R. and R. Grosschedl, *Dynamics and interplay of nuclear architecture, genome organization, and gene expression.* Genes & development, 2007. **21**(23): p. 3027-3043.
24. Sims, R.J., K. Nishioka, and D. Reinberg, *Histone lysine methylation: a signature for chromatin function.* TRENDS in Genetics, 2003. **19**(11): p. 629-639.
25. Wang, X., et al., *Effects of histone acetylation on the solubility and folding of the chromatin fiber.* Journal of Biological Chemistry, 2001. **276**(16): p. 12764-12768.
26. Sproul, D., N. Gilbert, and W.A. Bickmore, *The role of chromatin structure in regulating the expression of clustered genes.* Nature Reviews Genetics, 2005. **6**(10): p. 775-781.
27. van de Corput, M.P., et al., *Super-resolution imaging reveals three-dimensional folding dynamics of the β-globin locus upon gene activation.* Journal of Cell Science, 2012. **125**(19): p. 4630-4639.
28. Lanctôt, C., et al., *Dynamic genome architecture in the nuclear space: regulation of gene expression in three dimensions.* Nature Reviews Genetics, 2007. **8**(2): p. 104-115.
29. Croft, J.A., et al., *Differences in the localization and morphology of chromosomes in the human nucleus.* The Journal of cell biology, 1999. **145**(6): p. 1119-1131.
30. Cremer, M., et al., *Non-random radial higher-order chromatin arrangements in nuclei of diploid human cells.* Chromosome research, 2001. **9**(7): p. 541-567.
31. Bolzer, A., et al., *Three-dimensional maps of all chromosomes in human male fibroblast nuclei and prometaphase rosettes.* PLoS Biol, 2005. **3**(5): p. e157.

32. Malhas, A., et al., *Defects in lamin B1 expression or processing affect interphase chromosome position and gene expression.* The Journal of cell biology, 2007. **176**(5): p. 593-603.
33. Khrameeva, E.E., et al., *Spatial proximity and similarity of the epigenetic state of genome domains.* PLoS One, 2012. **7**(4): p. e33947.
34. Iyer, K.V., et al., *Modeling and experimental methods to probe the link between global transcription and spatial organization of chromosomes.* PloS one, 2012. **7**(10): p. e46628.
35. Maharana, S., *Chromosome intermingling--the physical basis of chromosome organization in differentiated cells* Nucleic Acid Research, 2016.
36. Branco, M.R. and A. Pombo, *Intermingling of chromosome territories in interphase suggests role in translocations and transcription-dependent associations.* PLoS biology, 2006. **4**(5): p. 780.
37. Van Steensel, B. and J. Dekker, *Genomics tools for unraveling chromosome architecture.* Nature biotechnology, 2010. **28**(10): p. 1089-1095.
38. Osborne, C.S., et al., *Active genes dynamically colocalize to shared sites of ongoing transcription.* Nature genetics, 2004. **36**(10): p. 1065-1071.
39. Noordermeer, D., et al., *The dynamic architecture of Hox gene clusters.* Science, 2011. **334**(6053): p. 222-225.
40. Jin, F., et al., *A high-resolution map of the three-dimensional chromatin interactome in human cells.* Nature, 2013. **503**(7475): p. 290-294.
41. Fanucchi, S., et al., *Chromosomal contact permits transcription between coregulated genes.* Cell, 2013. **155**(3): p. 606-620.
42. Bouchet-Marquis, C., J. Dubochet, and S. Fakan, *Cryoelectron microscopy of vitrified sections: a new challenge for the analysis of functional nuclear architecture.* Histochemistry and cell biology, 2006. **125**(1-2): p. 43-51.
43. Scheffer, M.P., M. Eltsov, and A.S. Frangakis, *Evidence for short-range helical order in the 30-nm chromatin fibers of erythrocyte nuclei.* Proceedings of the National Academy of Sciences, 2011. **108**(41): p. 16992-16997.
44. Naryshkin, N., et al., *Structural organization of the RNA polymerase-promoter open complex.* Cell, 2000. **101**(6): p. 601-611.
45. Littlefield, O., Y. Korkhin, and P.B. Sigler, *The structural basis for the oriented assembly of a TBP/TFB/promoter complex.* Proceedings of the National Academy of Sciences, 1999. **96**(24): p. 13668-13673.
46. Renfrow, M.B., et al., *Transcription factor B contacts promoter DNA near the transcription start site of the archaeal transcription initiation complex.* Journal of Biological Chemistry, 2004. **279**(4): p. 2825-2831.
47. Kornberg, R.D., *Chromatin structure: a repeating unit of histones and DNA.* Science, 1974. **184**(4139): p. 868-871.
48. Schalch, T., et al., *X-ray structure of a tetranucleosome and its implications for the chromatin fibre.* Nature, 2005. **436**(7047): p. 138-141.
49. Kruhlak, M.J., et al., *Changes in chromatin structure and mobility in living cells at sites of DNA double-strand breaks.* The Journal of cell biology, 2006. **172**(6): p. 823-834.
50. Hazzouri, M., et al., *Genome organization in the human sperm nucleus studied by FISH and confocal microscopy.* Molecular reproduction and development, 2000. **55**(3): p. 307-315.
51. Heilemann, M., *Fluorescence microscopy beyond the diffraction limit.* Journal of biotechnology, 2010. **149**(4): p. 243-251.
52. Hell, S.W., *Microscopy and its focal switch.* Nature Methods, 2008. **6**(1): p. 24-32.

53. Huang, B., H. Babcock, and X. Zhuang, *Breaking the diffraction barrier: super-resolution imaging of cells.* Cell, 2010. **143**(7): p. 1047-1058.
54. Mitchell-Jordan, S., et al., *Features of endogenous cardiomyocyte chromatin revealed by super resolution STED microscopy.* Journal of Molecular and Cellular Cardiology, 2012.
55. Betzig, E., et al., *Imaging intracellular fluorescent proteins at nanometer resolution.* Science, 2006. **313**(5793): p. 1642-1645.
56. Heilemann, M., et al., *Subdiffraction‐resolution fluorescence imaging with conventional fluorescent probes.* Angewandte Chemie International Edition, 2008. **47**(33): p. 6172-6176.
57. Matsuda, A., et al., *Condensed mitotic chromosome structure at nanometer resolution using PALM and EGFP-histones.* PloS one, 2010. **5**(9): p. e12768.
58. Zessin, P.J., K. Finan, and M. Heilemann, *Super-resolution fluorescence imaging of chromosomal DNA.* Journal of Structural Biology, 2012. **177**(2): p. 344-348.
59. Schoen, I., et al., *Binding-activated localization microscopy of DNA structures.* Nano letters, 2011. **11**(9): p. 4008-4011.
60. Boettiger, A.N., et al., *Super-resolution imaging reveals distinct chromatin folding for different epigenetic states.* Nature, 2016. **529**(7586): p. 418-422.
61. Kanda, T., K.F. Sullivan, and G.M. Wahl, *Histone–GFP fusion protein enables sensitive analysis of chromosome dynamics in living mammalian cells.* Current Biology, 1998. **8**(7): p. 377-385.
62. Hameed, F.M., et al., *Probing structural stability of chromatin assembly sorted from living cells.* Biochem Biophys Res Commun, 2009. **385**(4): p. 518-22.
63. Schoen, I., et al., *Binding-activated localization microscopy of DNA structures.* Nano Lett, 2011. **11**(9): p. 4008-11.
64. Bensimon, D., et al., *Stretching DNA with a receding meniscus: experiments and models.* Physical review letters, 1995. **74**(23): p. 4754-4757.
65. Noordermeer, D., et al., *Variegated gene expression caused by cell-specific long-range DNA interactions.* Nature cell biology, 2011. **13**(8): p. 944-951.
66. Fullwood, M.J., et al., *An oestrogen-receptor-&agr;-bound human chromatin interactome.* Nature, 2009. **462**(7269): p. 58-64.
67. Schoenfelder, S., et al., *Preferential associations between co-regulated genes reveal a transcriptional interactome in erythroid cells.* Nature genetics, 2010. **42**(1): p. 53-61.
68. Nguyen, V.T., et al., *In vivo degradation of RNA polymerase II largest subunit triggered by α-amanitin.* Nucleic acids research, 1996. **24**(15): p. 2924-2929.
69. Bhattacharya, D., et al., *EGFP-tagged core and linker histones diffuse via distinct mechanisms within living cells.* Biophysical journal, 2006. **91**(6): p. 2326-2336.
70. Flors, C., *Photoswitching of monomeric and dimeric DNA-intercalating cyanine dyes for super-resolution microscopy applications.* Photochem Photobiol Sci, 2010. **9**(5): p. 643-8.
71. Gustincich, S. and C. Schneider, *Serum deprivation response gene is induced by serum starvation but not by contact inhibition.* Cell growth & differentiation: the molecular biology journal of the American Association for Cancer Research, 1993. **4**(9): p. 753.
72. Schmittgen, T.D. and B.A. Zakrajsek, *Effect of experimental treatment on housekeeping gene expression: validation by real-time, quantitative RT-PCR.* Journal of biochemical and biophysical methods, 2000. **46**(1): p. 69-81.
73. Iyer, V.R., et al., *The transcriptional program in the response of human fibroblasts to serum.* Science, 1999. **283**(5398): p. 83-87.

74. Wang, Y., et al., *Super-resolution microscopy reveals decondensed chromatin structure at transcription sites.* Scientific reports, 2014. **4**.
75. Maeshima, K., S. Hihara, and M. Eltsov, *Chromatin structure: does the 30-nm fibre exist in vivo?* Current opinion in cell biology, 2010. **22**(3): p. 291-297.
76. Harr, J.C., et al., *Directed targeting of chromatin to the nuclear lamina is mediated by chromatin state and A-type lamins.* The Journal of cell biology, 2015. **208**(1): p. 33-52.
77. Mewborn, S.K., et al., *Altered chromosomal positioning, compaction, and gene expression with a lamin A/C gene mutation.* PloS one, 2010. **5**(12): p. e14342.
78. Butcher, D.T., T. Alliston, and V.M. Weaver, *A tense situation: forcing tumour progression.* Nature Reviews Cancer, 2009. **9**(2): p. 108-122.
79. Augsten, M., *Cancer-associated fibroblasts as another polarized cell type of the tumor microenvironment.* Frontiers in oncology, 2014. **4**.
80. Parada, L.A., P.G. McQueen, and T. Misteli, *Tissue-specific spatial organization of genomes.* Genome biology, 2004. **5**(7): p. R44.

APPENDICES

1. Copyright permission for Figure 1.1

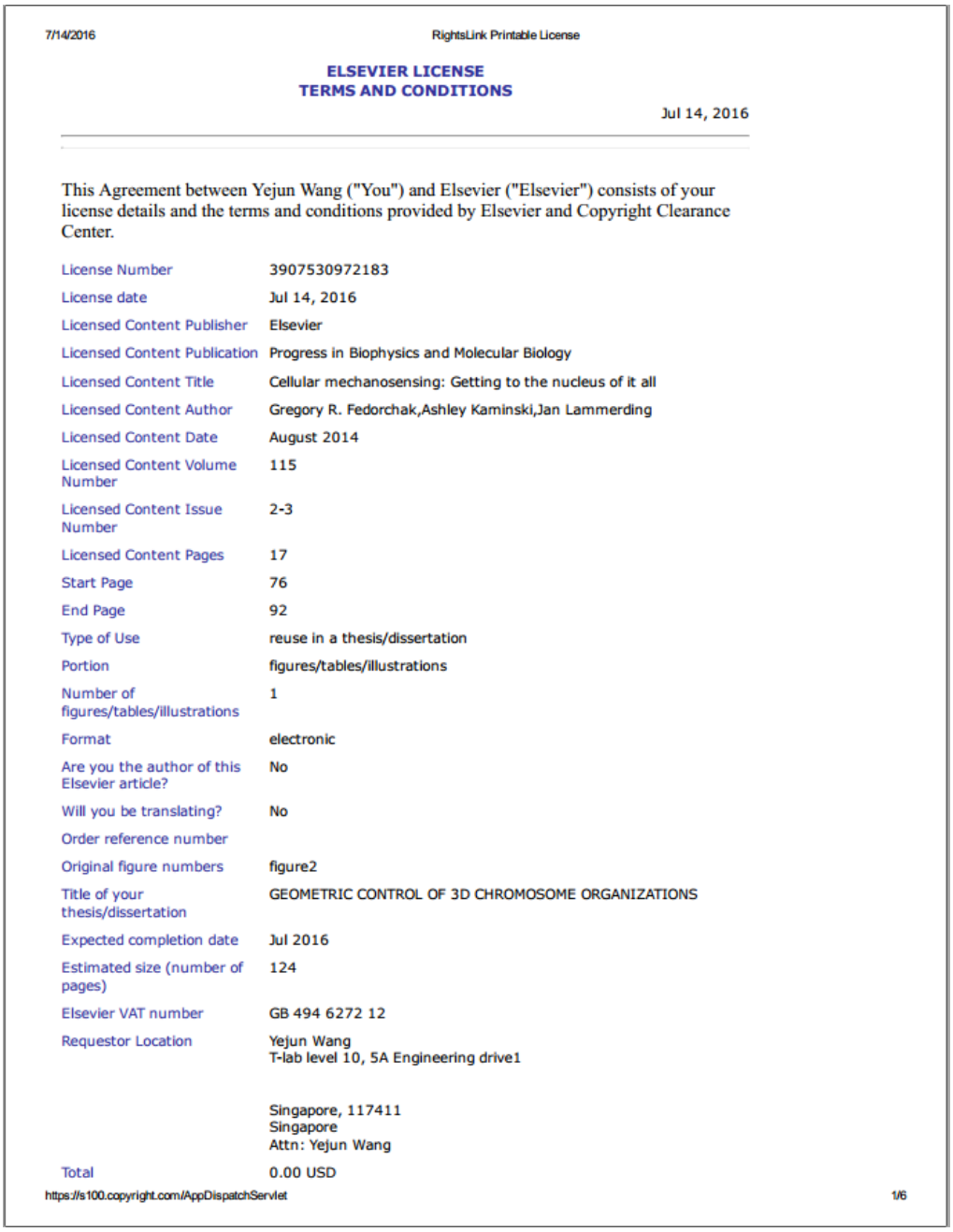

7/14/2016 RightsLink Printable License

ELSEVIER LICENSE
TERMS AND CONDITIONS

Jul 14, 2016

This Agreement between Yejun Wang ("You") and Elsevier ("Elsevier") consists of your license details and the terms and conditions provided by Elsevier and Copyright Clearance Center.

License Number	3907530972183
License date	Jul 14, 2016
Licensed Content Publisher	Elsevier
Licensed Content Publication	Progress in Biophysics and Molecular Biology
Licensed Content Title	Cellular mechanosensing: Getting to the nucleus of it all
Licensed Content Author	Gregory R. Fedorchak,Ashley Kaminski,Jan Lammerding
Licensed Content Date	August 2014
Licensed Content Volume Number	115
Licensed Content Issue Number	2-3
Licensed Content Pages	17
Start Page	76
End Page	92
Type of Use	reuse in a thesis/dissertation
Portion	figures/tables/illustrations
Number of figures/tables/illustrations	1
Format	electronic
Are you the author of this Elsevier article?	No
Will you be translating?	No
Order reference number	
Original figure numbers	figure2
Title of your thesis/dissertation	GEOMETRIC CONTROL OF 3D CHROMOSOME ORGANIZATIONS
Expected completion date	Jul 2016
Estimated size (number of pages)	124
Elsevier VAT number	GB 494 6272 12
Requestor Location	Yejun Wang T-lab level 10, 5A Engineering drive1 Singapore, 117411 Singapore Attn: Yejun Wang
Total	0.00 USD

https://s100.copyright.com/AppDispatchServlet 1/6

2. Copyright permission for Figure 3.19

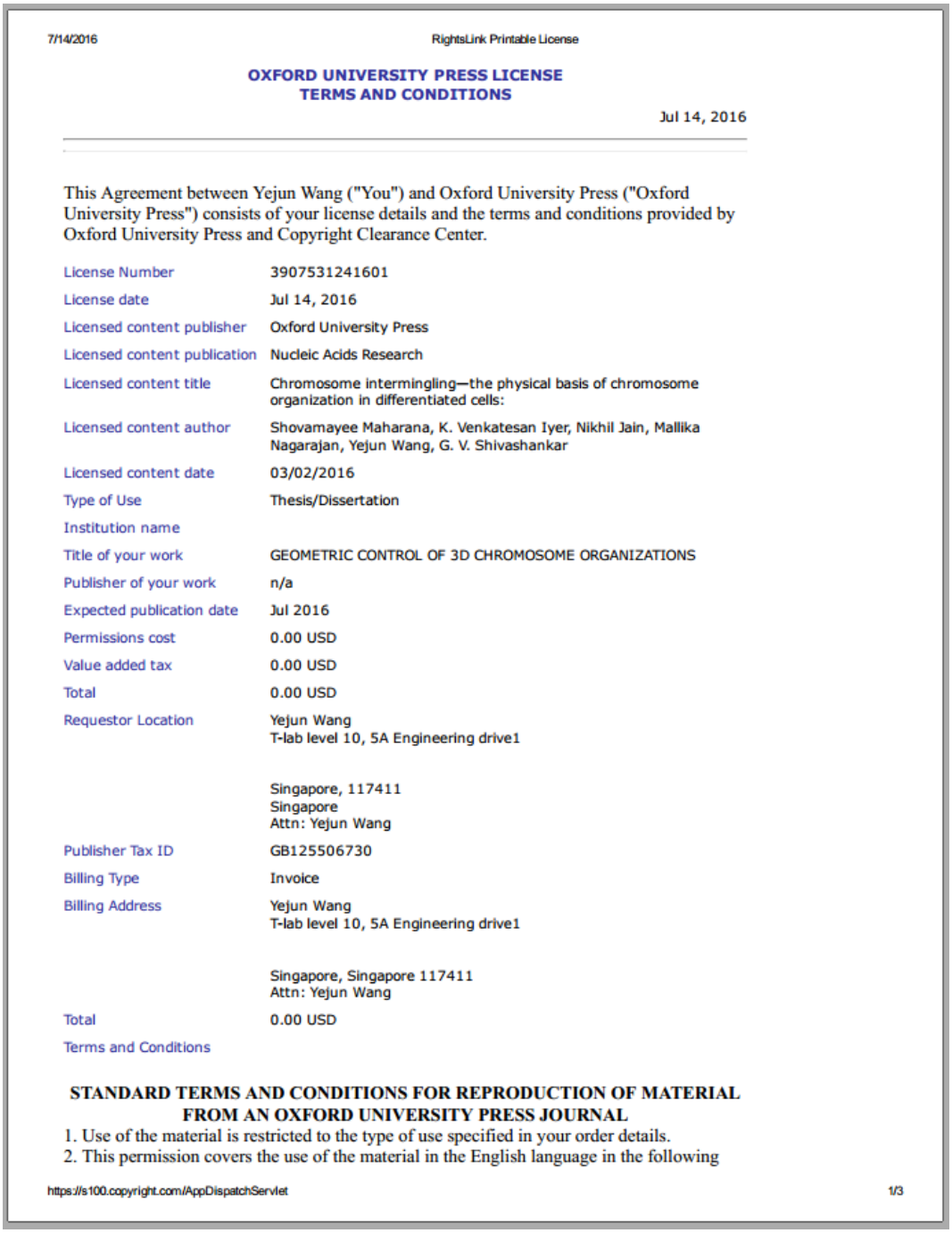

7/14/2016 RightsLink Printable License

OXFORD UNIVERSITY PRESS LICENSE TERMS AND CONDITIONS

Jul 14, 2016

This Agreement between Yejun Wang ("You") and Oxford University Press ("Oxford University Press") consists of your license details and the terms and conditions provided by Oxford University Press and Copyright Clearance Center.

License Number	3907531241601
License date	Jul 14, 2016
Licensed content publisher	Oxford University Press
Licensed content publication	Nucleic Acids Research
Licensed content title	Chromosome intermingling—the physical basis of chromosome organization in differentiated cells:
Licensed content author	Shovamayee Maharana, K. Venkatesan Iyer, Nikhil Jain, Mallika Nagarajan, Yejun Wang, G. V. Shivashankar
Licensed content date	03/02/2016
Type of Use	Thesis/Dissertation
Institution name	
Title of your work	GEOMETRIC CONTROL OF 3D CHROMOSOME ORGANIZATIONS
Publisher of your work	n/a
Expected publication date	Jul 2016
Permissions cost	0.00 USD
Value added tax	0.00 USD
Total	0.00 USD
Requestor Location	Yejun Wang T-lab level 10, 5A Engineering drive1 Singapore, 117411 Singapore Attn: Yejun Wang
Publisher Tax ID	GB125506730
Billing Type	Invoice
Billing Address	Yejun Wang T-lab level 10, 5A Engineering drive1 Singapore, Singapore 117411 Attn: Yejun Wang
Total	0.00 USD
Terms and Conditions	

STANDARD TERMS AND CONDITIONS FOR REPRODUCTION OF MATERIAL FROM AN OXFORD UNIVERSITY PRESS JOURNAL

1. Use of the material is restricted to the type of use specified in your order details.
2. This permission covers the use of the material in the English language in the following

https://s100.copyright.com/AppDispatchServlet 1/3